Spring 1-1-2012

THEMIS Observations of Electron Phase-Space Holes, the Lunar Wake, and Turbulence

Jianbao Tao
University of Colorado at Boulder, jianbao.tao@gmail.com

THEMIS Observations of Electron Phase-Space Holes, the Lunar Wake, and Turbulence

by

Jianbao Tao

B.S., University of Science and Technology of China, 2004

M.S., University of Colorado at Boulder, 2010

A thesis submitted to the

Faculty of the Graduate School of the

University of Colorado in partial fulfillment

of the requirements for the degree of

Doctor of Philosophy

Department of Astrophysical and Planetary Sciences

2012

This thesis entitled:
THEMIS Observations of Electron Phase-Space Holes, the Lunar Wake, and Turbulence
written by Jianbao Tao
has been approved for the Department of Astrophysical and Planetary Sciences

Robert Ergun

Fran Bagenal

Mark Rast

Laila Andersson

Martin Goldman

Date

The final copy of this thesis has been examined by the signatories, and we find that both the content and the form meet acceptable presentation standards of scholarly work in the above mentioned discipline.

Tao, Jianbao (Ph.D., Astrophysics)

THEMIS Observations of Electron Phase-Space Holes, the Lunar Wake, and Turbulence

Thesis directed by Robert Ergun

THEMIS is a recent multi-satellite mission launched in 2007 with five identical spacecraft orbiting in the equatorial plane of the Earth. Featuring a comprehensive package of particle and field instruments on each THEMIS spacecraft and multi-resolution data products, the THEMIS mission offers great opportunities to study space plasma dynamics in both large MHD scales and relatively small kinetic scales. This work focuses on kinetic aspects of space plasma dynamics using THEMIS observations, especially electric field observations, which are critical to study kinetic effects. Three specific topics, electron phase-space holes (EHs), kinetic instabilities in the lunar wake, and turbulent electric and magnetic fields in the Earth's magnetotail, are investigated in detail.

EHs are good indicators of nonlinear activities in space plasmas and have attracted many interests in both observational and theoretical work. In a traditional theoretical picture, EHs are understood as purely electrostatic structures. However, THEMIS recently observed electromagnetic EHs, which cannot be fully described with traditional theory, in the plasma sheet boundary layer. This work seeks to understand the magnetic signals of the observed electromagnetic EHs. In addition to the interpretations of the observed magnetic signals, a statistical study of the properties of the observed electromagnetic EHs reveals that those electromagnetic EHs feature fast speeds, large sizes, and strong potentials, which intrigues interests in their generation mechanism and influences on the space plasma environment.

The lunar wake, resulting from the interaction between the solar wind and the Moon, is an excellent example to study the expansion of plasmas into a more tenuous space. One of the THEMIS spacecraft, THB (known as ARTEMIS P1 after winter 2009) provided new

observations of the lunar wake from a lunar-wake flyby in early 2010. Kinetic instabilities from that flyby are examined in this work. Wavelengths and phase velocities of the observed kinetic instabilities are derived from electric field instrument voltage measurements using interferometric techniques, providing unprecedented information of the properties of kinetic instabilities in the lunar wake. In addition, the mode of the observed kinetic instabilities is identified as the electron beam mode, confirming a global-scale dynamics, electron velocity filtration by the negative lunar-wake potential, as proposed in previous works.

Turbulence, an efficient mechanism to dissipate kinetic energy into thermal energy, plays an important role in the global energy budget in the plasma sheet. Previous studies of turbulence in the plasma sheet generally focused on MHD scales and did not include electric field measurements. This work combines both electric and magnetic field measurements from THEMIS in the Earth's magnetotail with a frequency range that extends from MHD scales to kinetic scales. Statistical results of Poynting flux and spectral behavior of the turbulent electric and magnetic fields are presented. The Poynting flux results suggest that the turbulent electric and magnetic fields play an important role in the energy coupling between the ionosphere and the magnetosphere, whereas the spectral results may include information on universal relations between electric and magnetic fields for turbulence in plasmas.

献给我的父母

Acknowledgements

First and foremost, I am grateful to my advisor, Bob Ergun, in many ways. His sharp physics instinct is always eye-opening and inspiring; his high expectations always drive me to learn more and think more deeply; his entertaining spirit makes it a lot of fun to work with him. Towards the end of my Ph.D. study, he provided important support for my job hunting and a temporary job offer as a smooth transition to my new job at Berkeley, which is much appreciated.

Laila Andersson served as my direct supervisor at LASP. She helped me with almost everything in the beginning of my study at Boulder. In particular, I appreciate it a lot that she taught me how to analyze space plasma data with great patience. She also provided necessary financial support to my work. As with Laila, David Newman from CIPS has been rather kind and helpful to me all the way along. I learned so much about plasma physics and beyond from our discussions. Among other tools he shared with me, his Vlasov code is a great support to my thesis.

It is a pleasure to express my gratitude to David Malaspina. I enjoyed many discussions with him, whether work-related or not. I especially appreciate the time he spent with me skiing and bike riding. He helped me with the English language on many occasions, for which I am truly thankful.

The THEMIS and ARTEMIS teams have been very helpful to my research. In particular, I would like to thank Vassilis Angelopoulos, John Bonnell, Jim McFadden, Chris Cully, and Jasper Halekas.

I benefited from the interaction with many great people around me in the last five years. I would like to thank them all, especially Jack Gosling, Stefan Eriksson, Marty Goldman, and Bill Peterson. In addition, I would also like to thank Peter Delamere and Fran Bagenal for their help during my comprehensive exam II project.

I am grateful for the editing help for my thesis I received from Heather Beasley. Additionally, the editing help from Juthika Khargharia is acknowledged with pleasure.

The financial support I received from the NASA Earth and Space Sciences Fellowship is gratefully acknowledged.

Finally, I thank all my thesis committee members for all the help and support they provided.

Contents

Chapter

Tables

Table

Figures

Figure

Chapter 1

Introduction

THEMIS is a recent multi-satellite mission launched in 2007 with five identical spacecraft orbiting in the equatorial plane of the Earth. (Two spacecraft of the THEMIS mission were redirected to the Moon in winter 2009 and formed a new lunar mission, ARTEMIS, and therefore opened opportunities to study the lunar wake. See Appendix A for detail.) Featuring a comprehensive package of particle and field instruments on each THEMIS spacecraft and multi-resolution data products, the THEMIS mission offers great opportunities to study space plasma dynamics in both large MHD scales and relatively small kinetic scales. This work focuses on kinetic aspects of space plasma dynamics using THEMIS observations, especially electric field observations, which are critical to study kinetic effects. Three specific topics, electron phase-space holes (EHs), kinetic instabilities in the lunar wake, and turbulent electric and magnetic fields in the Earth's magnetotail, are investigated in detail.

These three topics show multiple applications of electric field measurements. The study of EHs primarily uses high time-resolution electric field waveforms. For the kinetic instabilities observed in the lunar wake, the interferometry techniques employed in the study primarily use potential measurements from the electric field instrument. For the turbulence study, the spectra of the electric field measurements are primarily used.

1.1 Electron Phase-Space Holes

1.1.1 The physics of EH

In their original work, *Bernstein, Greene, and Kruskal* [1957] solved the exact one-dimensional, stationary Vlasov-Poisson system and demonstrated that an arbitrary travelling wave solution could be constructed by an appropriate distribution of particles trapped in potential-energy troughs. In addition, they showed that the distribution function of trapped particles is nonlinear even in the limit of small-amplitude potentials. Because of their fundamental work, a wave mode due to the nonlinear balance between the electrostatic potential and trapped particles is often called a BGK mode. Unlike linear normal wave modes, a BGK mode is not necessarily a series of continuous waveforms. A large range of solitary potential structures can be a BGK mode. Moreover, this paper established a standard procedure to solve the stationary Vlasov-Poisson system, which consists of two main steps: 1) Prescribe a potential structure and the distribution of non-trapped particles; 2) solve the stationary Vlasov-Poisson system for the distribution of trapped particles. This procedure is often called the BGK method.

In real space, the characteristic motion of trapped particles is bouncing back and forth in potential-energy troughs. In phase space, this motion translates to a vortical motion. Figure 1.1 illustrates an example of this motion of a trapped particle. At position 1, the particle has maximum velocity relative to the potential. At position 2, it loses all its kinetic energy. When it reaches position 3 from 2, it attains the maximum velocity again but in an opposite direction. The particle finishes a full cycle of the bounce motion after reaching 4 and coming back to 1. In phase space, this cycle translates to a vortical trajectory as shown in Figure 1.1(b).

EHs are an excellent example of a BGK mode. An EH is supported by the balance between a positive potential and electrons trapped by the potential. It is well established by observations and simulations that EHs travel along the ambient magnetic $\mathbf{B}_0$. Figure

1.2 shows schematic representations of an EH in phase space, potential, and parallel electric field, respectively. The positive potential of an EH, as shown in Figure 1.2(b), traps a portion of electrons. The phase space density at the center of an EH is depleted, which forms a hole in phase space, and hence the name electron phase-space hole. The parallel electric field ($E_\parallel$) of an EH is typically a bipolar structure as shown in Figure 1.2(c). In observations, a solitary, bipolar signal in $E_\parallel$ is often a defining signature of an EH.

1.1.2 A brief history of EH study

Electron phase-space holes (EHs) were first discovered in early numerical simulations of electron two-stream instabilities and interpreted as a BGK mode [*Roberts and Berk*, 1967; *Morse and Nielson*, 1969]. Later, EHs were observed in Q-machine experiments [*Saeki et al.*, 1979; *Lynov et al.*, 1979], which gave rise to numerous theoretical studies of EHs. *Schamel* [1979] derived 1D stationary EH solutions that well described experimental results with a different approach from the BGK method. Instead of prescribing an EH potential, *Schamel* [1979] prescribed the distribution of the trapped particles and solved the stationary Vlasov-Poisson system for the EH potential. *Dupree* [1982] demonstrated that 1) EHs are a state of maximum entropy for constant mass, momentum, and energy, and 2) one large EH has a larger entropy than two small EHs, and thus EHs tend to coalesce. *Turikov* [1984] constructed an EH solution and studied the stability of EHs with simulations. He defined an EH Mach number, M, which is the ratio of the EH velocity (v_{EH}) to the electron temperature of the background plasmas (v_{Te}), namely, $M = v_{EH}/v_{Te}$. The simulations showed that the EH stability decreases as M increases if $M > 2$. *Schamel* [1986] reviewed experiments and theoretical studies of EHs, along with other electrostatic phase-space structures.

In space plasmas, EHs are often identified as solitary structures in electric field waveforms. Due to this solitary feature, EHs manifest themselves as bursty broadband enhancement in electric field spectra. In early space observations, electric field instruments did not have sufficiently high resolution to resolve the waveforms of EHs, and EHs were known as

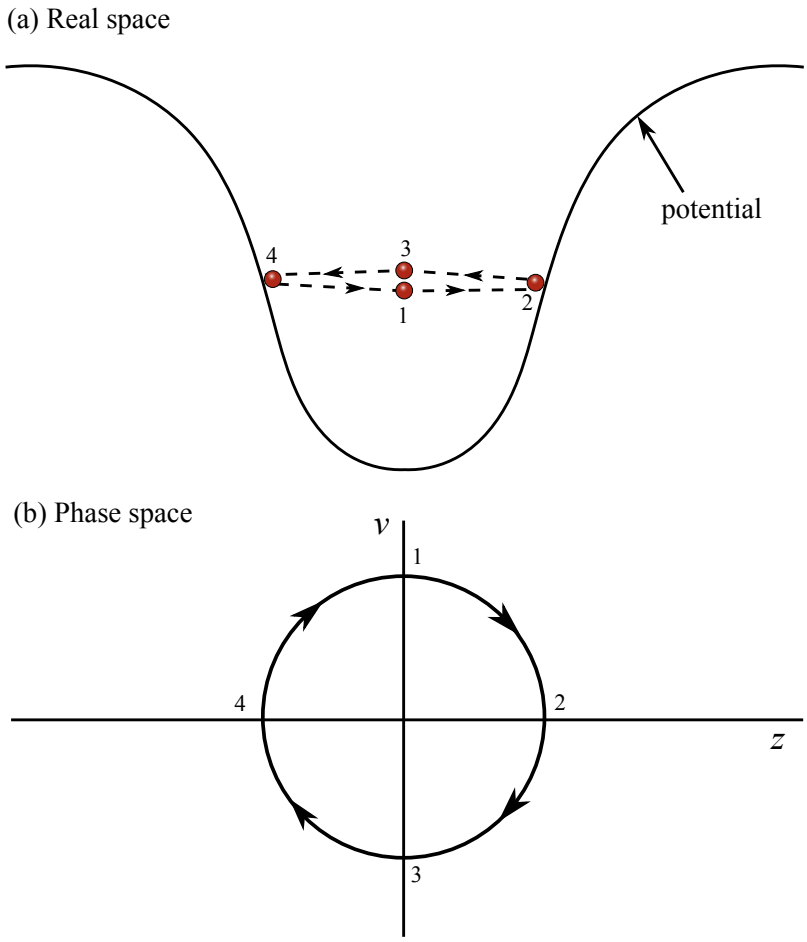

Figure 1.1: An example of 1D bounce motion of a trapped particle in (a) real space and (b) phase space in the reference frame of the potential.

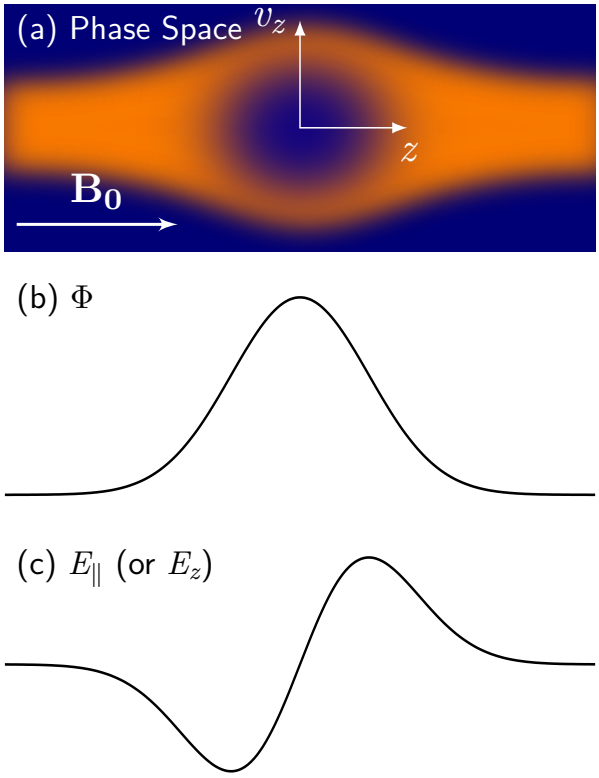

Figure 1.2: Schematic representations of an EH in (a) phase space, (b) potential, and (c) parallel electric field.

Broadband Electrostatic Noise (BEN) based on their spectral signatures [*Gurnett et al.*, 1976; *Gurnett and Frank*, 1977, 1978]. The EH waveforms were first resolved by the Geotail satellite in EH observations in the distant plasma sheet boundary layer (PSBL) with $X_{GSM} \sim -70R_E$ [*Matsumoto et al.*, 1994]. Since then, many more high-resolution EH observations have been made by various spacecraft in various regions, including Earth's auroral region [*Ergun et al.*, 1998a,b; *Mozer et al.*, 1997], high altitude polar magnetosphere [*Franz et al.*, 1998], inner-magnetosphere PSBL ($\sim 6R_E$) [*Cattell et al.*, 1998], the terrestrial bow shock transition region [*Bale et al.*, 1998], magnetopause and magnetosheath [*Cattell et al.*, 2002, 2003], and the solar wind [*Mangeney et al.*, 1999; *Huttunen et al.*, 2007]. Therefore, EHs appear to be ubiquitous in space plasmas.

Franz et al. [2005] provided a detailed historical review of EH studies. More recently, *Cattell et al.* [2005] reported Cluster observations of EHs during a reconnection event in the magnetotail at $\sim$18 R_E. *Retinò et al.* [2006] described solitary waves, which were possibly EHs, in a study of the separatrix region of a magnetic reconnection event observed by Cluster at the high-latitude duskside magnetopause. *Deng et al.* [2006] reported EHs associated with reconnection near the diffusion region and along the plasma sheet boundary layer by Geotail and Cluster. *Pickett et al.* [2009] reported Cluster observations of EHs associated with the onset of a super-substorm in the magnetotail around 18–19 R_E; in addition, they performed beam experiments with the University of California-Los Angeles Plasma Device (LAPD) and compared observations with experimental results. *Khotyaintsev et al.* [2010] presented observations of slow EHs observed by Cluster in the vicinity of a reconnection site in the Earth's magnetotail. *Hashimoto et al.* [2010] reported EH observations from SELENE (KAGUYA), a lunar mission, in the solar wind near the Moon and in the lunar wake. *Fox et al.* [2008] showed observations of EHs during magnetic reconnection experiments on the Versatile Toroidal Facility at MIT. *Lefebvre et al.* [2010] presented LAPD results of EHs generated by an electron beam injected into a magnetized low-β plasma column.

Recent EH observations and experiments refreshed theoretical interests in EHs. *Muschi-*

etti et al. [2000] demonstrated that the long-standing EH stability problem can be characterized by Ω_e/ω_b, where Ω_e is the gyrofrequency of local electrons, and ω_b the bounce frequency of trapped electrons. *Chen and Parks* [2002] constructed a 3D EH solution in magnetized plasmas. *Omura et al.* [1996] studied EH generation mechanisms via electron two-stream instabilities with 1D PIC simulations. *Singh et al.* [2000] studied the 3D structure of EHs and the evolution of EHs generated by electron beams. *Drake et al.* [2003] discovered EHs in magnetic reconnection simulations. *Umeda et al.* [2006] performed 2D electromagnetic PIC simulations to study the evolution of EHs for various electron temperatures and gyrofrequencies. *Lu et al.* [2008] conducted a parameter study of the perpendicular electric field of EHs. Most recently, *Singh et al.* [2011] performed mesoscale 2D PIC simulation of double layers and EHs and found that the fast-moving EHs are effective in transverse heating of cold electrons.

1.1.3 Generation and evolution of EHs

EHs are thought to be generated by electron beam instabilities [e.g., *Singh*, 2000; *Umeda et al.*, 2004] or by Buneman instabilities [e.g., *Goldman et al.*, 2008; *Che et al.*, 2010]. A common pattern of the generation and evolution of EHs is the following. First, the free energy of the system is released via instabilities and electrostatic waves are excited consequently. Next, the electrostatic waves will grow into a nonlinear stage and form a series of EHs adjacent to each other. Then, EHs coalesce as they evolve and eventually become solitary structures. Figure 1.3 illustrates such an evolution based on 1D Vlasov simulation results, in which the system initially consists of two relatively drifting electron components as shown in Figure 1.3(a). EHs keep coalescing and eventually only one EH is left in the system in this case as shown in Figure 1.3(f).

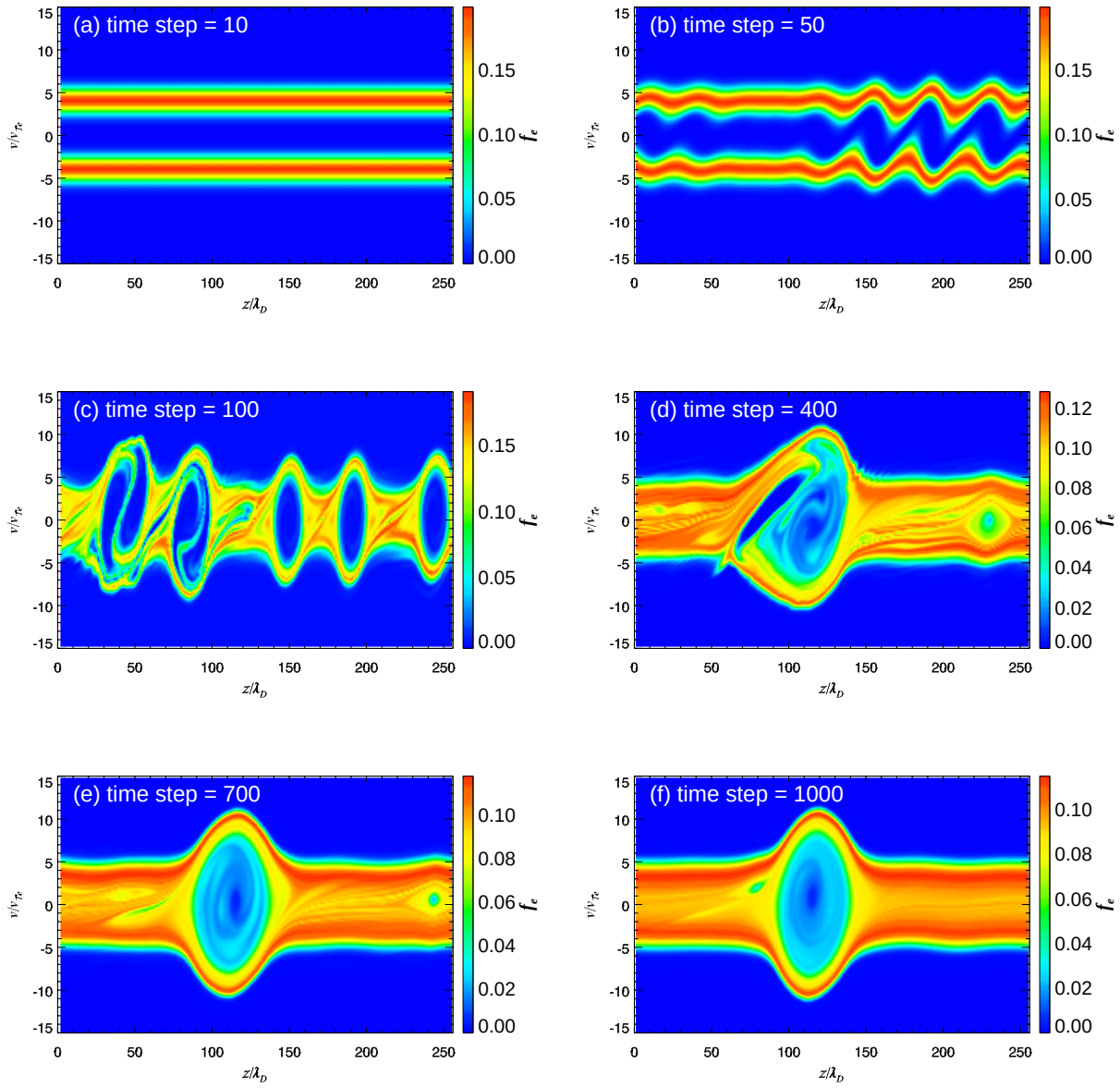

Figure 1.3: A 1D example of EH evolution in phase space. The color codes indicate the electron distribution function (f_e). z coordinates are normalized by the Debye length of the system (λ_D), and v coordinates normalized by the common thermal velocity of electron beams (v_{Te}). The time steps are labelled at the upper left corner of each panel.

1.1.4 Importance of EH study

EHs are excellent indicators of nonlinear processes in space plasmas. For instance, *Ergun et al.* [2001] reported EHs along with double layers in the downward current region of the Earth's auroral zone; *Khotyaintsev et al.* [2010] presented observations of slow EHs observed by Cluster in the vicinity of a reconnection site in the Earth's magnetotail; *Ergun et al.* [2009] showed EHs produced by double layers in the Earth's plasma sheet.

EHs can not only help us identify nonlinear processes in observations, but also be useful in understanding the nature of the source that generates the EHs. For example, what is the relation between the energy level of the source and the potential carried by EHs? Furthermore, as EHs propagate and eventually dissipate in space plasmas, what influence do they have on the plasma environment? To be able to answer these questions, further investigations are required to gain a more comprehensive understanding of EHs.

1.1.5 Electromagnetic EHs: New observations from THEMIS

The observational characteristics of EHs are almost always electrostatic, i.e., no magnetic field signals are associated with the observations of EHs. Exceptions of EHs with magnetic signals were reported with FAST and Polar observations [*Ergun et al.*, 1998a; *Mozer et al.*, 1997] in the Earth's auroral region. However, in those exceptions, the magnetic signals were perpendicular to the ambient magnetic field and *Ergun et al.* [1998a] attributed the perpendicular magnetic signals ($\delta B_\perp$) to the Lorentz transformation of the perpendicular electric signals ($\delta E_\perp$). In other words, there exists a reference frame where EH signals remain electrostatic. Therefore, those exceptions are still within the traditional BGK picture where EHs are electrostatic structures resulting from a balance between positive potentials and trapped electrons.

However, THEMIS observed EHs with magnetic signals present in all three magnetic field components in the plasma sheet boundary layer [*Andersson et al.*, 2009]. These EH

observations are termed electromagnetic EHs. Among the magnetic signals, the parallel magnetic signals ($\delta B_{\parallel}$) cannot be accounted for by the Lorentz transformation and are beyond the traditional BGK picture. Therefore, the $\delta B_{\parallel}$ signals raise an important question: *What physics are we missing in understanding EHs?* This work seeks to answer that question. In addition, a detailed analysis of the properties of the electromagnetic EHs, including velocities, potentials, and sizes, is provided in this work.

1.2 The Lunar Wake

The orbit of the moon is roughly a circle (mean radius $\sim 60R_E$) in the ecliptic plane with inclination $\sim 5^\circ$. Figure 1.4 illustrates the orbit of the Moon in the context of the solar wind and the Earth's magnetosphere. Based on the average magnetopause position from *Shue et al.* [1997] and the average bow shock position from *Peredo et al.* [1995], the percentages of the time that the Moon is in the solar wind, magnetosheath, and magnetosphere are $\sim$70%, $\sim$15%, $\sim$15%, respectively. Because the magnetosheath solar-wind flow is weakly shocked at the orbit of the Moon, the Moon encounters a supersonic flow even in the magnetosheath. Therefore, the Moon is immersed in the supersonic solar wind $\sim$85% of the time.

When the Moon is immersed in the solar wind, solar wind plasmas that impinge on the Moon are absorbed by the lunar surface creating a depleted wake region downstream, which is referred to as the lunar wake. The Moon does not have an intrinsic magnetic field, and the conductivity of the Moon is so low that the motion of the solar wind magnetic field does not induce a significant diamagnetic field. Therefore, there is no global magnetosphere of the Moon. As a result, the solar wind magnetic field penetrates the Moon with little disturbance [*Ness et al.*, 1967; *Ness*, 1972].

The density gradient between the lunar wake and the solar wind drives solar wind plasmas to refill the lunar wake along magnetic field lines, in which a rarefaction wave front creates a boundary of the lunar wake [*Johnson and Midgley*, 1968]. Ions and electrons undergo ambipolar diffusion during the refilling, in which electrons rush into the wake ahead

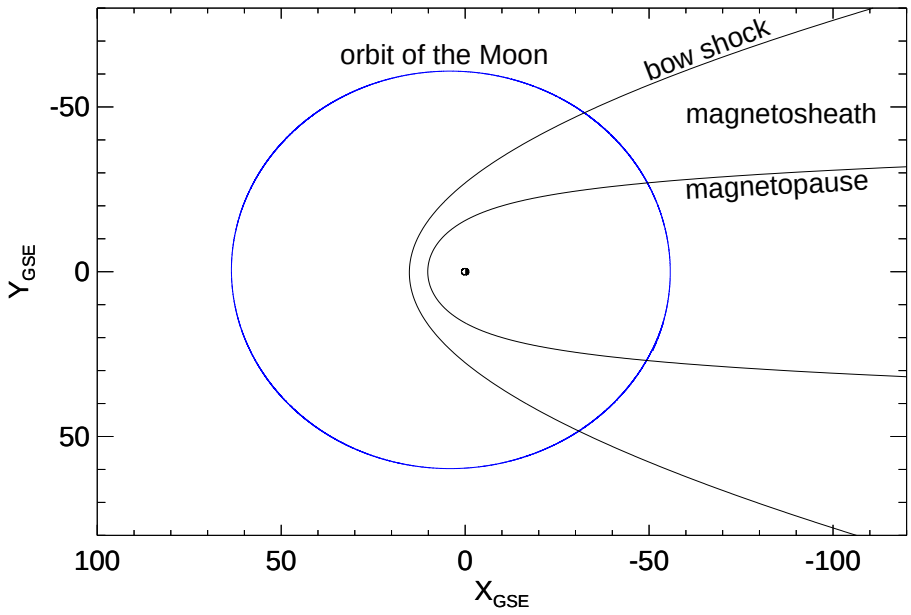

Figure 1.4: The ecliptic projection of the Moon orbit (the blue circle) in the context of the Earth's magnetosphere and the solar wind. The two black open curves indicate the average positions of the magnetopause and the bow shock, respectively. The space between the magnetopause and the bow shock is the magnetosheath.

of ions and cause the wake to become negatively charged. The potential gradient in the wake in turn sets up an ambipolar electric field that accelerates ions into the wake. Figure 1.5 illustrates the refilling process in the lunar wake.

Early studies of the lunar wake are mostly based on observations from the U.S. Explorer 35 and the Apollo program in the 1960s and 1970s (see *Ness* [1972] and *Schubert and Lichtenstein* [1974] for review). The Wind spacecraft swung by the lunar wake at roughly 7 R_L (lunar radius) downstream of the Moon for a gravity assist and provided observations of the wake with modern plasma instruments [*Ogilvie et al.*, 1996; *Owen et al.*, 1996; *Farrell et al.*, 1996; *Kellogg et al.*, 1996; *Bosqued et al.*, 1996], which drove a series of investigations of the dynamics associated with the lunar wake [*Bale et al.*, 1997; *Bale*, 1997; *Farrell et al.*, 1998; *Birch and Chapman*, 2001, 2002; *Nakagawa et al.*, 2003; *Kallio*, 2005]. Among recent lunar missions, the ARTEMIS mission [*Angelopoulos*, 2010], which is derived from the two outermost satellites (known as P1 and P2, or THB and THC) of the THEMIS mission [*Angelopoulos*, 2008], is able to cover an extensive range of the lunar wake (∼1.1–12 R_L selenocentric after lunar orbit insertion). Other missions, including the Lunar Prospector, SMART-1, Kaguya, Change'e 1 and 2, Chandrayaan-1, and the Lunar Reconnaissance Orbiter, are generally lower-altitude orbiters.

During the transition from orbiting the Earth to orbiting the Moon, the ARTEMIS P1 spacecraft made its first lunar-wake flyby ∼3.5 R_L downstream from the Moon on 13 February 2010, during which the Moon was in the solar wind at ∼(63, -9, 2.5)R_E in GSE coordinates. Detailed observations of magnetic fields and plasma properties during this flyby were reported by *Halekas et al.* [2011], and a global simulation of this flyby was performed by *Wiehle et al.* [2011].

This work also uses the observations from the lunar-wake flyby introduced above to study the dynamics of the wake. The focus of this work is on the electrostatic waves observed on the outbound side of the flyby. One motivation of this work is to derive the wavelengths and phase velocities of those waves using interferometric techniques. Although plasma waves

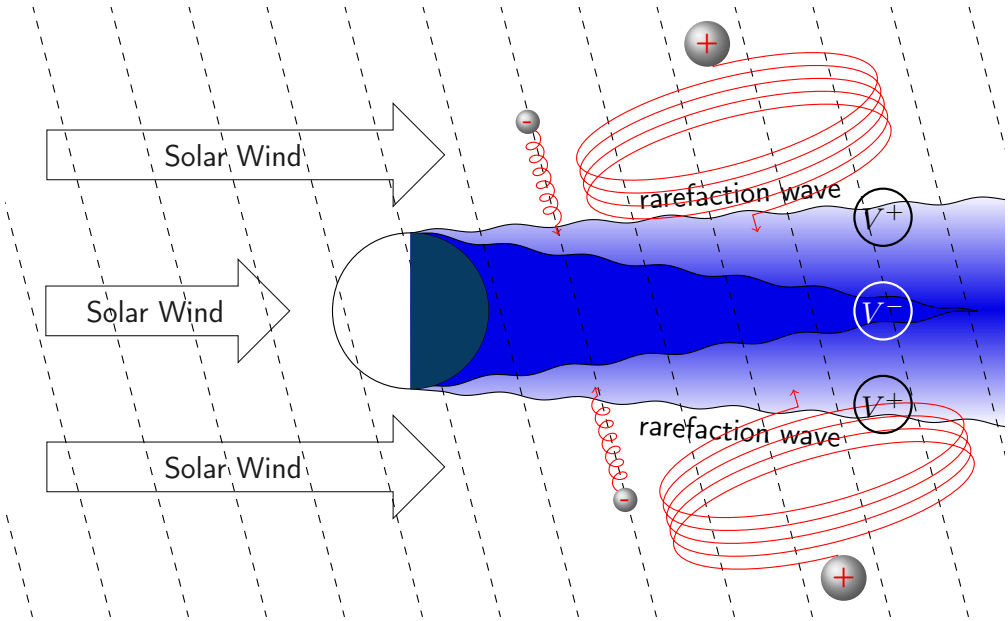

Figure 1.5: An illustration of the refilling of the lunar wake, which is confined by a rarefaction wave front. The central circle with the right half filled represents the Moon. The oblique dashed lines represent the solar wind magnetic field. The small gray balls labelled with a minus sign represent electrons, whereas the large gray balls labelled with a plus sign represent ions. The V^- sign indicates the negative wake potential, whereas the V^+ signs indicate higher potentials on the wake boundaries than inside the wake.

were previously reported with observations from the Wind spacecraft [*Kellogg et al.*, 1996], the derivation of wavelength and phase velocity is unprecedented and helps to provide a more comprehensive understanding of plasma wave properties in the lunar wake. Another motivation of this work is to identify the mode of the observed electrostatic waves. *Kellogg et al.* [1996] reported waves with similar frequencies, but was unable to identify the mode of those waves. Thus, identifying the mode of such waves can extend our understandings of the nature of the waves.

In this work, two interferometry techniques, cross-spectrum analysis and cross-correlation analysis [*Labelle and Kintner*, 1989], are used to derive wavelength and phase velocity. Similar previous work includes *Angelopoulos et al.* [2001] and *Ergun et al.* [1991]. 1D Vlasov simulations are carried out to identify the mode of the observed electrostatic waves.

1.3 Turbulence

The research of turbulence dates back to more than a century ago. Osborne Reynolds carried out the first systematic work on turbulence in 1883 with pipe flow experiments [*Reynolds*, 1883]. He showed that the flow becomes turbulent (or irregular) when the dimensionless ratio $\mathrm{Re} = UL/\nu$, later named the Reynolds number by the German theoretical physicist Arnold Sommerfeld [*Rott*, 1990], exceeds a certain critical value. (Here U is the velocity scale, L is the length scale, and ν is the kinematic viscosity.) In 1922, Lewis Richardson proposed a turbulent energy cascade from large eddies to small eddies and eventually to viscosity scale in a rhyming verse: "*big whirls have little whirls that feed on their velocity, and little whirls have lesser whirls and so on to viscosity—in the molecular sense*" [*Richardson*, 2007, p.66]. Such a spectral energy cascade is at the heart of our present understanding of turbulent flows.

The coupling of different scales is via nonlinear terms in the governing equations of the system, which can be understood from the convolution theorem. To simplify the problem, we limit ourselves to a 1D system. Suppose $f(x)g(x)$ is a nonlinear term in the system

equations. Fourier transforming the system from x-space to k-space, we have

$$\mathcal{F}\{f(x)g(x)\} = f(k) * g(k) = \int_{-\infty}^{\infty} f(k)g(k-k')dk', \tag{1.1}$$

where $\mathcal{F}\{\ \}$ represents the Fourier transform, $f(k) = \mathcal{F}\{f(x)\}$, and $g(k) = \mathcal{F}\{g(x)\}$. Equation (1.1) indicates that scale k is coupled with all the other scales.

The classical turbulent energy cascade is generally considered to consist of three scales from large to small: injection scale, inertial scale, and dissipation scale. Figure 1.6 illustrates the three scales via a textbook neutral-fluid turbulence spectrum. Among the three scales, the inertial scale is generally assumed to be dissipation-free, and its spectral slope is independent on the energy supply and is determined by the nonlinear interactions in the system. Therefore, the spectral slope in the inertial scale reflects the dynamics of the system. (A spectral slope in a log-log plot is characterized by the value of the power index α as in the form of $k^{-\alpha}$). *Kolmogorov* [1941] showed that the spectral energy density E_k follows a power law $E_k \sim k^{-5/3}$ for the inertial scale in neutral fluids under the assumptions of isotropy and incompressibility, which has been verified by numerous neutral-fluid turbulence experiments (see *Frisch* [1995] and references therein).

The dynamics of plasma differs from that of a neutral fluid. There are several nonlinear terms in plasma equations that have different importance at different scales for plasmas. It is possible that E_k can have a changing slope within the inertial range for plasmas, compared to the universal Kolmogorov $k^{-5/3}$ law for neutral fluids. *Iroshnikov* [1964] and *Kraichnan* [1965] showed that $E_k \sim k^{-3/2}$ in the inertial scales of homogeneous MHD turbulence. With 2D electron MHD turbulence simulations, *Biskamp et al.* [1996] showed that, below the ion inertial length c/ω_{pi}, the energy spectral density E_k follows $k^{-5/3}$ for $kd_e > 1$ and $k^{-7/3}$ for $kd_e < 1$, where $d_e = c/\omega_{pe}$ is the electron inertial length. In the framework of Hall MHD, *Krishan and Mahajan* [2004] suggested that the E_k curve steepen from $k^{-5/3}$ to $k^{-\alpha_1}$ with $\alpha_1 \simeq 3$–4 in the inertial range. With 3D Hall MHD simulations, *Galtier and Buchlin* [2007] found that the magnetic energy spectrum curve steepens from a Kolmogorov-type $k^{-5/3}$

spectrum to a $k^{-7/3}$ spectrum if the magnetic energy overtakes the kinetic energy, or to a $k^{-11/3}$ spectrum in the opposite case.

The focus of this work is on the turbulent electric and magnetic fields in the Earth's magnetotail, primarily in the plasma sheet. A number of studies have been published on turbulence in the Earth's plasma sheet. Among others, *Hoshino et al.* [1994] studied turbulent structures with magnetic field data observed by Geotail in the distant tail ($X_{GSM} \sim -200$ R_E) and found that the power spectrum of magnetic field as a function of frequency turns around 0.04 Hz from a more Kolmogorov-like slope at lower frequencies to a steeper slope at higher frequencies. *Borovsky et al.* [1997] analyzed ten several-hour-long intervals of single-point measurements of flow velocity and magnetic field from the ISEE-2 satellite at a distance around 20 R_E in the Earth's plasma sheet and found that the plasma flows and magnetic fields appear to be turbulent. In a follow-up paper, *Borovsky and Funsten* [2003] discussed the dynamics, dissipation, and driving of turbulence in the plasma sheet. They concluded that the plasma sheet turbulence is primarily eddy-dominated in the MHD scales. *Weygand et al.* [2005] studied MHD turbulence in the plasma sheet with Cluster data and concluded that the turbulence in the plasma sheet is likely to be intermittent.

Previous studies of turbulence in the plasma sheet were primarily based on magnetic fields and flow velocities. As an important aspect of plasma dynamics, statistical features of turbulent electric fields have yet to be addressed. Therefore, one motivation of my work is to find statistical features of turbulence in plasmas combining both electric and magnetic fields. In addition, it is interesting to see the statistical features of the Poynting flux in the plasma sheet, which can shed light on the energy coupling between the ionosphere and the magnetosphere. (Both electric and magnetic fields are required in order to calculate the Poynting flux.) Another motivation of my work is to extend our perspectives of turbulence from MHD scales into kinetic scales. The frequency range of previous studies is primarily within the MHD regime. However, using THEMIS high-resolution data, one can study turbulence in plasmas in both MHD and kinetic scales.

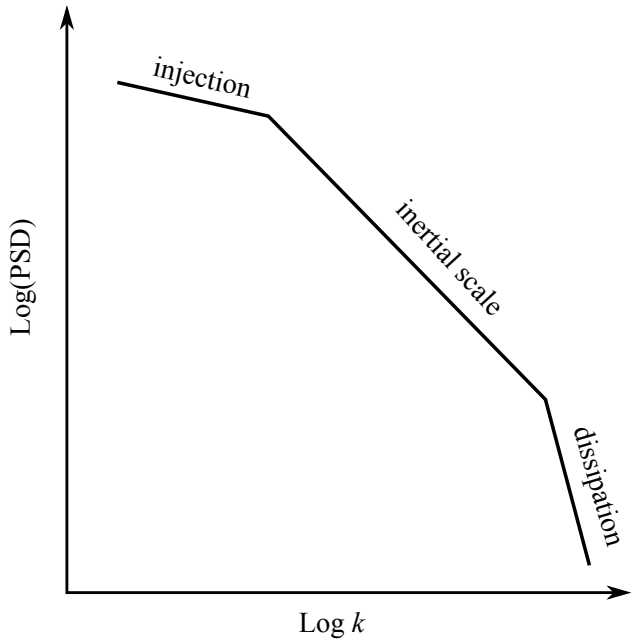

Figure 1.6: Illustration of turbulence spectrum

.

1.4 Organization

In Chapter 2, the observations of electromagnetic EHs are analyzed and a model for electromagnetic EHs is presented. In Chapter 3, kinetic instabilities observed during the first lunar-wake flyby of ARTEMIS are analyzed with interferometry techniques and Vlasov simulations. In Chapter 4, a statistical study of turbulent electric field and magnetic field observations by THEMIS in the Earth's magnetotail is presented. This work concludes with a brief discussion of future work.

Chapter 2

Electromagnetic Electron Phase-Space Holes

On March 28, 2008, the THEMIS A (THA) spacecraft observed unusual EHs in the plasma sheet boundary layer. The observed EHs had large electric field amplitude ($\sim$100 mV/m) compared to previous observations ($\lesssim$ 50 mV/m) [*Franz et al.*, 2005; *Cattell et al.*, 2005; *Pickett et al.*, 2004] and most other THEMIS observations. More important, the EHs had signals in all three magnetic field components, which had not been reported previously. Further, some physical quantities, such as velocities, sizes, and potentials, that are derived from these observations also show uncommon features. The velocities are roughly as fast as one-third of the speed of light. The sizes are tens of the local Debye length (λ_D), as opposed to most EHs observations where EHs are reported with sizes of several λ_D. The potentials are comparable to local electron temperatures (i.e., $e\Delta\Phi/T_e \sim 1$), as opposed to the most common case $e\Delta\Phi/T_e \ll 1$. These unusual features of the observed EHs provoke questions such as how they were generated and what impact they had on the plasma environment.

2.1 Review of the Observations

Figure 2.1 shows a background overview of the electromagnetic EH event observed by THA on 28 March 2008. The electromagnetic EHs were recorded in a $\sim$16 s "wave burst" from 11:14:41 UT to 11:47:57 UT. The term "wave burst" refers to THEMIS field data with high temporal resolution (sampled at $\sim$8 kHz or $\sim$16 kHz) and short durations ($\lesssim$ 20 s). The vertical dashed line across Figure 2.1 indicates the mid-time of the $\sim$16 s wave burst.

The spacecraft was located at ($x_{GSM} \sim -6.0\ R_E$, $y_{GSM} \sim 7.4\ R_E$, $z_{GSM} \sim -1.6\ R_E$) during the event, as labelled at the bottom of the figure.

Figures 2.1(a) and 2.1(b) show the differential energy flux of electrons and ions, respectively, where the color scales and the y axes indicate the magnitude of the differential energy flux and the energy level, respectively. Data from both the electrostatic analyzer (ESA) [*McFadden et al.*, 2008] and the solid-state telescope (SST) are used in these two figures. The white gap at ∼25 keV in Figure 2.1(b) is due to the instrument energy range gap between the ESA and the SST. In both figures, the enhanced energy flux in red color at high-energy levels (above 1000 eV) on both sides of the event indicates that the spacecraft was in the plasma sheet during that period. (Enhanced differential energy flux at high energy levels is a common feature of the plasma sheet.) The high energy flux in the bottom of Figure 2.1(a) (dark red area) is from photoelectrons emitted by the spacecraft. At the time of the ∼16 s wave burst, the energy flux of plasmas, as well as the plasma densities shown in Figure 2.1(d), was reduced compared to the plasma sheet, indicating that the spacecraft was in the plasma sheet boundary layer at that time.

Figure 2.1(c) shows parallel and perpendicular temperatures of electrons from ESA data. At the time of the ∼16 s wave burst, $T_{e\parallel} \sim 6$ keV and $T_{e\perp} \sim 3$ keV from Figure 2.1(c). Figure 2.1(d) shows that the plasma number density is ∼0.02 cm^{-3} at that time. Figure 2.1(e) shows the DC magnetic field measurements from the onboard fluxgate magnetometer (FGM) [*Auster et al.*, 2008] in GSM coordinates. The total magnetic field (B_0) is ∼50 nT during the ∼16 s wave burst.

Figure 2.2 shows ∼0.2 s of the electromagnetic perturbations $\delta\mathbf{E}$ and $\delta\mathbf{B}$ (filtered from ∼5 Hz to ∼3.3 kHz; sampled at 8192 Hz) from the ∼16 s wave burst, demonstrating the detailed structures of the electric and magnetic field signals of the electromagnetic EHs. The data are presented in a field-aligned coordinate (FAC) system. (For electric and magnetic field observations, the FAC system is defined as such that the z-axis is in the same direction of the ambient magnetic field $\mathbf{B}_0$, the x-axis lies in the spin plane of the spacecraft, and

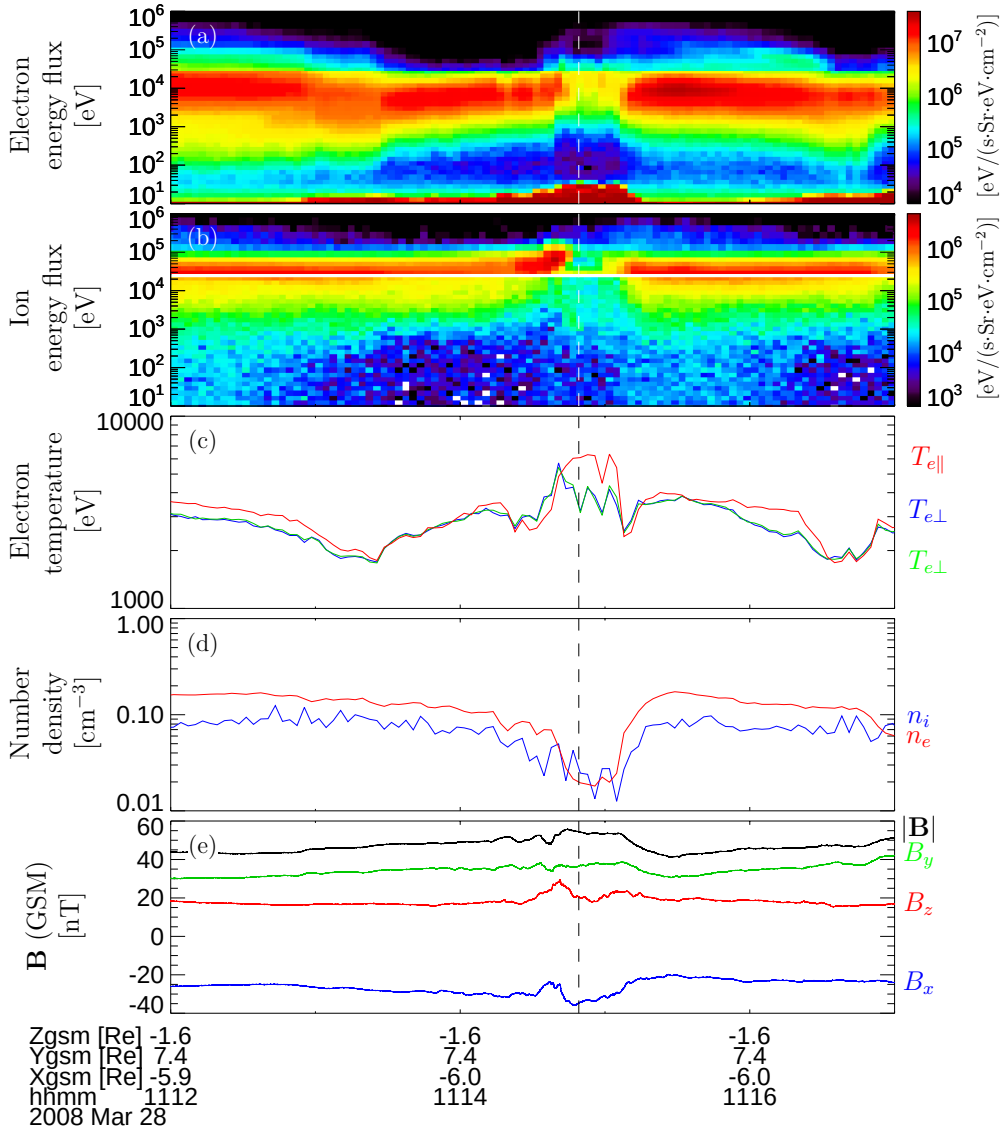

Figure 2.1: Five-minute overview observations of the electromagnetic EH event on 28 March 2008 from THA.

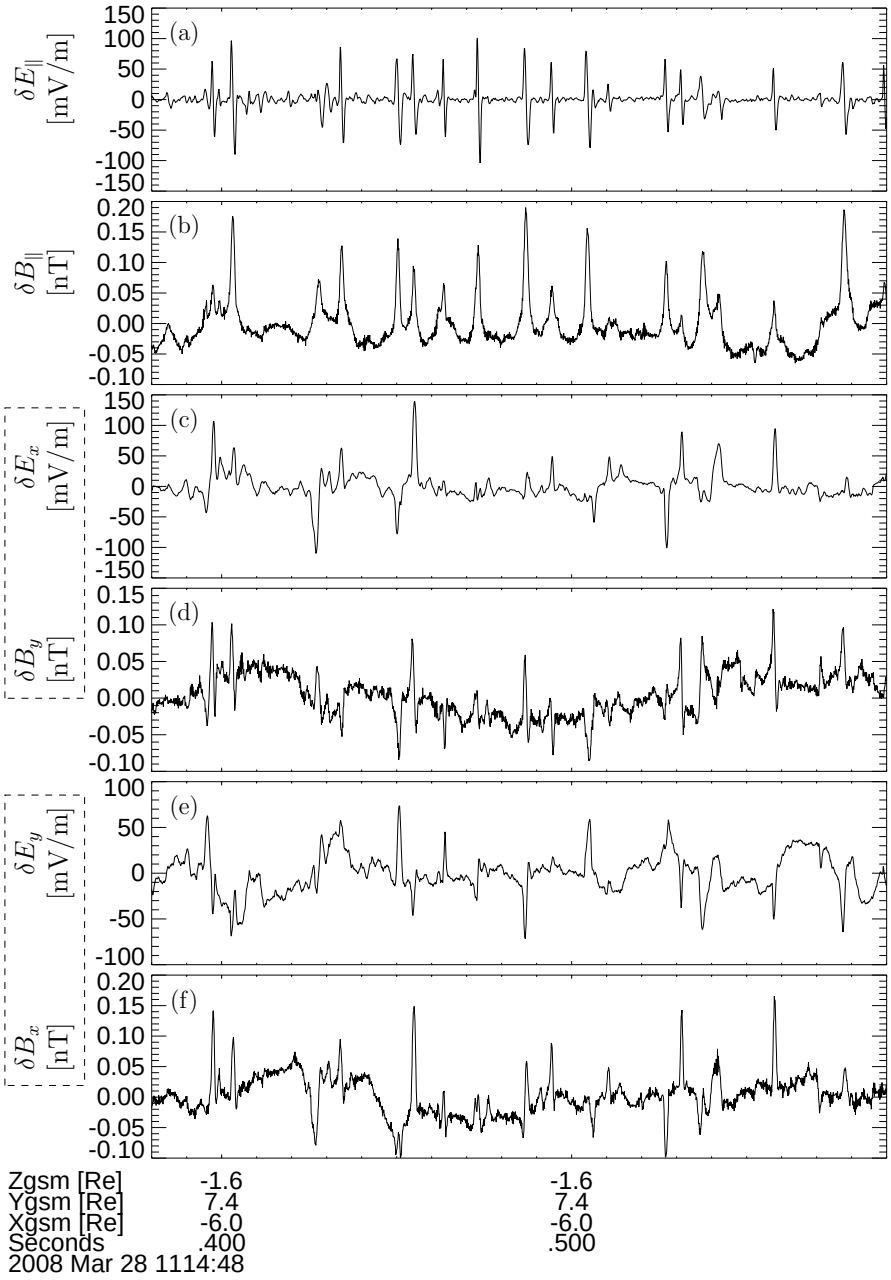

Figure 2.2: ∼0.2 s of the electromagnetic EH observations.

the y-axis completes the FAC system as a right-handed coordinate system.) The $\delta\mathbf{E}$ signals are from the THEMIS electric field instrument (EFI) [*Bonnell et al.*, 2008], whereas the $\delta\mathbf{B}$ signals are from the THEMIS searchcoil magnetometer (SCM) [*Roux et al.*, 2008]. The x and y components are perpendicular to $\mathbf{B_0}$.

The solitary spiky bipolar $\delta E_\parallel$ signals are defining signatures of EHs in observations and are used to identify EHs in the data [e.g. *Matsumoto et al.*, 1994; *Ergun et al.*, 1998a]. As shown in Figure 2.2(a), the polarities of $\delta E_\parallel$ of these EHs are identical, with a positive peak followed by a negative peak in time, indicating that the EHs were travelling in the same direction and likely from the same source. As shown in Figure 2.1(e), the GSM B_x was negative during the event, which indicates that the field lines were anti-earthward. The first-positive-then-negative polarity of $\delta E_\parallel$ signals indicates that the EHs were travelling in the same direction of $\mathbf{B_0}$, namely, anti-earthward.

The positive, unipolar $\delta B_\parallel$ signals shown in Figure 2.2(b) are a unique observational feature of the electromagnetic EHs in the ∼16 s wave burst, and their interpretation will be discussed in Section 2.2. The amplitudes of $\delta B_\parallel$ signals are up to ∼0.2 nT.

In Figures 2.2(c–f), two dashed boxes grouped δE_x and δB_y, δE_y and δB_x together, respectively, based on their relations in the Lorentz transformation as discussed later. The δE_x and δB_y signals are approximately correlated, whereas the δE_y and δB_x signals are approximately anti-correlated.

2.2 Interpretations and an EH Model with Electron $\delta\mathbf{E} \times \mathbf{B_0}$ Drift Current

Ergun et al. [1998b] reported EHs with perpendicular magnetic field perturbations ($\delta B_\perp$). They found that $c^2 \Delta B_\perp / \Delta E_\perp \cong v_{delay}$, where v_{delay} is the EH velocity derived from the time delay between two physically separated EFI antennas, suggesting that the measured EHs were electrostatic in their rest frame and that the perturbations in $\delta B_\perp$ signals were due to the Lorentz transformation of $\delta E_\perp$ signals from the EH frame to the spacecraft frame. Their results indicate that the Lorentz transformation may be a key to understanding the

$\delta B_\perp$ signals of the electromagnetic EHs as shown in Figure 2.2.

The exact Lorentz transformation from the EH frame to the spacecraft frame in FAC is the following [*Jackson*, 1998, p.558, changed to SI]:

$$\begin{aligned} \delta E_\parallel &= \delta E'_\parallel & \delta B_\parallel &= \delta B_\parallel{}' \\ \delta E_x &= \gamma(\delta E'_x + v_{EH}\delta B'_y) & \delta B_x &= \gamma(\delta B'_x - \frac{v_{EH}}{c^2}\delta E'_y) \\ \delta E_y &= \gamma(\delta E'_y - v_{EH}\delta B'_x) & \delta B_y &= \gamma(\delta B'_y + \frac{v_{EH}}{c^2}\delta E'_x) \end{aligned} \tag{2.1}$$

where $\gamma = (1 - v_{EH}^2/c^2)^{-1/2}$. Assuming that the EHs are electrostatic in their rest frame (i.e., $\delta B' = 0$), from the equation set (2.1) we obtain:

$$\delta B_x \approx -\frac{v_{EH}}{c^2}\delta E_y, \tag{2.2}$$

$$\delta B_y \approx \frac{v_{EH}}{c^2}\delta E_x. \tag{2.3}$$

Equations (2.2) and (2.3) show that δB_x and δE_y are anti-correlated, and that δB_y and δE_x are correlated, which are highly consistent with the observations shown in Figure 2.2. Although v_{delay} was not available for the electromagnetic EHs in the ∼16 s wave burst, this correlation consistency strongly suggests that the $\delta B_\perp$ perturbations can be roughly understood as Lorentz transformation results of $\delta E_\perp$.

However, the Lorentz transformation cannot explain the observed positive, unipolar $\delta B_\parallel$ signals. In this work, they are interpreted as results from an electron $\delta\mathbf{E} \times \mathbf{B_0}$ drift current. Figure 2.3 shows an EH model with such a current.

Figure 2.3(a) and 2.3(b) are two cross-sections of the EH model in the FAC x-y plane and x-z plane, respectively. The red areas represent the EH. In Figure 2.3(a), the black arrows represent the electrostatic fields ($\delta\mathbf{E}'$) from the electrostatic BGK potential of the EH, and the yellow dot-circles represent the ambient magnetic fields ($\mathbf{B_0}$) pointing out of the paper. The $\delta\mathbf{E}'$ fields point radially outwards because the BGK potential peaks positively at the center of the EH. The blue arrows and symbols in Figure 2.3(a) and 2.3(b), respectively, represent the azimuthal current $\mathbf{J}_\phi$ generated by the $\delta\mathbf{E} \times \mathbf{B_0}$ drift of electrons. The black

curved arrows crossing the EH in Figure 2.3(b) represent the magnetic field $\delta\mathbf{B}'$ induced by $\mathbf{J}_\phi$. The dashed line in Figure 2.3(b) represents an imaginary spacecraft track, and the small object below it represents the spacecraft (SC). One can see that the parallel component of $\delta\mathbf{B}'$ in the model is predominantly of the same direction of $\mathbf{B_0}$, and hence the spacecraft should mostly record positive unipolar $\delta B_\parallel$ structures as shown in Figure 2.2.

Based on this model, a Gaussian potential such as the following

$$\Phi = \Phi_0 e^{-\frac{r^2}{2l_\perp^2}} e^{-\frac{z^2}{2l_\parallel^2}}, \tag{2.4}$$

can be used to estimate $\delta\mathbf{B}'$, where Φ_0 is the central potential of the EH, r and z are cylindrical coordinates corresponding to the FAC ($r = \sqrt{x^2+y^2}$), and $l_\perp(l_\parallel)$ is the half perpendicular(parallel) size of the EH (full sizes $L_\perp = 2l_\perp$, $L_\parallel = 2l_\parallel$).

Given Equation (2.4), assuming a uniform background electron density (n_0), one obtains $\delta\mathbf{E}'$ and $\mathbf{J}_\phi$ as

$$\delta\mathbf{E}' = -\boldsymbol{\nabla}\Phi = \frac{r}{l_\perp^2}\Phi\hat{\mathbf{r}} + \frac{z}{l_\parallel^2}\Phi\hat{\mathbf{z}}, \tag{2.5}$$

$$\mathbf{J}_\phi \approx -en_0\frac{\delta\mathbf{E}'\times\mathbf{B_0}}{B_0^2} = \frac{en_0 r}{B_0 l_\perp^2}\Phi\hat{\boldsymbol{\phi}}, \tag{2.6}$$

where $\hat{\mathbf{r}}$, $\hat{\mathbf{z}}$, and $\hat{\boldsymbol{\phi}}$ are the unit vectors of the cylindrical coordinate system. $\delta\mathbf{B}'$ is obtained with the Biot-Savart law [*Jackson*, 1998, p.178]

$$\begin{aligned}\delta\mathbf{B}'(\mathbf{x}) &= \frac{\mu_0}{4\pi}\int \mathbf{J}_\phi(\mathbf{x}')\times\frac{\mathbf{x}-\mathbf{x}'}{|\mathbf{x}-\mathbf{x}'|^{\mathbf{3}}}d^3x' \\ &= \frac{en_0\mu_0}{B_0 4\pi}\int \frac{x'}{l_\perp^2}\Phi\hat{\boldsymbol{\phi}}\times\frac{\mathbf{x}-\mathbf{x}'}{|\mathbf{x}-\mathbf{x}'|^{\mathbf{3}}}d^3x'\end{aligned} \tag{2.7}$$

In general, numerical integration is required to obtain $\delta\mathbf{B}'$ from Equation (2.7) for an arbitrary location inside the EH. However, the central $\delta\mathbf{B}'$ can be obtained analytically as

$$\delta\mathbf{B}'(r=0,z=0) = \frac{e\Phi_0\mu_0 n_0}{B_0}g(l_\perp/l_\parallel)\hat{\mathbf{z}} \tag{2.8}$$

where

$$g(l_\perp/l_\parallel) = \mathrm{Re}\left[\frac{1-\frac{l_\perp^2}{l_\parallel^2}+\frac{l_\perp^2}{l_\parallel^2}\arccos(\frac{l_\parallel}{l_\perp})\sqrt{\frac{l_\perp^2}{l_\parallel^2}-1}}{\left(1-\frac{l_\perp^2}{l_\parallel^2}\right)^2}\right] \tag{2.9}$$

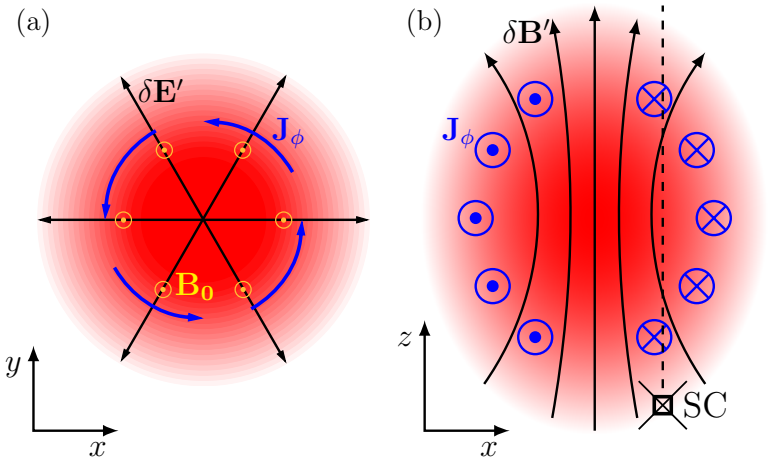

Figure 2.3: An EH model with electron $\delta\mathbf{E} \times \mathbf{B_0}$ drift current.

Note that the dimensionless factor g only depends on the ratio $l_\perp/l_\parallel$, which characterizes the shape of the EH and hence is called a geometric factor. Figure 2.4 shows the behavior of g as a function of $l_\perp/l_\parallel$.

2.3 Conditions for Establishing $\delta\mathbf{E} \times \mathbf{B_0}$ Drift Current in EHs

One key question about the EH model shown in Section 2.2 is whether the electron $\delta\mathbf{E} \times \mathbf{B_0}$ drift current can be established. The $\delta\mathbf{E} \times \mathbf{B_0}$ drift motion stems from the gyromotion of particles. Therefore, the most relevant scales are the perpendicular EH size ($l_\perp$) with respect to the gyroradius of particles (ρ), and the EH transit time (δt) with respect to the gyroperiod of particles (t_c). A test-particle code was developed to address the conditions of $l_\perp$ and δt for the formation of $\delta\mathbf{E} \times \mathbf{B_0}$ drift current. As discussed in *Chen and Parks* [2002], the $\delta\mathbf{E} \times \mathbf{B_0}$ drift of electrons does not substantially affect the BGK equilibrium of an 3D EH in magnetized plasmas. Therefore, a test-particle simulation model is appropriate for this investigation.

2.3.1 Simulation model

The test-particle code is a 2D, particle-in-cell (PIC) code, in which the widely-used Boris method is implemented to update particle velocities and a first-order shape function is used to obtain the current density on the grid (see *Birdsall and Langdon* [1985]). Particles are initialized with a uniform density in the x-y plane perpendicular to $\mathbf{B}_0$, Maxwellian velocity distributions in v_x and v_y, and a uniform $v_\parallel$ (equivalent to v_z). To cover a full distribution of $v_\parallel$, multiple runs with various values of $v_\parallel$ are required.

Figure 2.5 illustrates the simulation model. The potential of the EH is assumed with a Gaussian shape as in Equation (2.4). As a simulation goes, the simulation plane sweeps through the EH. In a typical case, an azimuthal current first gradually forms as the simulation plane moves towards the center of the EH, and then gradually vanishes as the simulation plane moves out of the EH.

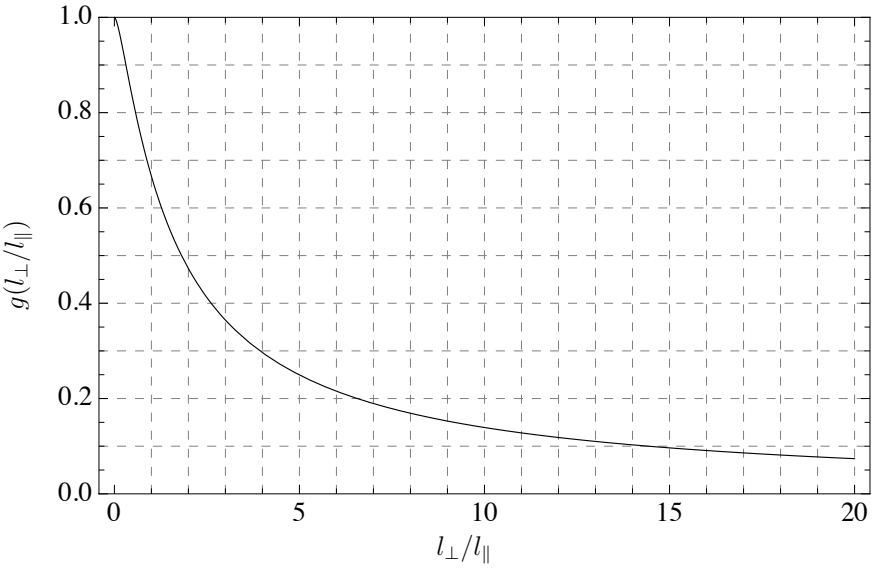

Figure 2.4: The geometric factor, g, as a function of $l_\perp/l_\parallel$.

With periodic boundary conditions, the simulation plane expands over a $N_x \times N_y = 100 \times 100$ grid with $-L/2 \leq x \leq L/2$ and $-L/2 \leq y \leq L/2$, where $L \geq 6l_\perp$ (typically $L = 10l_\perp$). The number of total particles is 20 million with ∼2000 per cell.

2.3.2 Simulation results

The major diagnostics of the investigation is the maximum current density in the simulation plane (J_{max}) normalized by the theoretical maximum current density (J_0) that is calculated according to Equation (2.6). J_{max} is calculated as the average of the current density over the ring between $r = l_\perp - 0.1l_\perp$ and $r = l_\perp + 0.1l_\perp$, a region where the maximum $\delta\mathbf{E} \times \mathbf{B_0}$ drift current is expected.

As mentioned earlier, multiple runs are required to cover the full distribution of $v_\parallel$. The J_{max} of a full distribution of $v_\parallel$ is calculated as

$$J_{max} = \int_{\infty}^{-\infty} J'_{max} f_\parallel(v_\parallel; v_{EH}) dv_\parallel, \tag{2.10}$$

where $f_\parallel(v_\parallel; v_{EH}) = \frac{1}{\sqrt{2\pi v_t^2}} \exp\left[-\frac{(v_\parallel + v_{EH})^2}{2v_t^2}\right]$, v_t is the thermal velocity of the particles, and J'_{max} is obtained from a single simulation run.

Figure 2.6(a) shows the effect of $l_\perp$ on the formation of the $\delta\mathbf{E} \times \mathbf{B_0}$ drift current. The results are from simulation runs with $\delta t \approx 1.6t_c$, where t_c is the gyroperiod of the particles. The $\delta\mathbf{E} \times \mathbf{B_0}$ drift current from the simulation asymptotically approaches the theoretical value as $l_\perp$ increases. When $l_\perp \gtrsim 10\rho$, the $\delta\mathbf{E} \times \mathbf{B_0}$ drift current from the simulation is quite close to the theoretical value (i.e., $J'_{max}/J_0 \approx 1$), suggesting that $l_\perp \gtrsim 10\rho$ is required to fully establish the $\delta\mathbf{E} \times \mathbf{B_0}$ drift current.

Figure 2.6(b) shows the effect of the transit time (δt) with respect to the gyroperiod of the particles (t_c) on the formation of the $\delta\mathbf{E} \times \mathbf{B_0}$ drift current. δt is calculated by $L_\parallel/v_{EH}$ where $L_\parallel$ is 20 gyroradii of the particles. One can see that the $\delta\mathbf{E} \times \mathbf{B_0}$ drift current quickly drops as δt decreases when $\delta t/t_c$ is less than ∼0.5. When $\delta t/t_c \gtrsim 1$, the simulation results approximately match the theoretical results. The overshoot between $\delta t/t_c = 0.5$ and

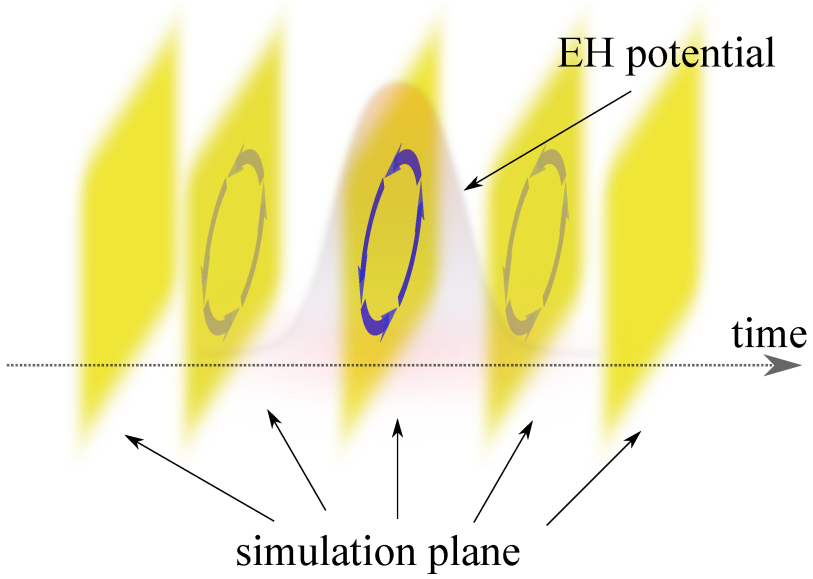

Figure 2.5: An illustration of the test-particle simulation model of $\delta\mathbf{E} \times \mathbf{B_0}$ drift current, where the 2D simulation plane passes through an EH with a Gaussian potential shape. The circular arrows represents the azimuthal $\delta\mathbf{E} \times \mathbf{B_0}$ drift current.

$\delta t/t_c = 1$ is a phase effect indicating that the ensemble of particle gyromotions enhances the $\delta\mathbf{E} \times \mathbf{B_0}$ drift current in this time scale.

For the EHs in the ∼16 s wave burst, the electron gyroradius is a few kilometers and the ion gyroradius is ∼100 km; as shown later, the $l_\perp$ of the EHs is roughly 70 km. In addition, the transit times through the EHs are approximately equal to the electron gyroperiod. Therefore, according to Figure 2.6, a net current due to electron $\delta\mathbf{E} \times \mathbf{B_0}$ drift could be established in those EHs.

2.4 Derivation of v_{EH}, $\Delta\Phi$, and $L_\parallel$

2.4.1 Derivation of v_{EH}

The velocity of EHs with respect to the spacecraft (v_{EH}) is the basis for deriving two main characteristics of EHs, potential ($\Delta\Phi$) and parallel size ($L_\parallel$). One common method for deriving v_{EH} is to use time delays from two physically separated EFI antennas. Unfortunately, due to instrument limitations, especially the limited physical length of EFI booms, this time-delay method is only applicable for relatively slow-moving EHs. In the case of the THEMIS EFI, this method can resolve EH velocities up to ∼1000 km/s.

For fast-moving EHs, the Lorentz transformation provides another method for deriving v_{EH}. Substituting the expressions of δE_x and δE_y into the expressions of δB_y and δB_x respectively in the equation set (2.1), one obtains

$$\delta B_x = \frac{\delta B'_x}{\gamma} - v_{EH}\frac{\delta E_y}{c^2}, \tag{2.11}$$

$$\delta B_y = \frac{\delta B'_y}{\gamma} + v_{EH}\frac{\delta E_x}{c^2}. \tag{2.12}$$

As shown later, the electromagnetic EHs in the ∼16 s wave burst were weakly relativistic ($\gamma \approx 1$). Therefore, we have

$$\delta B_x \approx \delta B'_x - v_{EH}\frac{\delta E_y}{c^2}, \tag{2.13}$$

$$\delta B_y \approx \delta B'_y + v_{EH}\frac{\delta E_x}{c^2}. \tag{2.14}$$

According to the model shown in Section 2.2, $\delta B'_x$ and $\delta B'_y$ are induced by the electron $\delta\mathbf{E}\times\mathbf{B_0}$ drift current. As shown in Figure 2.3, the perpendicular components of $\delta\mathbf{B}'$, $\delta B'_x$ and $\delta B'_y$, are typically bipolar along spacecraft trajectories.

v_{EH} is derived by a linear fitting method. In this method, the measured δB_x and δB_y signals are fitted with the following fitting model

$$\delta B_y^{fit} = v\frac{\delta E_x}{c^2}, \tag{2.15}$$

$$\delta B_x^{fit} = -v\frac{\delta E_y}{c^2}. \tag{2.16}$$

where v is an estimate of v_{EH}, and the residue δB_y^{res} ($=\delta B_y - \delta B_y^{fit}$) and δB_x^{res} ($=\delta B_x - \delta B_x^{fit}$) are an estimate of $\delta B'_y$ and $\delta B'_x$, respectively. The resulting v of the two fits are combined by choosing the one with less uncertainty to be the final estimate of v_{EH}.

Figure 2.7 shows an example of the linear fit. As an estimate of $\delta B'_y$ and $\delta B'_x$, respectively, δB_y^{res} and δB_x^{res} exhibit a bipolar feature, which is consistent with the model shown in Section 2.2.

2.4.2 Derivation of $\Delta\Phi$ and $L_\parallel$

The estimation of the potential amplitude ($\Delta\Phi$) and parallel size ($L_\parallel$) of the observed EHs is based on the Gaussian potential model as below:

$$\Phi_{measure} = \Delta\Phi \exp\left[-\frac{(z-z_0)^2}{2(L_\parallel/2)^2}\right] \tag{2.17}$$

With space-dependence converted into time-dependence with $z - z_0 = v_{EH}(t - t_0)$, the corresponding $\delta E_\parallel$ from the potential model is

$$\delta E_\parallel(t) = -\frac{\Delta\Phi}{v_{EH}\delta t/2}\frac{t-t_0}{\delta t/2}\exp\left[-\frac{(t-t_0)^2}{2(\delta t/2)^2}\right] \tag{2.18}$$

where the minus sign in the front of the right-hand side is from the positive-then-negative polarity of $\delta E_\parallel$ in the full set, δt is an estimate of the peak-to-peak interval, and $L_\parallel = v_{EH}\delta t$. To derive $\Delta\Phi$ and $L_\parallel$, the observed $\delta E_\parallel$ is fitted with the following model

$$\delta E_\parallel^{fit}(t) = -p_0\frac{t-p_1}{p_2}\exp\left[-\frac{(t-p_1)^2}{2p_2^2}\right] + p_3 \tag{2.19}$$

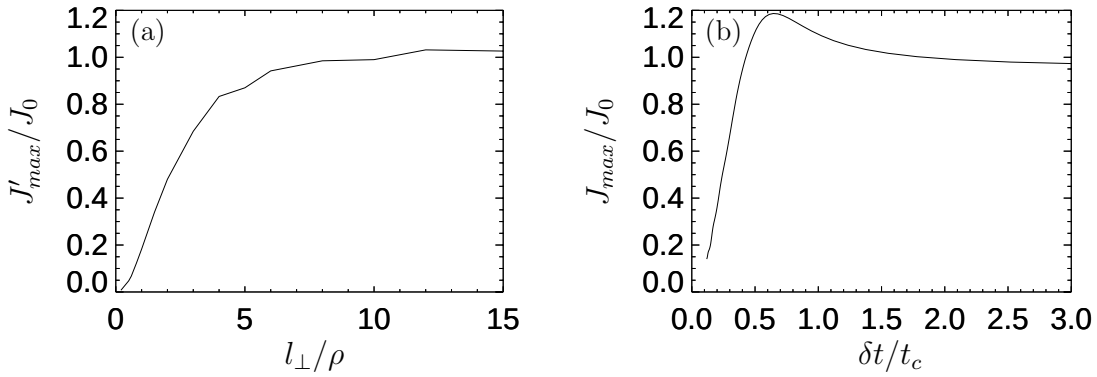

Figure 2.6: The effects of EH perpendicular size and transit time on the formation of the $\delta\mathbf{E} \times \mathbf{B_0}$ drift current from test-particle simulations.

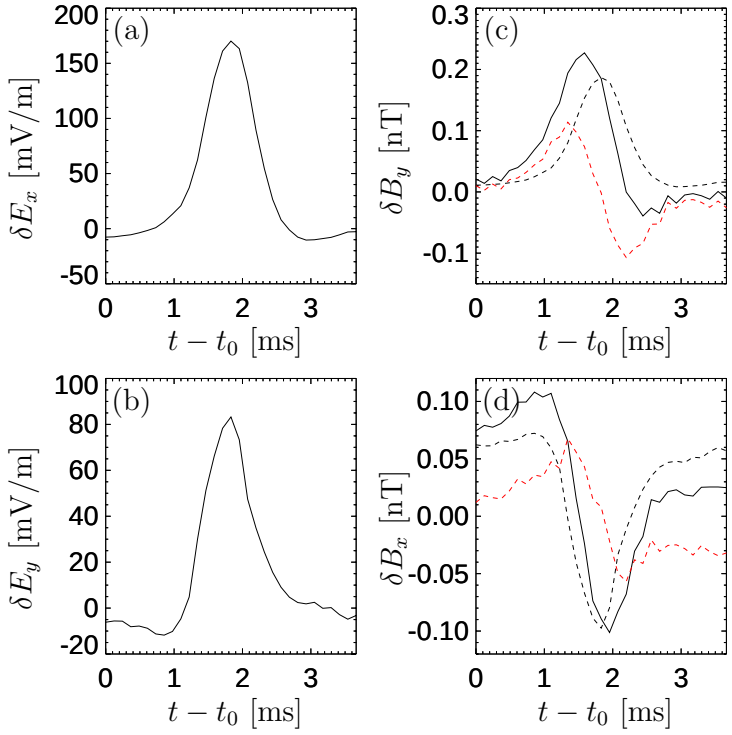

Figure 2.7: An example of the linear fit introduced in Section 2.4. (a) The observed δE_x. (b) The observed δE_y. (c) The observed δB_y (solid line), δB_y^{fit} (black, dashed line), δB_y^{res} (red, dashed line). (d) The observed δB_x (solid line), δB_x^{fit} (black, dashed line), δB_x^{res} (red, dashed line).

Comparing Equations (2.18) and (2.19), we have

$$\Delta\Phi = 2p_0 p_2 v_{EH}, \tag{2.20}$$

$$L_{\parallel} = 2p_2 v_{EH}. \tag{2.21}$$

Figure 2.8 shows an example of fitting $\delta E_{\parallel}$, where the derivative of a Gaussian well fits the $\delta E_{\parallel}$ measurements.

2.5 Statistical Results of v_{EH}, $\Delta\Phi$, and $L_{\parallel}$

This section presents statistical results of the velocities, potentials, and sizes of the electromagnetic EHs in the ∼16 s wave burst using the methods introduced in Section 2.4.

The first step of this work is to select EHs in the ∼16 s wave burst. The following criteria are applied in this step.

(1) The magnitude of each peak of the bipolar $\delta E_{\parallel}$ must be greater than 10 mV/m and $3\sigma_E$, where σ_E is the local standard deviation of $\delta E_{\parallel}$ that is calculated over a 201-data-point window (25 ms).

(2) The peak-to-peak interval of the bipolar $\delta E_{\parallel}$ must be less than 2 ms and greater than the local electron gyroperiod (≈ 0.71 ms).

(3) The polarity of the bipolar $\delta E_{\parallel}$ must be positive-then-negative in time as shown in Figure 2.2(a).

(4) $\Delta E_{\perp}$ must be greater than 50 mV/m, where $\Delta E_{\perp}$ is either $\Delta E_x (\equiv \max[\delta E_x] - \min[\delta E_x])$ or $\Delta E_y (\equiv \max[\delta E_y] - \min[\delta E_y])$, depending on which one produces a better fit.

These selection criteria result in 54 EH samples from the ∼16 s wave burst. Each EH sample consists of 31 data points (4 ms). For the above criteria, the first one makes use of the solitary feature of EHs. The second one is to make sure that only one EH is selected at a time as the peak-to-peak interval of EHs (δt) is generally less than 1 ms in this event,

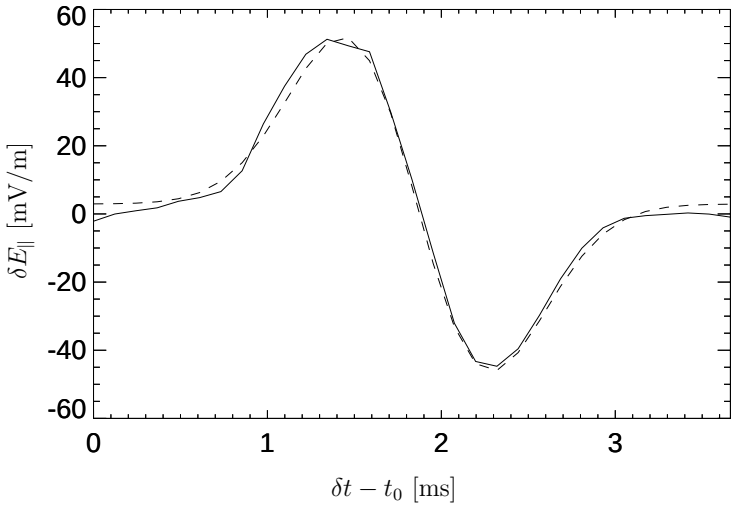

Figure 2.8: An example of fitting $\delta E_\parallel$ with the derivative of a Gaussian, where t_0 is 2008-03-28/11:14:48.1172. The solid line is from spacecraft measurements, and the dashed line is the fit to the measurements.

and that electrons can have sufficient time to establish $\delta\mathbf{E} \times \mathbf{B_0}$ drift current as shown in Figure 2.6. The third one ensures that the selected EHs travel in the same direction and hence are likely from the same source. The fourth one restricts the results with relatively small uncertainties because increasing $\Delta E_\perp$ can improve the goodness of the linear fit model as shown by Equations (2.13) and (2.14).

Figure 2.9 shows the distribution of the derived v_{EH}. The mean v_{EH} is 0.83×10^8 m/s, which verifies that $\gamma \approx 1$ is valid for the EHs in the ∼16 s wave burst.

Figure 2.10 shows the relations of σ_v, uncertainty of v_{EH}, with $\Delta E_\perp$ and $\Delta B_\perp$, respectively, where $\Delta B_\perp$ is either $\Delta B_x (\equiv \max[\delta B_x] - \min[\delta B_x])$ or $\Delta B_y (\equiv \max[\delta B_y] - \min[\delta B_y])$, depending on which one is selected to derive v_{EH}. One can see that the trend of σ_v decreasing as $\Delta E_\perp$ increases is relatively tighter than the decreasing trend of σ_v as $\Delta B_\perp$ increases. This trend difference is consistent with Equations (2.13) and (2.14) because increasing $\Delta E_\perp$ immediately improves the goodness of the linear fit model but increasing $\Delta B_\perp$ does not necessarily have that effect due to the existence of $\delta B'_x$ and $\delta B'_y$.

Figure 2.11 shows the potentials and sizes of the 54 EHs. Because the fourth selection criterion mentioned above confines the perpendicular offset of the spacecraft trajectory through an EH roughly in a region of large $\delta E_\perp$, one can see that $\Delta\Phi$ is approximately centered around 3 kV. $\Delta\Phi$ reaches up to ∼9 kV for a few EHs, suggesting that the central potentials of the EHs are mostly similar but can be very strong in a few EHs. The mean of $\Delta\Phi$ is ∼3.2 kV. The distribution of $L_\parallel$ is more concentrated than that of $\Delta\Phi$. This confirms that the potential of the EHs can be roughly described with a cylindrically symmetric Gaussian, since in that case $L_\parallel$ is roughly independent on the perpendicular offset to the center of an EH but $\Delta\Phi$ is sensitive to that offset. The mean of $L_\parallel$ is ∼68 km. Additionally, the perpendicular sizes of the EHs are generally comparable to parallel sizes because the magnitudes of $\Delta E_\perp$ are generally comparable to those of $\Delta E_\parallel$.

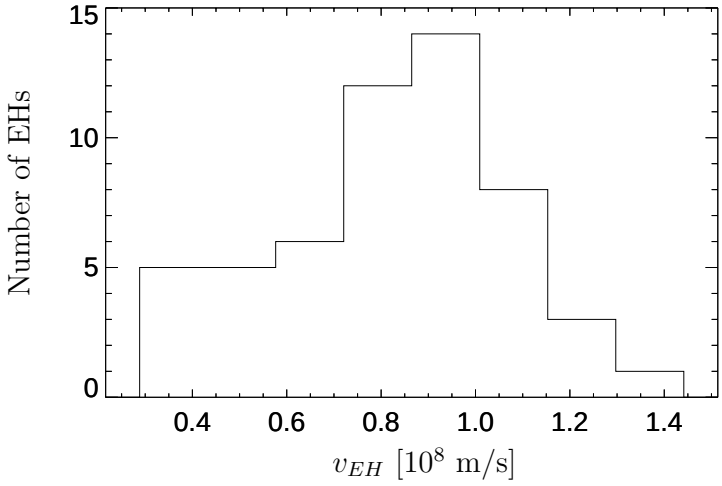

Figure 2.9: Histogram of v_{EH}.

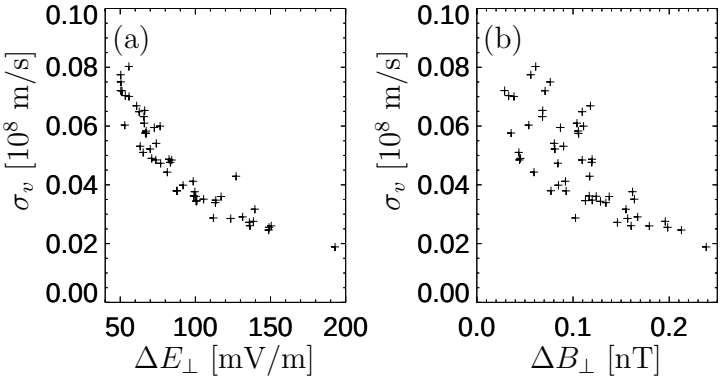

Figure 2.10: (a) σ_v (uncertainty of the derived v_{EH}) versus $\Delta E_\perp$. (b) σ_v versus $\Delta B_\perp$.

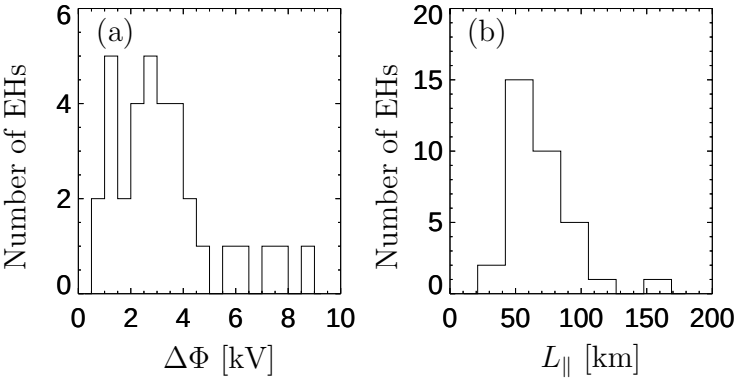

Figure 2.11: Histograms of (a) EH potential $\Delta\Phi$ and (b) parallel size $L_\parallel$.

2.6 Verification of the Interpretations

In the measurements of the electromagnetic EHs, the positive, unipolar $\delta B_{\parallel}$ signals are interpreted as a result of the electron $\delta\mathbf{E} \times \mathbf{B_0}$ drift current in the EHs, and the $\delta B_{\perp}$ signals are interpreted as a superposition of $\delta B_{\perp}{}'$ from the electron $\delta\mathbf{E} \times \mathbf{B_0}$ drift current and the Lorentz transformation of $\delta E_{\perp}$, with the latter mostly predominant. The qualitative aspects of the interpretations have been shown in Section 2.2 by the correlation consistency of $\delta E_{\perp}$ and $\delta B_{\perp}$ signals between the Lorentz transformation and the measurements, and the consistent polarity of $\delta B_{\perp}$ between the model and the measurements.

The interpretations of the observed $\delta B_{\perp}$ and $\delta B_{\parallel}$ signals are different. The former is primarily due to relativistic effects, whereas the latter is due to the $\delta\mathbf{E} \times \mathbf{B_0}$ drift of electrons. The estimation of $\Delta\Phi$ is based on the interpretation of $\delta B_{\perp}$. With the central $\delta B_{\parallel}$ and $\Delta\Phi$ present, Equation (2.8) connects the two interpretations and hence provides a quantitative means to cross-check the interpretations. With these typical values: $\Phi_0 \sim 5$ kV, $n_0 \sim 0.02$ cm^{-3}, $B_0 \sim 50$ nT, and $g \sim 0.50$, one obtains $\sim$0.2 nT for the central $\delta B_{\parallel}$, which corresponds to the upper limit of $\delta B_{\parallel}$ for the measurements. As shown in Figure 2.2, the measured $\delta B_{\parallel}$ is up to $\sim$0.2 nT. Therefore, the interpretations of $\delta B_{\perp}$ and $\delta B_{\parallel}$ signals are consistent with each other.

2.6.1 Detailed EH examples

Three EH examples are presented in this section, one slow, one fast, and one center-crossing (i.e., the trajectory of the spacecraft was close to the center of the EH).

Figure 2.12 shows a relatively slow EH with a velocity of 2.90×10^7 m/s. The estimated potential and $L_{\parallel}$ are $\sim$1.4 kV and $\sim$43 km, respectively. With $n_0 = 0.02$ cm^{-3}, $B_0 = 50$ nT, and $g = 0.5$, the model in Section 2.2 gives $\Delta B_{\parallel} \lesssim 0.055$ nT according to Equation (2.8). The amplitude of the measured $\delta B_{\parallel}$ is difficult to estimate in this case because of its irregular shape. However, if one takes the range of the $\delta B_{\parallel}$, $\Delta B_{\parallel}$ ($\equiv \max[\delta B_{\parallel}] - \min[\delta B_{\parallel}]$),

which is 0.04 nT, as an estimate of the amplitude of $\delta B_{\parallel}$, the observation and the model are roughly in agreement. In the figure, one can see that the δE_x and δE_y signals do not peak at the center of the EH as they would in an ideal cylindrically symmetric case. One possibility is that the transformation of the signals into FAC is not perfect, due to the uncertainty in determining $\mathbf{B_0}$, so that there are contributions left in δE_x and δE_y from the parallel component. Another possibility is that the shape of this EH is irregular so that the sizes of EH in x and y dimensions are different. EHs with irregular shapes are not uncommon in simulations [*Lu et al.*, 2008]. Note that these two possibilities are not exclusive. Both possibilities could contribute to the results shown in Figure 2.12.

Figure 2.13 shows a relatively fast EH with a velocity of 1.07×10^8 m/s. The estimated potential and $L_{\parallel}$ are ∼4.2 kV and ∼87 km respectively. The observed amplitude of $\delta B_{\parallel}$ is ∼0.09 nT as shown in Figure 2.13(d). With the same background parameters and assuming the perpendicular offset of the spacecraft trajectory is roughly $l_{\perp}$, the model in Section 2.2 gives an estimate of $\Delta B_{\parallel}$ ∼0.1 nT, consistent with the observation. One interesting fact in the figure is that δB_y is well fitted by δE_x but δB_x is not by δE_y. This suggests that $\delta B'_x$ is relatively more significant than $\delta B'_y$, which further suggests that the size of EH in y dimension is larger than in x dimension. (This can be understood from Figure 2.3(b). Imagine an extreme case in which the y-dimension size of the EH is infinite, in which $\delta B'_y$ would be zero.) Additionally, the irregularity of the internal structure of the EH can contribute to the results. However, it is difficult to infer such an irregularity based on a single spacecraft crossing.

In addition to the 54 EH samples, a relatively clean center-crossing (small $\Delta E_{\perp}$ and large $\Delta E_{\parallel}$) EH example is found, as shown in Figure 2.14. The estimated potential is ∼4.8 kV, which is higher than the average value shown in Section 2.5 as expected, and the size ∼59 km. The observed amplitude of $\delta B_{\parallel}$ is roughly 0.15 nT, and the model in Section 2.2 gives an estimate of 0.19 nT without a perpendicular offset correction. Considering the uncertainties in the perpendicular offset and the EH shape, the model and the observation

are in a fairly good agreement.

2.7 Discussion and Summary

Compared to previous observations [*Cattell et al.*, 1999; *Franz et al.*, 2005] and most THEMIS observations of EHs in the plasma sheet, the electromagnetic EHs discussed in this chapter featured faster speeds, larger sizes, and stronger potentials. More important, these electromagnetic EHs raise an interesting question: What mechanism is responsible for the generation of the observed electromagnetic EHs? Many simulation works have been published to address the generation mechanisms of EHs based on previous EH observations. However, a thorough study of the generation of the observed electromagnetic EHs has yet to be made. The statistical properties of the electromagnetic EHs in this chapter can provide useful constraints on theoretical and numerical studies of the generation mechanism of the electromagnetic EHs. Knowing the generation mechanism is important because one can infer the properties of the source using information of the electromagnetic EHs. Additionally, since the observed electromagnetic EHs were travelling anti-earthward along the magnetic field lines, which link (earthward) to the ionosphere, the source region of the electromagnetic EHs is not necessarily inside the plasma sheet.

To sum up, THEMIS observations of electromagnetic EHs were presented. Two co-existing mechanisms were proposed to interpret the magnetic field signals associated with the observed EHs. The $\delta B_\perp$ signals were interpreted as primarily due to relativistic effects, whereas $\delta B_\parallel$ signals were due to $\delta\mathbf{E} \times \mathbf{B_0}$ drift of electrons in EHs. The formation of $\delta\mathbf{E} \times \mathbf{B_0}$ drift of electrons in the observed EHs was verified with test-particle simulations. The interpretation of $\delta B_\perp$ signals was used to derive v_{EH}, which in turn was used to derive $\Delta\Phi$ and $L_\parallel$. Statistical results of v_{EH}, $\Delta\Phi$, and $L_\parallel$ of the observed EHs were presented, followed by observational verifications of the proposed interpretations and some EH examples.

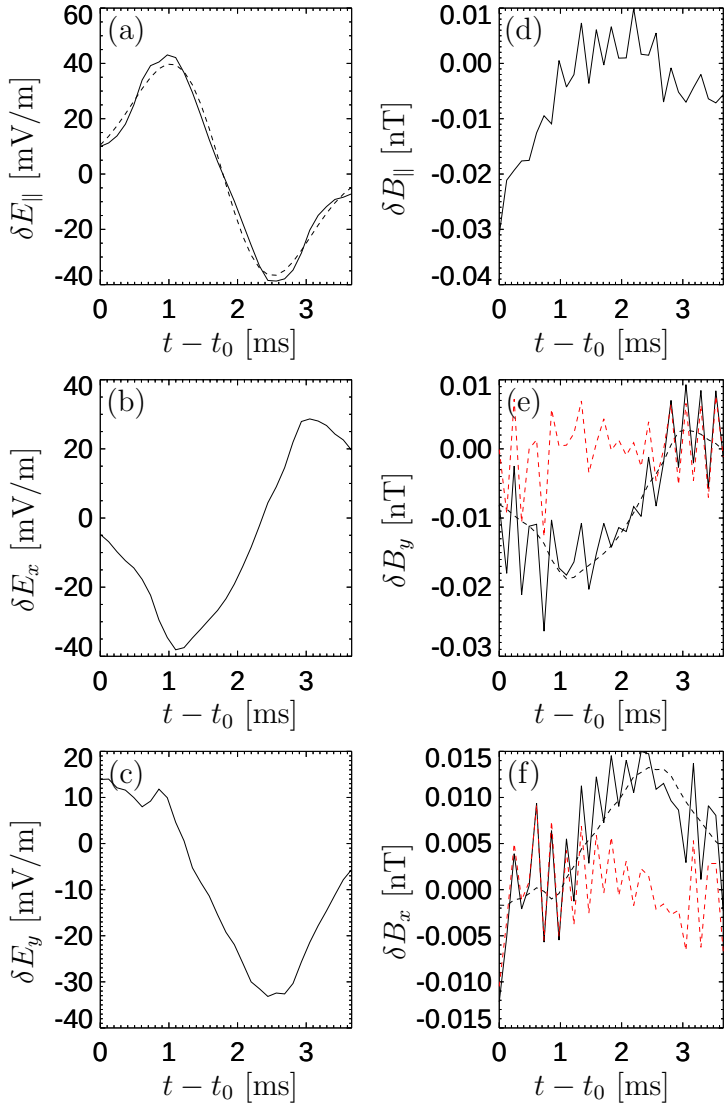

Figure 2.12: An example of a slow EH, where t_0 is 2008-03-28/11:14:54.1617 in the x-axis labels. The dashed line in (a) is a fit of $\delta E_\parallel$ with the derivative of a Gaussian. The format of (e) and (f) is the same as that in Figures 2.7(c) and 2.7(d) respectively. The velocity is 2.90×10^7 m/s from the fit of δB_y, and 2.85×10^7 m/s from the fit of δB_x, with the first one chosen to be the final value because its uncertainty is smaller.

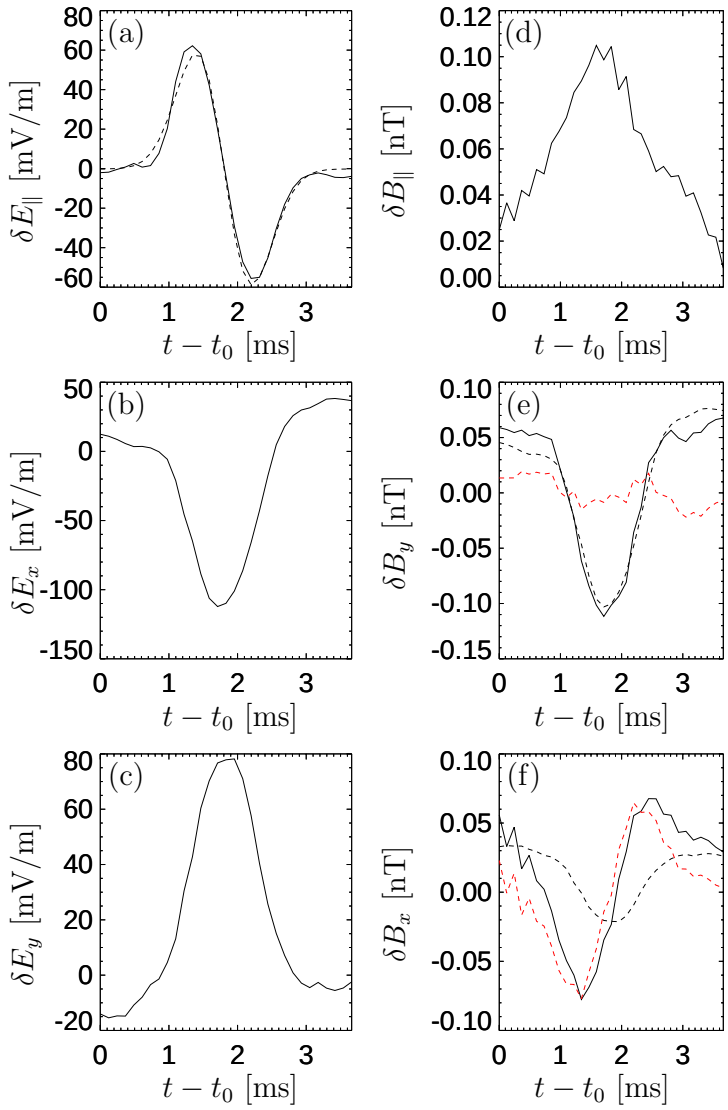

Figure 2.13: An example of a fast EH, where t_0 is 2008-03-28/11:14:48.2664 in the x-axis labels. The format is the same as Figure 2.12. The velocity is 1.07×10^8 m/s from the fit of δB_y, and 0.53×10^8 m/s from the fit of δB_x, with the first one chosen to be the final value because its uncertainty is smaller.

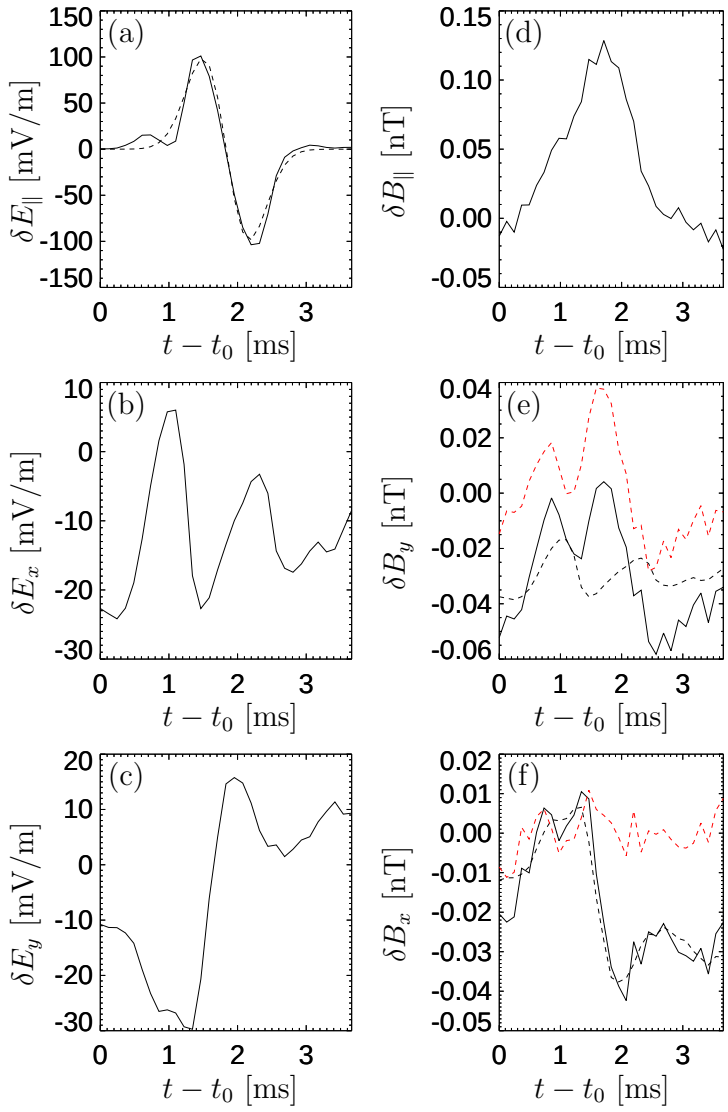

Figure 2.14: An example of central EH crossing, where t_0 is 2008-03-28/11:14:48.4716 in the x-axis labels. The format is the same as Figure 2.12. The final estimated velocity is 8.7×10^7 m/s from δB_x and δE_y.

Chapter 3

ARTEMIS Observations of Kinetic Instabilities in the Lunar Wake

During its first lunar wake flyby on 13 February 2010, ARTEMIS P1 observed electrostatic waves on the outbound side of the flyby. The observed electrostatic waves resulted from kinetic instabilities. The wavelengths and phase velocities of the observed electrostatic waves are derived in this chapter. In addition, 1D Vlasov simulation results are presented to identify the wave mode of the observed electrostatic waves. The properties of the observed electrostatic waves are important to understand kinetic processes in the lunar wake.

3.1 Overview of the Flyby

Figure 3.1 shows the trajectory of ARTEMIS P1 during the flyby, where the Moon was located at $\sim$(63, -9, 2.5)R_E in GSE coordinates.

Figure 3.2 shows overview observations of the flyby. During the flyby, ARTEMIS P1 experienced a crossing of the lunar shadow, an interval indicated by the two vertical black dashed lines in Figure 3.2. For a spinning spacecraft such as ARTEMIS P1, vector field data are collected in a spinning coordinate system and must be de-spun into physical coordinates such as GSE, GSM, SSE, etc., for normal scientific use. However, during the shadow of this flyby, ARTEMIS P1 lost its spin reference, the Sun, and the spin data were no longer valid for de-spinning vector field data. Therefore, a correction had to be made against this shadow effect. A simple method was developed for this correction in this work, and is described in detail in Appendix B. The ion velocity and magnetic field in Figure 3.2 have been corrected

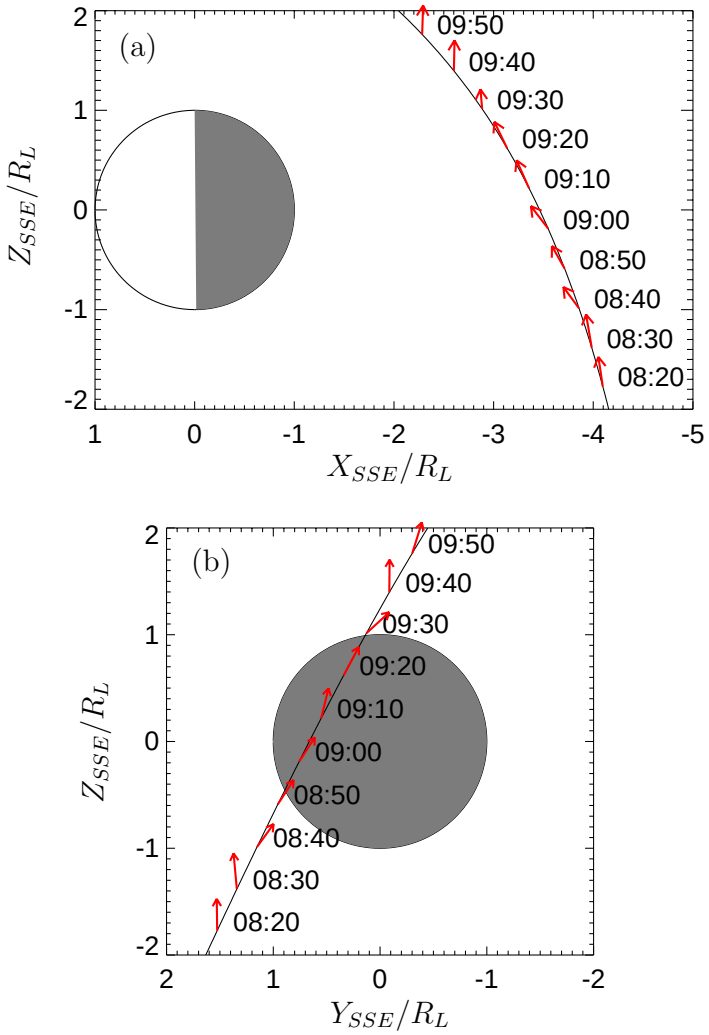

Figure 3.1: The trajectory of ARTEMIS P1 during its first lunar-wake flyby on 13 February 2010 in the (a) x-z plane and (b) y-z plane of the Selenocentric Solar Ecliptic coordinate system (SSE). The coordinates are normalized by the lunar radius ($1R_L \approx 1737$ km). The circles centered at the origins represent the Moon, where the gray areas represent the nightside of the Moon. The red vectors indicate the observed magnetic field at the times (UT) labelled on the right, whose lengths are scaled with respect to the magnitude of the magnetic field (≈ 6 nT) at 08:20 UT. The magnetic field data is from the onboard fluxgate magnetometer (FGM) [*Auster et al.*, 2008].

using that method.

Because the solar wind velocity is not exactly along the Sun-Moon line, the lunar wake does not overlap the lunar shadow precisely, as can be seen from the ion density in Figure 3.2(a). The ion density, along with other particle data (ion velocity, electron temperature, and electron different energy flux), is from the electrostatic analyzer (ESA) [*McFadden et al.*, 2008]. The roughly linear slope of the ion density curve in the log plot of Figure 3.2(a) indicates that the ion density decreases exponentially towards the inside of the wake, which is consistent with previous theoretical work [*Samir et al.*, 1983].

Figure 3.2(c) shows electron temperature (T_e). T_e was approximately isotropic outside the wake. Inside the wake, both the field-aligned temperature and the perpendicular temperature increased, with the former increasing more. This increase is expected in light of the following consideration: Solar wind electrons generally consist of three components: a cold core, a hot halo, and a field-aligned strahl component [*Feldman et al.*, 1975; *Louarn et al.*, 2009]. The wake potential screens out the cold core significantly, as can be seen from the depletion of low-energy flux (the red color) inside the wake in Figure 3.2(e). Therefore, both $T_{e\parallel}$ and $T_{e\perp}$ increase as shown in Figure 3.2(c). The reason why $T_{e\parallel}$ increases more than $T_{e\perp}$ may be due to anisotropy in the high-energy components of solar wind electrons.

The observed magnetic field was mostly stable on the inbound side and had some significant rotations on the outbound side, as shown in Figure 3.2(d).

As indicated by the enhancement of differential energy flux in Figure 3.2(e), parallel electron beams were observed on the outbound side. (The terms "parallel" and "anti-parallel" directions are with respect to the ambient magnetic field ($\mathbf{B}_0$), with the former in the same direction of $\mathbf{B}_0$ and the latter in the opposite direction.) The parallel electron beams were modulated by the orientation of the magnetic field, which is expected since electrons are primarily restricted to move along field lines due to the frozen-in condition.

Figure 3.2(f) shows the electric field power spectrum derived by the onboard digital field board (DFB) [*Cully et al.*, 2008]. There are clear enhancements of electric field power

on the outbound side of the flyby (from ∼09:10 to ∼09:25) that are correlated with the electron beams shown in Figure 3.2(e). The frequency range of the waves is mostly between $0.1f_{pe}$ and $0.4f_{pe}$ except in the middle of the flyby where the power occasionally reaches as low as $\sim 0.01f_{pe}$. These waves were identified as electrostatic waves because no corresponding magnetic field signals were observed from the onboard search coil magnetometer (SCM) [*Roux et al.*, 2008]. The properties of these electric field waves are the focus of this chapter. Three high-resolution wave bursts that are indicated by the black vertical bars across Figures 3.2(e) and 3.2(f) allow us to perform a detailed analysis of these waves. For the ease of reference, these three wave bursts are labelled WB1, WB2, and WB3 in a temporal order.

3.2 Waveform and Spectrum

Figure 3.3 displays the waveforms (sample rate ∼16 kHz; filtered from ∼10 Hz to ∼6 kHz) and spectrograms of parallel electric fields ($E_{\parallel}$) from WB1, WB2, and WB3. The waveforms are from the onboard EFI [*Bonnell et al.*, 2008]. The spectrograms were computed from the corresponding waveforms. $E_{\parallel}$ dominates in the electric field signals of the three wave bursts, indicating that $\mathbf{E} \parallel \mathbf{B_0}$ and that these electrostatic waves had phase velocity along $\mathbf{B_0}$. In general, the $E_{\parallel}$ amplitudes of these waves roughly vary from 5 mV/m to 15 mV/m as shown in Figures 3.3(a), 3.3(c), and 3.3(e). The spectral characteristic of these waves, shown in Figures 3.3(b), 3.3(d), and 3.3(f), is generally consistent with that shown in Figure 3.2(f) but with detailed structures, especially for WB2 and WB3 which consist of enhanced waves from ∼09:18:39 to ∼09:18:42 and from ∼09:20:13 to ∼09:20:16.5, respectively.

3.3 Wavelength and Phase Velocity

The onboard EFI consists of three double-probe booms, with two long, orthogonal booms in the spin plane of the spacecraft, and one relatively short boom along the spin axis [*Bonnell et al.*, 2008]. Because longer booms generally have more accurate measurements [*Pedersen et al.*, 1998], the analysis of this work focuses on measurements from the longest

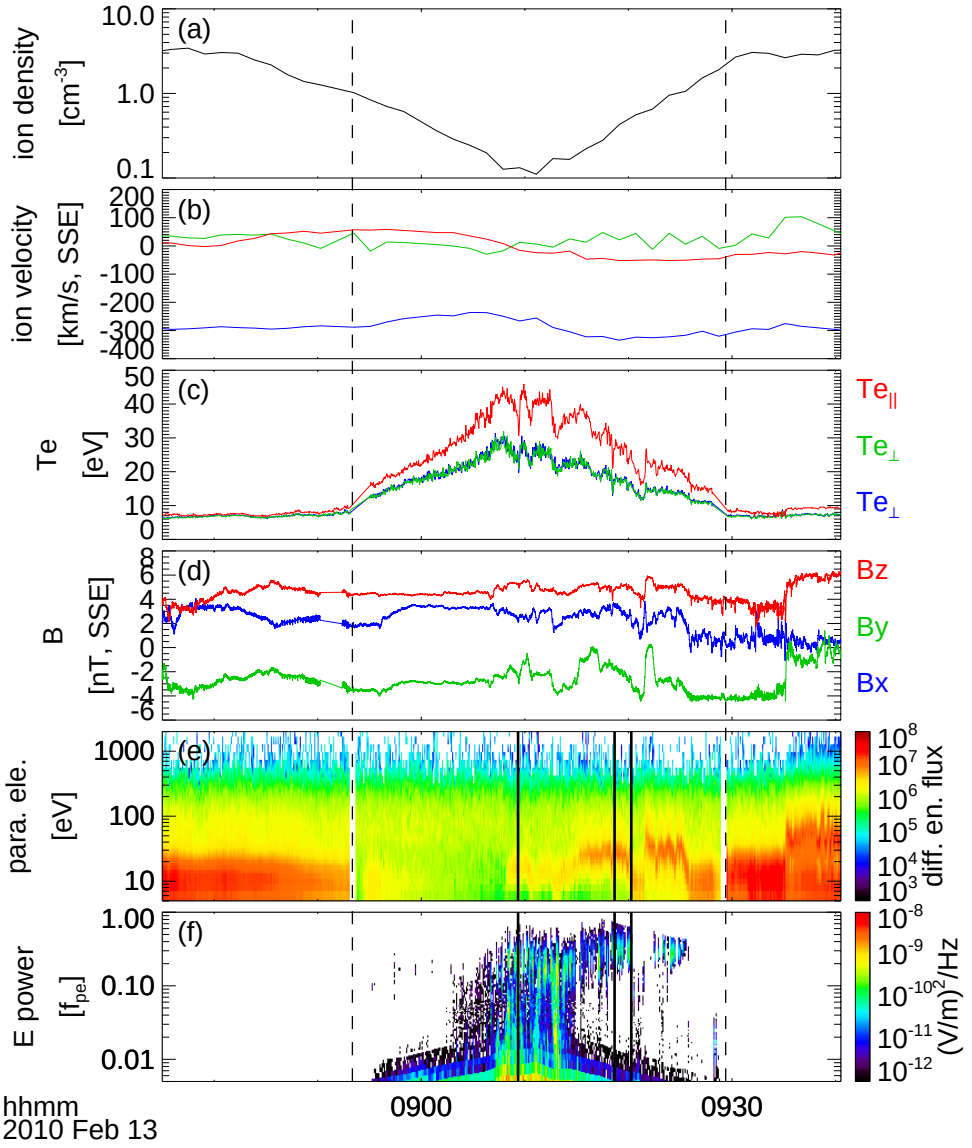

Figure 3.2: Time-series overview observations of the flyby, where the shadow interval of the flyby is between the two vertical black dashed lines across the figure. (a) Ion density. (b) Ion velocity in Selenocentric Solar Ecliptic (SSE) coordinates. (c) Electron temperature, where the red line is field-aligned temperature ($T_{e\|}$) and the green and blue lines are perpendicular temperatures ($T_{e\perp}$). (d) Magnetic field in SSE coordinates. (e) Differential energy flux of parallel electrons. (f) Electric field power spectrum from the onboard digital field board (DFB) [*Cully et al.*, 2008] with frequency normalized by the local electron plasma frequency (f_{pe}), where the three vertical red dashed lines indicate the times of three wave bursts that are analyzed in detail.

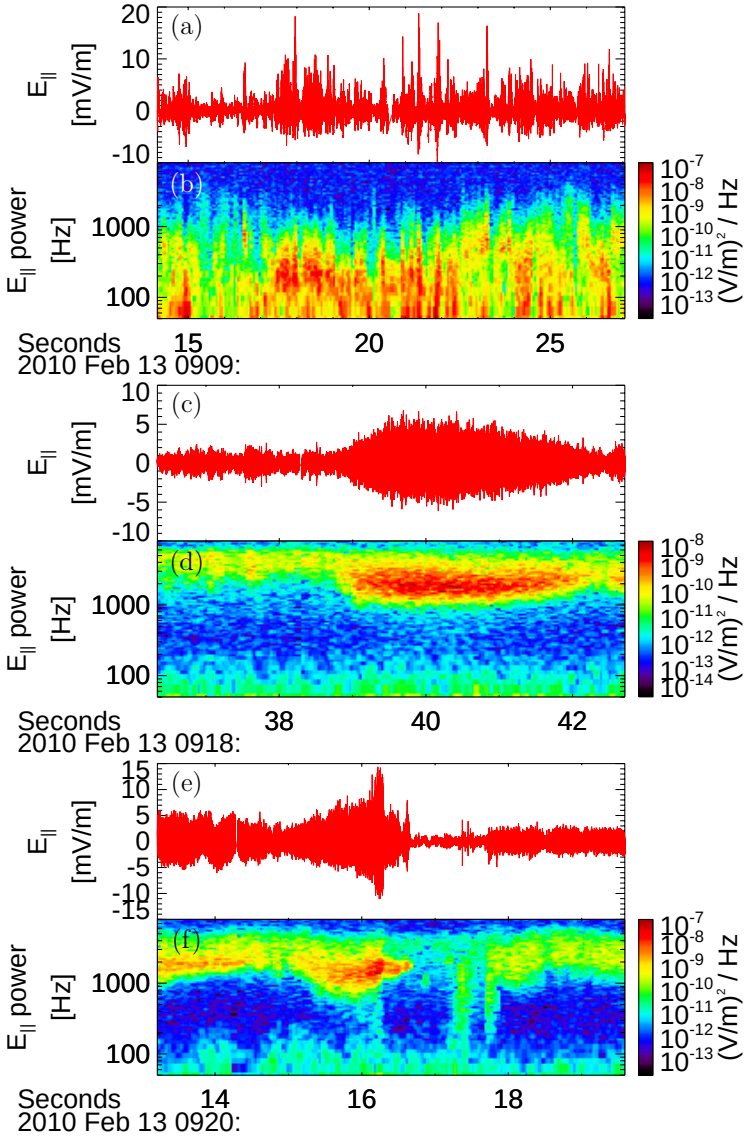

Figure 3.3: Parallel electric field waveforms and spectrograms of WB1 (a, b), WB2 (c, d), and WB3 (e, f).

EFI boom which connects the EFI probes numbered 1 and 2. The results from the second longest boom (not shown) generally confirm those from the longest boom.

Figure 3.4 illustrates plasma waves passing one EFI boom in the spin plane. In general, the phase of a wave mode with frequency ω and wave vector $\mathbf{k}$ is

$$\theta = \mathbf{k} \cdot \mathbf{x} - \omega t, \tag{3.1}$$

where θ is the phase, t time, $\mathbf{x}$ location in 3D space. As shown in Figure 3.4, in the EFI frame, the phase shift between the two opposite probes at time t is

$$\begin{aligned} \Delta\theta(t) = \theta_1(t) - \theta_2(t) &= \mathbf{k} \cdot (\mathbf{x}_1 - \mathbf{x}_2) \\ &= k_{sp} L \cos\phi = k_{sp} L \cos(\omega_s t + \phi_0), \end{aligned} \tag{3.2}$$

where k_{sp} is the component of $\mathbf{k}$ in the spin plane, L the effective distance between the two EFI probes, ω_s the spin rate of the spacecraft, and ϕ_0 the initial phase of the spin. On the other hand, the time delay of waves moving from one EFI probe to the other is

$$\Delta t = \frac{L \cos\phi}{v_{sp}} = \frac{L}{v_{sp}} \cos(\omega_s t + \phi_0) \tag{3.3}$$

where Δt is the time delay, and v_{sp} is the spin-plane component of the phase velocity of the waves. From Equations (3.2) and (3.3), one can see that both $\Delta\theta$ and Δt are a sinusoidal function of time with amplitudes as a function of wavenumber and phase velocity, respectively. Therefore, by fitting the derived $\Delta\theta$ and Δt from observations with a sinusoidal model, one can derive k_{sp} and v_{sp} from the amplitudes of the resultant fits.

$\Delta\theta$ is obtained from cross-spectrum analysis and Δt from cross-correlation analysis. For a monochromatic wave, the two kinds of analysis are interchangeable if the wave frequency is known. However, in real situations, there is a spread in both wavenumber and wave frequency, and hence these two analyses have different uses, with the cross-spectrum analysis ideal for deriving wavenumber and the cross-correlation analysis ideal for deriving phase velocity. In cross-spectrum analysis, the derived phase shift is generally averaged over

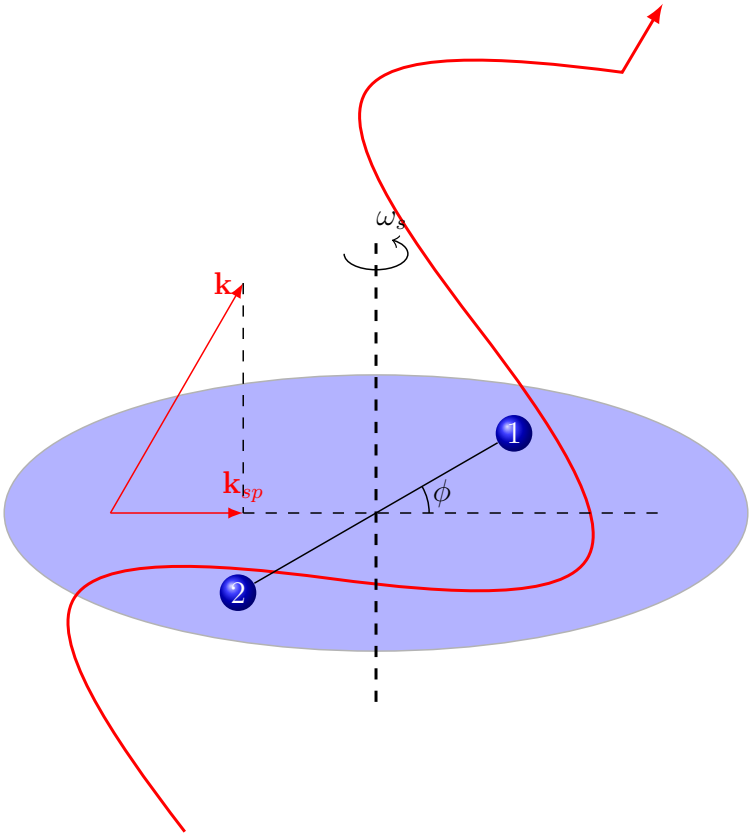

Figure 3.4: An illustration of waves passing an EFI boom. The blue balls, numbered with 1 and 2 respectively, represent the two probes on an EFI boom in the spin plane, the light blue ellipse plane. The spin rate is ω_s. The red, wave-like curve represents a series of waves passing the probes with wave vector $\mathbf{k}$ whose spin-plane component is $\mathbf{k}_{sp}$. The angle between $\mathbf{k}_{sp}$ and the EFI boom is denoted with ϕ.

a number of frequency bins. Therefore, the resultant wavelength is an average over the corresponding frequencies. On the other hand, in cross-correlation analysis, it is assumed that the signals have a uniform velocity over a frequency range of interest in the time scale of Δt.

In addition to $\Delta\theta$, the cross-spectrum analysis gives the coherence between two series of signals. By definition, the coherence varies between 0 and 1. When the coherence is close to 1, it indicates that the two series of signals are coherent and hence favors the reliability of the derived $\Delta\theta$ and Δt.

Figure 3.5 shows the coherence, phase shift, and time delay of WB1 derived from EFI voltage measurements. The voltage data are band-pass filtered from 100 Hz to 700 Hz prior to analysis. The calculation of the coherence and phase shift uses twenty of the most powerful frequency bins. (Each frequency bin has a band width of 8 Hz.) The red lines in Figures 3.5(b) and 3.5(c) are sinusoidal fits to $\Delta\theta$ and Δt, respectively, using data points with coherence greater than 0.85. One can see that the data (the black line) generally follow the fits well when the coherence is close to 1, especially for Δt after 09:09:22, indicating that k_{sp} and v_{sp} from the fits have a relatively high degree of reliability in that period. The fits of $\Delta\theta$ and Δt give $k_{sp} = 0.001912$ m^{-1} and $v_{sp} = 1131$ km/s, respectively, with uncertainties less than 30%. Assuming $\mathbf{k} \parallel \mathbf{B_0}$, these results correspond to a wavelength of 1727 m and a phase velocity of 2151 km/s, respectively.

Figures 3.6 and 3.7 show the results of WB2 and WB3, respectively, in the same format of Figure 3.5. The voltage data are band-pass filtered from 1 kHz to 3 kHz for both bursts. Compared to Figure 3.5, the fits of $\Delta\theta$ and Δt show much better agreement with data when the coherence is close to 1 in both figures. With similar calculations, a wavelength of 272 m and a phase velocity of 1568 km/s are obtained for WB2, and a wavelength of 231 m and a phase velocity of 1397 km/s obtained for WB3.

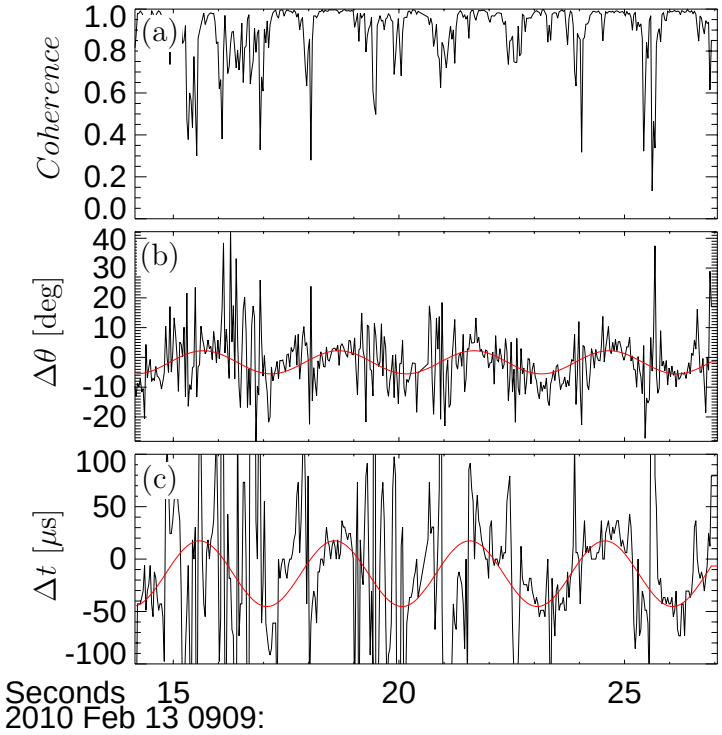

Figure 3.5: Cross-spectrum analysis and cross-correlation analysis results of WB1 using the EFI boom 1-2. (a) Coherence. (b) Phase shift ($\Delta\theta$). The red line is a fit of $\Delta\theta$ according to Equation (3.2). (c) Time delay (Δt). The red line is a fit of Δt according to Equation (3.3).

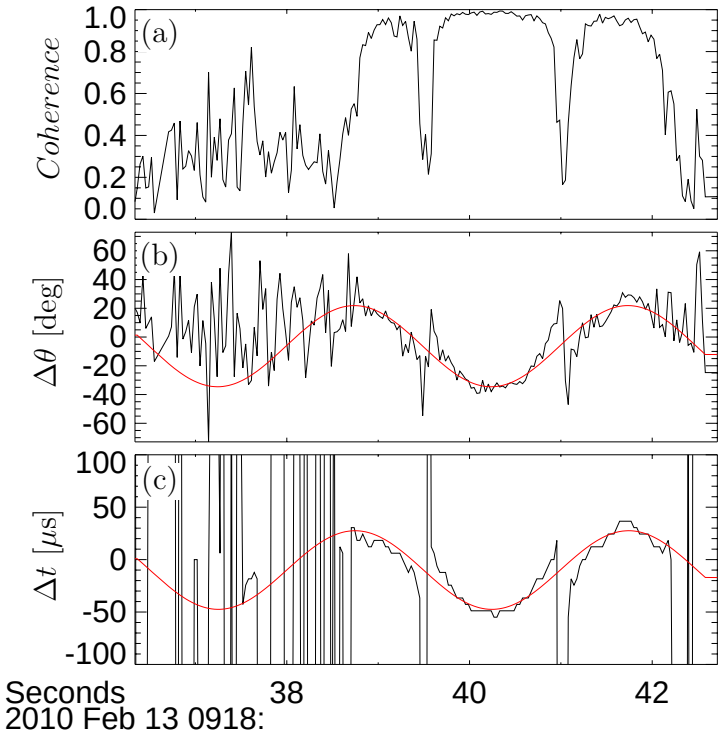

Figure 3.6: Cross-spectrum analysis and cross-correlation analysis results of WB2 using the EFI boom 1-2. The format is the same as Figure 3.5.

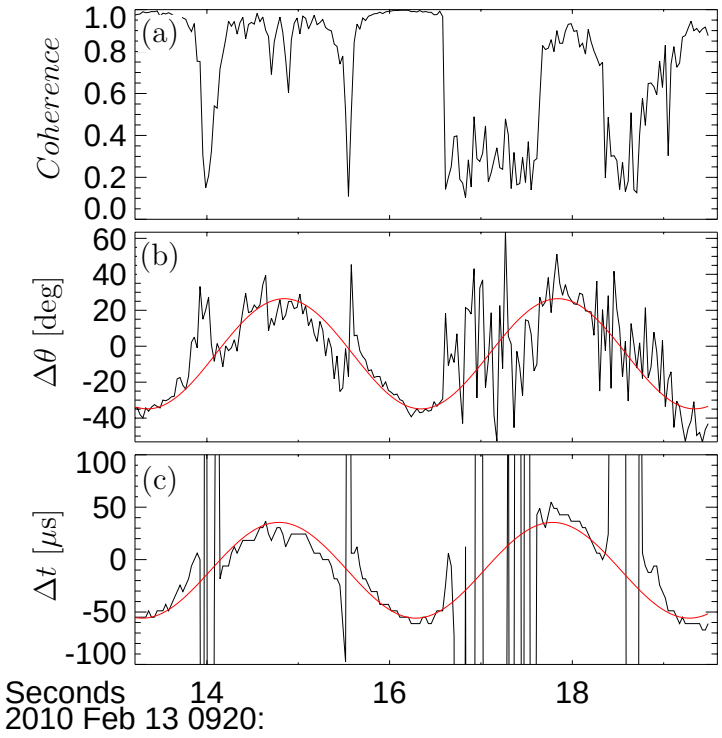

Figure 3.7: Cross-spectrum analysis and cross-correlation analysis results of WB3 using the EFI boom 1-2. The format is the same as Figure 3.5.

3.4 Wave Mode

As shown in Figure 3.2(f), the power enhancement in the electrostatic waves on the outbound side of the flyby generally lies between $0.1f_{pe}$ and $0.4f_{pe}$. In this frequency range, the electron beam mode [*Gary*, 1985] and the electron acoustic mode [*Gary and Tokar*, 1985] are two possible candidates for driving wave growth. However, the latter requires a substantial hot electron component, the presence of which is not supported by observations. Thus, the observed electrostatic waves are likely to be the electron beam mode. To confirm this hypothesis, 1D electrostatic Vlasov simulations are carried out with the initial conditions close to observations so as to make relevant comparisons between simulations and observations. As shown later, the observed waves have different wavelengths in units of the local Debye length, namely, different values of $k\lambda_D$ in WB1, WB2, and WB3. To cover the observed range of $k\lambda_D$, two representative runs are presented with different values of $k\lambda_D$ for the fastest growing mode.

The Vlasov code used in this work is based on the time-splitting scheme of *Cheng and Knorr* [1976] with open boundary conditions. More details regarding the code can be found in *Newman et al.* [2008]. Ions are initialized as homogeneous, Maxwellian background with proton mass. Electrons are initialized with two components, one background component and one beam-like component. The initial electron velocity distribution function takes the form:

$$\begin{aligned} f_e(v) = & \frac{n_1\Gamma[\kappa]}{\sqrt{\pi(2\kappa-3)v_{t1}^2}\Gamma[\kappa-1/2]}\left(1+\frac{v^2}{(2\kappa-3)v_{t1}^2}\right)^{-\kappa} \\ & +\frac{n_b\Gamma[\kappa]}{\sqrt{\pi(2\kappa-3)v_{tb}^2}\Gamma[\kappa-1/2]}\left(1+\frac{(v-u_b)^2}{(2\kappa-3)v_{tb}^2}\right)^{-\kappa}, \end{aligned} \tag{3.4}$$

where the one-dimensional kappa distribution [*Summers and Thorne*, 1991] is used with $\kappa = 6$, Γ is the gamma function, n_1 and v_{t1} are the number density and thermal velocity of the major background component, respectively, and n_b, v_{tb}, and u_b are the number density, thermal velocity, and drifting velocity of the minor beam-like component, respectively.

Table 3.1 lists parameters of initial electron distribution of the two runs. As shown

Table 3.1: Parameters of initial electron distribution

	Run 1	Run 2
n_1	1.01	1.015
v_{t1}	1	1
n_b	-0.01	-0.015
v_{tb}	0.05	0.1
u_b	0.4	0.4

in Figures 3.2(c) and 3.2(e), the energy level of the enhanced parallel electron differential energy flux is approximately equal to the background electron temperature. However, because differential energy flux is proportional to $E^2 f$, where E and f represent energy and distribution function, respectively, the energy level of the beam is not equal to but a fraction of that of the enhanced differential energy flux. (At beam energy level (E_b), $\frac{\partial f}{\partial E}|_{E_b} = 0$; thus, $\frac{\partial (E^2 f)}{\partial E}\Big|_{E_b} = E_b^2 \frac{\partial f}{\partial E}\big|_{E_b} + 2E_b f(E_b) = 2E_b f(E_b) > 0$, indicating E_b is lower than the energy level of the peak differential energy flux where $\frac{\partial (E^2 f)}{\partial E} = 0$.) Thus, u_b is chosen to be a fraction of the thermal velocity of the background electrons for both runs, as shown in Table 3.1. For such a low drifting velocity, it is relatively easier to carve the distribution function than to add a bump to create a positive slope. Therefore, negative n_b is used. Due to the negative n_b and small v_{tb}, the initial beam velocity that corresponds to a positive peak in the distribution function is slightly larger than u_b. Figure 3.8 shows the profiles of initial electron distributions of Run 1 and Run 2.

The phase-space domain is distributed on a $N_z \times N_{ve}(N_{vi}) = 4096 \times 2048(256)$ grid that spans the region $0 \leq z \leq L_z = 4096\lambda_D$ and $-12v_{t1}(-10v_{ti}) \leq v \leq 12v_{t1}(10v_{ti})$, where $\lambda_D = \frac{\epsilon_0 m_e v_{t1}^2}{n_0 e^2}$, $n_0 = n_1 + n_2$, and $v_{t1}(v_{ti})$ is the thermal velocity of the background electrons (ions). The size of the simulation domain and the homogeneous initial density is sufficient to model the *local* wave dynamics considered here. A larger *global* simulation study that includes spatial inhomogeneity will be the subject of future investigation.

Figure 3.9 shows linear-analysis results of the initial electron distribution of Run 1. (Appendix C describes the details of the linear-analysis calculation.) In Figure 3.9(a), the

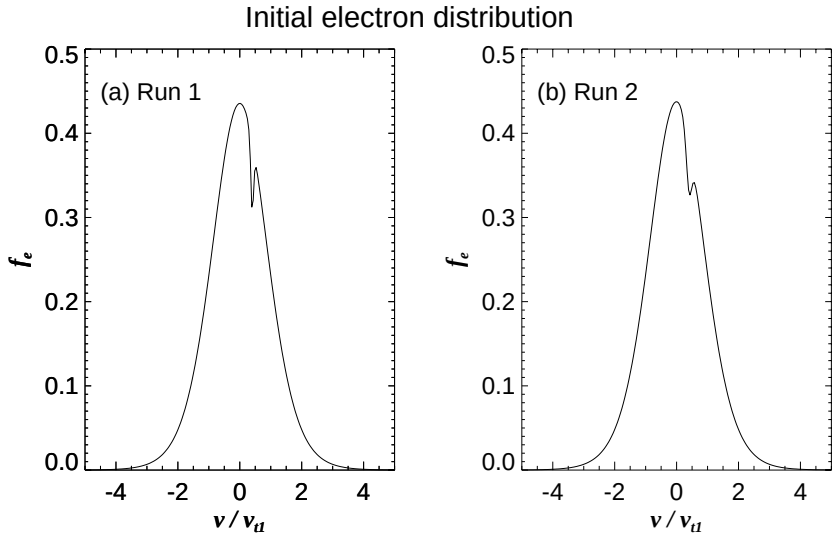

Figure 3.8: Initial electron distribution of Run 1 and Run 2.

Nyquist curve crosses the negative real axis (the blue line) once, indicating that there is one unstable mode in the system [*Penrose*, 1960]. (The Nyquist curve starts and ends at the origin, which must be excluded when counting crossings of the negative real axis.) Figure 3.9(b) shows the dispersion relation of the unstable mode. The linear feature of the ω_r-k relation (the black line) is consistent with the electron beam mode, as shown in previous studies [*Gary*, 1985; *Onsager and Holzworth*, 1990]. The γ-k relation (the red line) shows that the fastest growing mode has $k\lambda_D \approx 0.8$, with the growing modes extending to $k\lambda_D \approx 2$.

Figure 3.10 shows linear-analysis results of the initial electron distribution of Run 2. The results are generally similar to those of Run 1 except that the fastest growing mode has $k\lambda_D \approx 0.45$ in Run 2. A linear analysis for a set of initial parameters has been performed in this work, and it shows that the $k\lambda_D$ of the fastest growing mode is most sensitive to v_{tb}, which is somewhat expected since v_{tb} affects the positive slope in the initial distribution most. The general trend is that the smaller the v_{tb}, or the steeper the positive slope in the initial distribution, the larger the $k\lambda_D$ of the fastest growing mode. For the three wave bursts WB1, WB2, and WB3, the local values of λ_D are roughly 108 m, 53 m, and 46 m, respectively, and the corresponding values of $k\lambda_D$ are roughly 0.4, 1.23, and 1.24, respectively, with the wavelengths derived in Section 3.3. All the observed $k\lambda_D$ are accessible for electron beam mode based on the linear analysis results.

Figure 3.11 shows spectral results of Run 1. As shown in Figure 3.11(a), the frequency of the waves is around $0.2f_{pe}$, consistent with the higher-frequency part of the spectrum in Figure 3.2(f). The frequency-wavenumber spectrum in Figure 3.11(b) matches the linear-analysis result of electron beam mode quite well, supporting that the observed frequency-time spectrum in Figure 3.2(f) is likely on the electron beam mode branch. Figure 3.12 shows spectral results of Run 2, which generally supports the same conclusion from Figure 3.11.

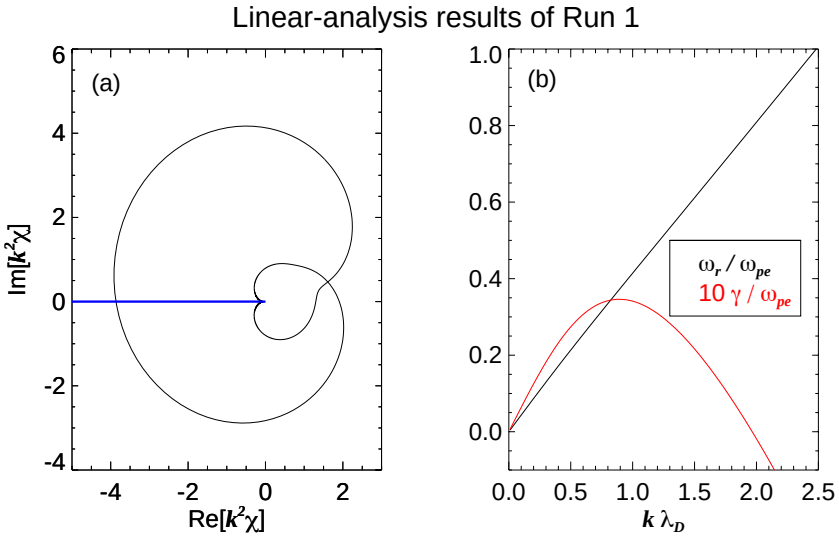

Figure 3.9: Linear-analysis results of the initial electron distribution of Run 1. (a) Nyquist diagram, where k is wavenumber, χ is the regular susceptibility in an electrostatic, kinetic model, and the blue line represents the negative real axis. (b) The dispersion relation of electron beam mode, where ω_r and γ are the real and the imaginary parts of the complex wave frequency respectively, and $\omega_{pe} = \left(\frac{n_0 e^2}{\epsilon_0 m_e}\right)^{1/2}$. The growth curve γ-k (the red line) is scaled by a factor of 10 for easy recognition.

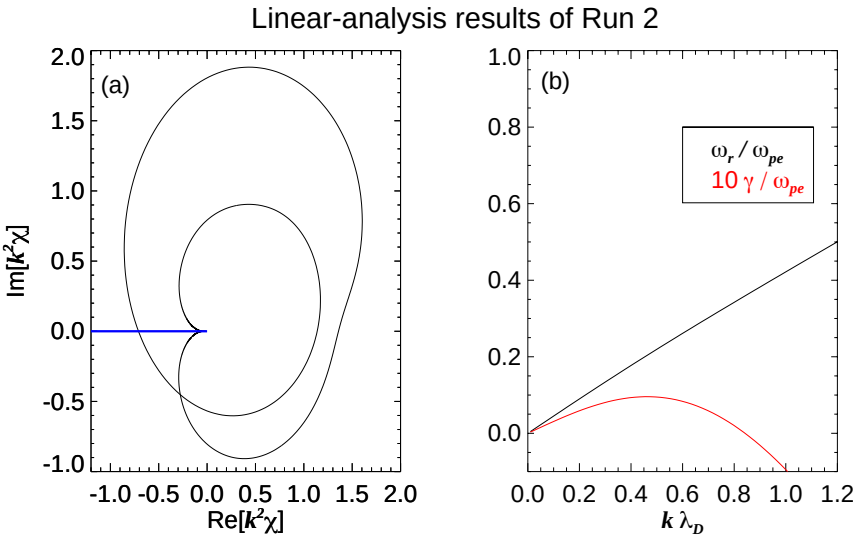

Figure 3.10: Linear-analysis results of the initial electron distribution of Run 2. The format is the same as Figure 3.9.

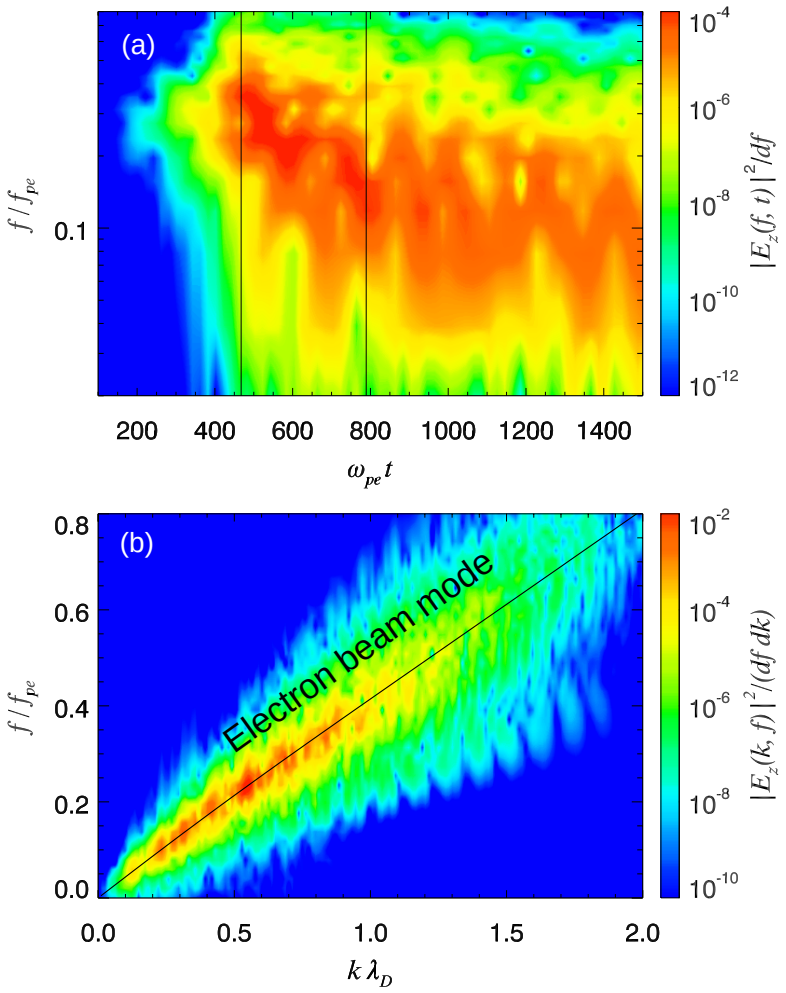

Figure 3.11: Spectral results of Run 1. (a) Spectrogram of E_z at the center of the simulation box ($z/L_z = 0.5$), where $f_{pe} = \omega_{pe}/2\pi$. (b) Frequency-wavenumber spectrum calculated from the period between the two vertical lines in panel (a), where the oblique black line is from the linear analysis of the initial electron distribution. The frequency range in (a) is in a log scale for a close comparison with observations, whereas the frequency range in (b) is in a linear scale to preserve the linear feature of the frequency-wavenumber relation of the electron beam mode.

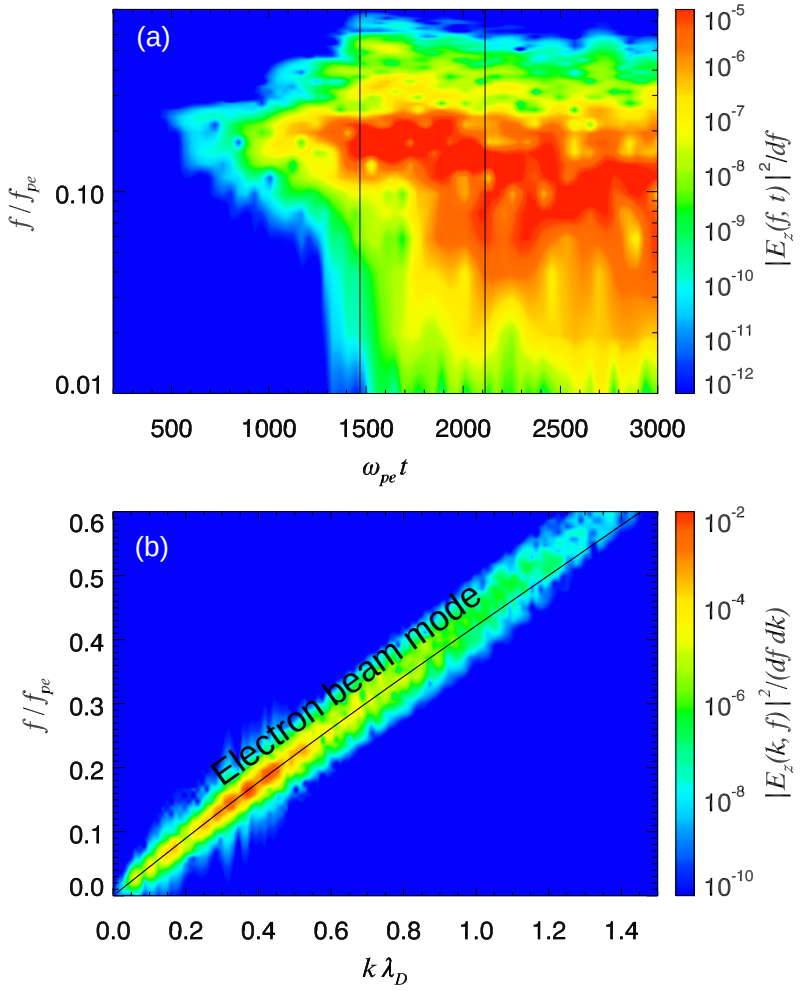

Figure 3.12: Spectral results of Run 2. The format is the same as Figure 3.11.

3.5 Discussion and Summary

Knowing the mode of the electrostatic waves observed on the outbound side of the flyby helps us to have a better understanding of the big picture of the lunar wake dynamics. As proposed in previous works [*Farrell et al.*, 1996; *Nakagawa et al.*, 2003; *Halekas et al.*, 2011], there is an electron velocity filtration at work in the lunar wake: As solar wind electrons refill the lunar wake along the solar wind field lines, the field-aligned velocity distribution of the electrons is filtered by the wake potential such that low energy electrons are reflected by the negative wake potential whereas high energy electrons penetrate the negative wake potential and reach the other side of the wake. The field-aligned distribution of solar wind electrons is asymmetric due to the presence of the solar wind strahl component, a high-energy field-aligned electron population coming from the Sun [*Fitzenreiter et al.*, 1998; *Louarn et al.*, 2009]. This feature leads to an asymmetric wake potential as suggested by *Halekas et al.* [2011]. One consequence from the asymmetric field-aligned distribution of solar wind electrons and wake potential is that the filtered overall electron distribution is not necessarily stable, i.e., a positive slope can be formed in the electron distribution, when the distribution of penetrating electrons attaches to that of reflecting electrons on the other side of the wake. However, the positive slope of the unstable distribution is expected to occur within the bulk of the distribution, for which the electron beam mode is expected to prevail [*Gary*, 1985; *Onsager et al.*, 1989]. As shown in this chapter, the observed electrostatic waves were likely on the electron beam mode branch, hence providing confirmative evidence for the existence of the electron velocity filtration in the lunar wake.

The amplitudes of electric field waveforms in WB1 are clearly more modulated than those in WB2 and WB3 as shown in Figure 3.3, suggesting that other wave modes may be involved in WB1. As shown in Figure 3.2(f), the wave frequency spectrum at the time of WB1 has a low-frequency component that can reach as low as $0.01 f_{pe}$, a value that is below the frequency range of the electron beam mode. The location of WB1 coincided with the

minimum density shown in Figure 3.2(a), indicating that the spacecraft was relatively deep inside the wake at the time. Similar to *Ogilvie et al.* [1996], *Halekas et al.* [2011] reported counter-streaming ions in the wake. Because $0.01 f_{pe}$ is on the order of ion plasma frequency, ion dynamics may be involved in WB1. In addition, WB1 spans a broader frequency band than WB2 and WB3. Previous studies show that both solitary structure (e.g., electron phase-space holes, [*Kojima et al.*, 1997]) and non-solitary structures (e.g., chorus emissions [*Santolík et al.*, 2003]) can produce a broadband spectrum. In this work, no well-defined solitary structures are present in WB1 or in the simulations.

Since the waves in WB1 likely consist of wave modes other than just the electron beam mode, it is difficult to make pertinent comparisons of the amplitudes of the waveforms between simulations and observations for WB1. However, the wave energy of WB2 and WB3 is mostly within the frequency range of the electron beam mode, and thus a waveform amplitude comparison between simulations and observations would be appropriate for these two bursts. Since Run 1 has $k\lambda_D \sim 1.0$, a value closer to those in WB2 ($k\lambda_D \approx 1.23$) and WB3 ($k\lambda_D \approx 1.24$) than Run 2's result ($k\lambda_D \sim 0.4$), it is appropriate to use Run 1 to make such a comparison. In the simulation, the electric field is normalized by $e\lambda_D n_0/\epsilon_0$, i.e., $E = (e\lambda_D n_0/\epsilon_0)\tilde{E}$, where E is the electric field in physical units, and $\tilde{E}$ is the normalized electric field in the simulation. For WB2 and WB3, $\lambda_D \sim 50$ m, $n_0 \sim 0.5$ cm^{-3}; the amplitude of the normalized E_z in Run 1 is roughly 0.005. Therefore, given parameters of WB2 and WB3, the simulation gives an electric field amplitude of roughly 2 mV/m. Considering the uncertainties in modeling the unstable distribution function, the simulation result for the electric field amplitude is in a fairly good agreement with the observations as shown in Figures 3.3(c) and 3.3(e).

Kinetic instabilities have been observed in previous simulations of the lunar wake. *Farrell et al.* [1998] showed electrostatic instabilities in the wake with 1D PIC simulations, although they did not further address the nature of the electrostatic instabilities. *Birch and Chapman* [2001, 2002] observed nonlinear electrostatic waves, namely, electron phase-space

holes [*Roberts and Berk*, 1967; *Singh et al.*, 2011], in 1D and 2D PIC simulations of the wake.

In addition to simulation work, *Bale* [1997] studied the effects of the absorption of solar wind plasmas by the lunar surface and proposed that the positive slope of the affected electron distribution might be responsible for the Langmuir waves observed by Wind during a period when the spacecraft was magnetically connected to the lunar wake [*Bale et al.*, 1997]. However, for this flyby, *Halekas et al.* [2011] suggested that the observed electrostatic waves may be due to the filtration of the electron distribution by the wake potential.

In summary, the characteristics of the observed electrostatic waves are shown in this chapter, in particular, the wavelength and phase velocity measurements from cross-spectrum analysis and cross-correlation analysis of EFI data. The estimated wavelengths vary from a few hundred meters to a couple of thousand meters, whereas the estimated phase velocities are on the order of 1000 km/s. Finally, a 1D Vlasov code is used to identify the mode of those electrostatic waves and the results suggest that those waves were likely on the electron beam mode branch.

Chapter 4

Turbulent Electric and Magnetic Fields in the Earth's Magnetotail

Launched in 2007, the THEMIS mission has accumulated a large data set of electric and magnetic fields in the Earth's magnetotail, which offers an excellent opportunity to study the statistical properties of the turbulent electric and magnetic fields in the magnetotail.

4.1 Data Description

This study uses data from all the five THEMIS spacecraft in the period from 15 December 2007 to 30 April 2011 for the inner spacecraft (THA, THD, and THE) and from 15 December 2007 to 31 December 2009 for the outer spacecraft (THC and THB). (THC and THB were re-directed to the Moon in the end of 2009 and formed the ARTEMIS mission. See Appendix A.) The basic measurements of the study are high time-resolution electric and magnetic field waveforms sampled at 128 Hz. The electric field waveforms are measured by the THEMIS EFI [*Bonnell et al.*, 2008], whereas the magnetic field waveforms are measured by the THEMIS FGM [*Auster et al.*, 2008] for DC signals and by the THEMIS SGM [*Roux et al.*, 2008] for AC signals.The waveforms are recorded in a so-called particle-burst mode of the mission. A particle burst is a continuously sampled data segment with high temporal resolution. The duration of a particle burst ranges mostly from $\sim$10 minutes to a few tens of minutes.

The following criteria are used to select particle bursts for the study:

- The measurements should be made in the tail region. The tail region is defined

as such that the magnetic local time (MLT) is between 20:00 and 04:00, and the distance from the Earth is greater than 8 R_E. An illustration of the tail region in the GSM x-y plane is shown in Figure 4.1.

- The durations of the selected particle bursts should be longer than 128 s.
- The maximum magnitude of the electric fields in a single selected particle burst should be larger than 50 mV/m.

1390 particle bursts in total are obtained for the study.

Each burst is divided into 128-second-long segments before further processing. Incomplete data segments (shorter than 128 seconds) from this division are not used. For each 128-second-long segment, the background electric and magnetic fields, $\mathbf{E}_0$ and $\mathbf{B}_0$, are determined from the medians of the EFI measurements and the FGM measurements, respectively. Electric field perturbation, $\delta\mathbf{E}$, is obtained by subtracting $\mathbf{E}_0$ from the measurements. For the FGM measurements, magnetic field perturbation, $\delta\mathbf{B}$, is obtained by subtracting $\mathbf{B}_0$ from the measurements. For the SCM measurements, $\delta\mathbf{B}$ is from the direct measurements since SCM measurements are already AC signals. The 128-second-long segments are the basis for calculating detrended Poynting flux and power spectral densities of the fields that will be shown later.

4.2 Overview of the Data

Figure 4.2 shows an overview of the 1390 particle bursts obtained for the study. The majority of the bursts are from the inner THEMIS spacecraft, as can be seen from Figures 4.2(a), 4.2(b), and Figure 4.2(c). One main reason for this feature is that the magnitude of electric fields generally decreases as the distance from the Earth increases, which can be seen from Figure 4.2(d); for this reason, the electric field magnitude constraint, i.e., the last burst selection criterion as shown above, limits bursts from the outer spacecraft. Due to the

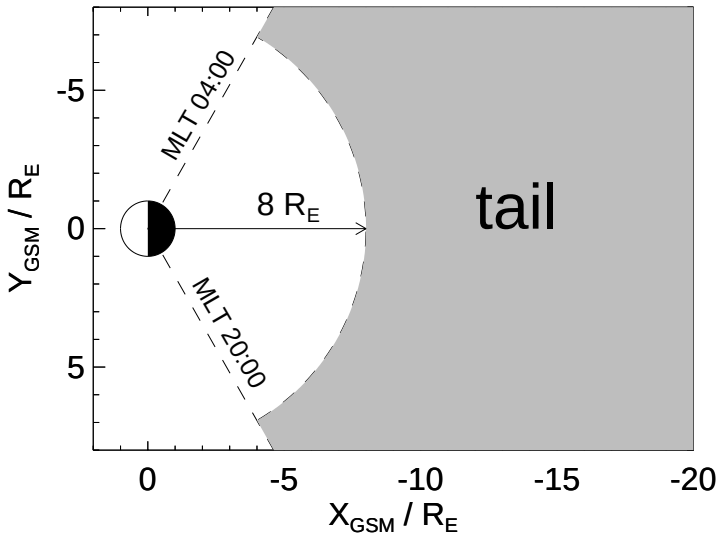

Figure 4.1: Illustration of the definition of the tail region (the gray area).

orbit limits of the THEMIS spacecraft (see Appendix A), the upper limit of the distance to the Earth for the data set is $\sim$30 R_E.

Figure 4.3 shows an example time series of turbulent electric and magnetic fields in the magnetotail with particle-burst data. The electron differential energy flux in the top panel of the figure indicates that the data were recorded in the plasma sheet, which is typically the case for particle bursts in the magnetotail. The rest of the panels of the figure indicate that these electric and magnetic fields are highly intermittent, with strong field fluctuations distributed sporadically over time. This is typically the case for the obtained particle bursts, and is consistent with previous studies [*Weygand et al.*, 2005].

4.3 Detrended Poynting Flux

Kelley et al. [1991] showed that only the detrended Poynting flux, which is given by

$$\mathbf{S} = \frac{\delta\mathbf{E} \times \delta\mathbf{B}}{\mu_0}, \tag{4.1}$$

contains useful information regarding electromagnetic energy flow or dissipation in the Earth's magnetosphere. (For calculating $\mathbf{S}$, $\delta\mathbf{E}$ is determined from EFI data, and $\delta\mathbf{B}$ is from FGM data, as described in the end of Section 4.1.) In particular, the component of the detrended Poynting flux along the background magnetic field ($\mathbf{B}_0$), $S_\parallel$, is responsible for transporting electromagnetic energy between the ionosphere and the plasma sheet. One interesting question that the study can ask is whether there is a statistically significant trend in $S_\parallel$ from the turbulent electric and magnetic fields in the plasma sheet.

Figure 4.4 shows histograms of $S_\parallel$ for various distance ranges. Panels (a)–(c) of the figure show that the distribution of $S_\parallel$ is statistically asymmetric in the near-Earth plasma sheet ($r \lesssim 15\ R_E$) in the sense that large values of $S_\parallel$ (greater than $\sim$0.5 mW/m^2) are much more likely in the earthward direction than the opposite direction, compared to the panel (d). Large values of $S_\parallel$ are generally bursty in time, due to the fact that large values of $S_\parallel$ require large-amplitude electric fields, which are generally bursty in time. In the plasma

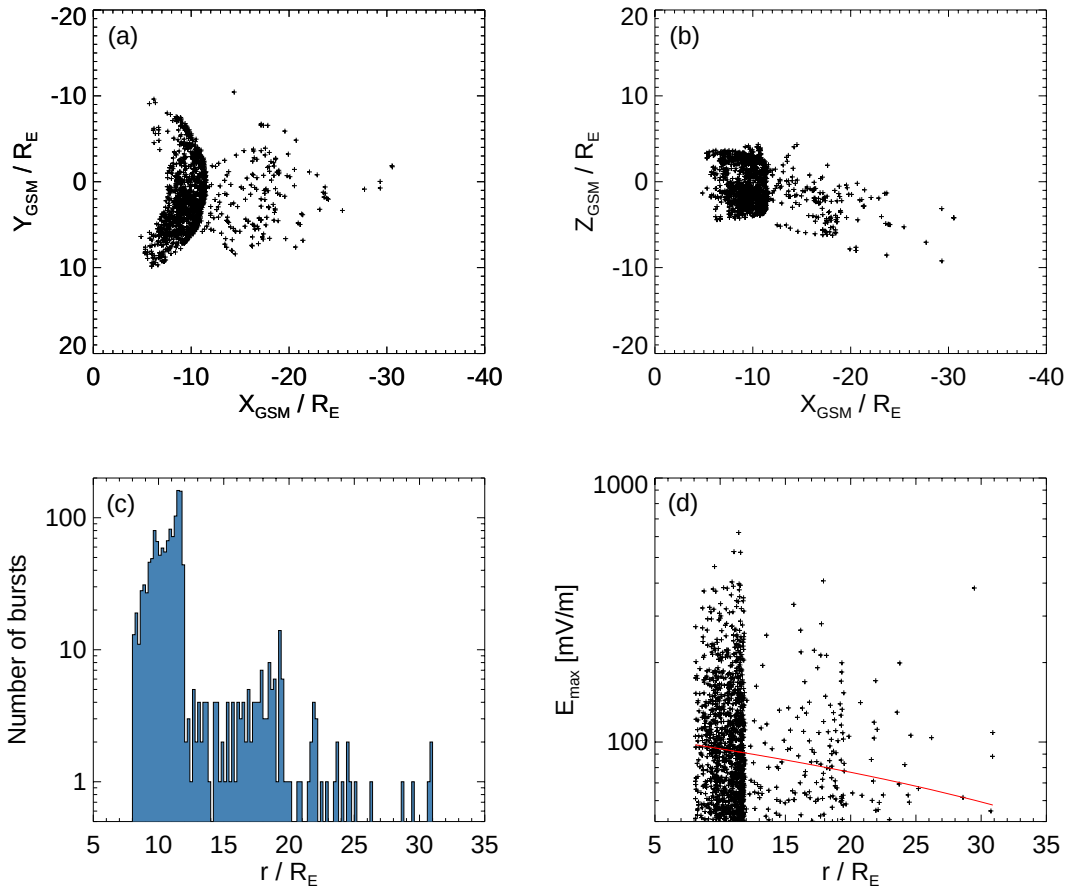

Figure 4.2: Overview of the particle bursts obtained for the study. (a) Burst locations in the GSM x-y plane. (b) Burst locations in the GSM x-z plane. (c) Distance histogram of the bursts, where r is the distance to the Earth. (d) Scatter plot of the maximum electric field in a single burst (E_{max}) versus the burst distance, where the red line is a least absolute deviation fit to the data.

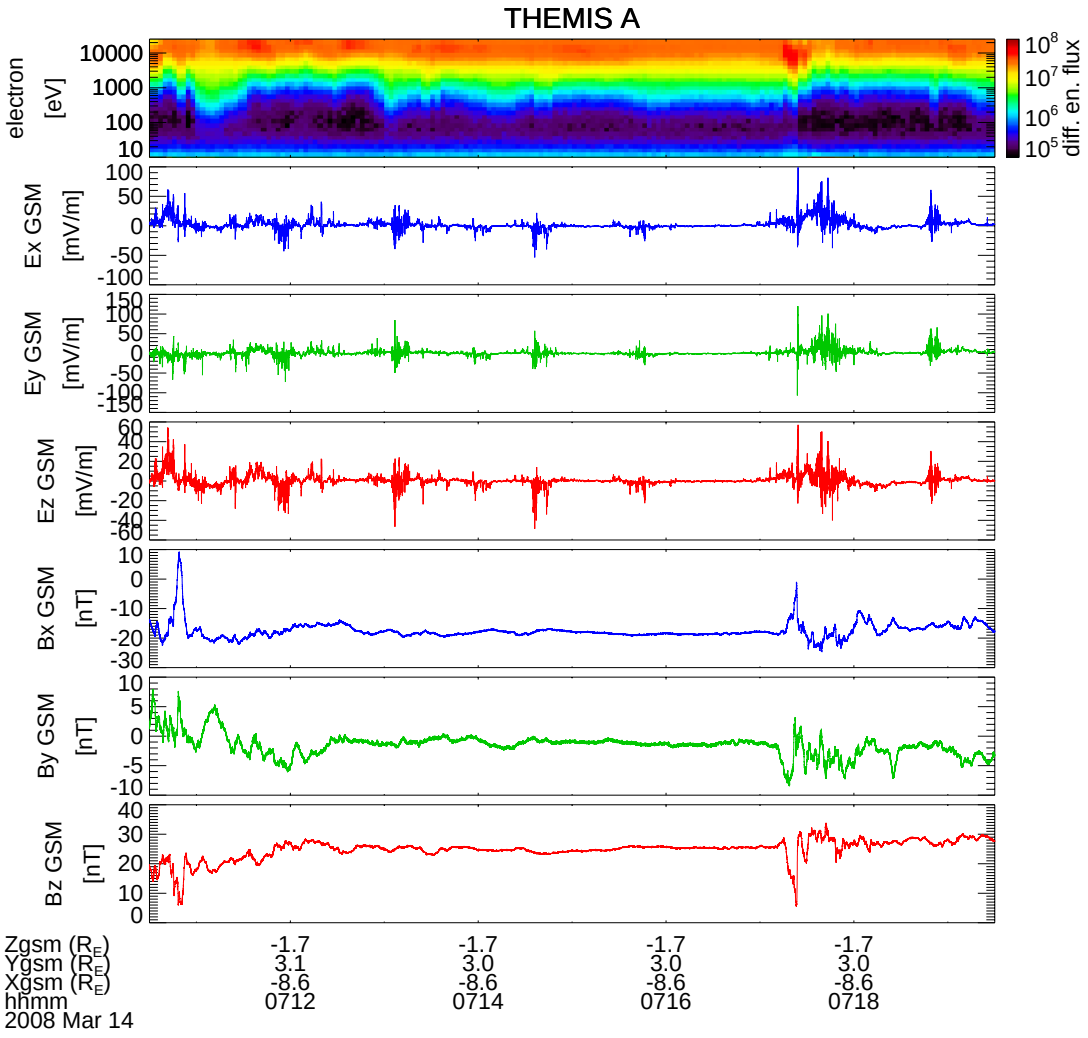

Figure 4.3: Time series of example particle-burst field waveforms in GSM coordinates except the top panel, which shows the electron differential energy flux.

sheet, δB is typically on the order of 10 nT; to have $S_{\parallel}$ on the order of 1 mW/m^2, δE should be on the order of 100 mV/m. Such strong electric fields generally last briefly in the plasma sheet, as can be seen in Figure 4.3.

The significant earthward trend of near-Earth energetic Poynting flux ($\gtrsim 0.5$ mW/m^2) in Figure 4.4 suggests that the corresponding electromagnetic energy flow is likely part of a larger-scale, earthward energy flow. The region ($r \lesssim 15\ R_E$) where energetic electromagnetic energy flux is primarily earthward coincides with the braking region of earthward high-speed ion flows (also known as bursty bulk flows (BBFs)) [*Shiokawa et al.*, 1997], suggesting that BBFs are likely one primary source of the earthward energetic electromagnetic energy flux.

The earthward energetic Poynting flux can have significant impact on the auroral region. As the magnetic field lines converge in the earthward direction, the field-aligned Poynting flux increases following a simple inverse square law, $1/d^2$, where d is the diameter of a magnetic field flux tube. The diameter d decreases by a factor of ∼30 from the magnetotail to the ionosphere, indicating that the field-aligned Poynting flux increases by a factor of ∼1000. *Angelopoulos et al.* [2002] showed that ∼90% of the field-aligned Poynting flux can be dissipated in the plasma sheet. *Dai et al.* [2011] showed that even ∼10% of 0.1 mW/m^2 field-aligned Poynting flux in the plasma sheet is sufficient to account for the kinetic energy flux observed in the auroral region based on this spatial convergence. Therefore, the earthward energetic $S_{\parallel}$ ($\gtrsim 0.5$ mW/m^2) as shown in Figure 4.4 is more than sufficient to power the kinetic energy flux in the auroral region, and the significant earthward trend in the near-Earth region suggests that the near-Earth plasma sheet is primarily responsible for the Poynting flux that powers the kinetic energy flux in the auroral region.

4.4 Spectral Slope

Hoshino et al. [1994] showed that the slopes of magnetic field spectra turn steeper near the ion gyrofrequency using Geotail data. Similar phenomena are also shown in this study. Due to this spectral turnover, two spectral slopes are obtained with least absolute deviation

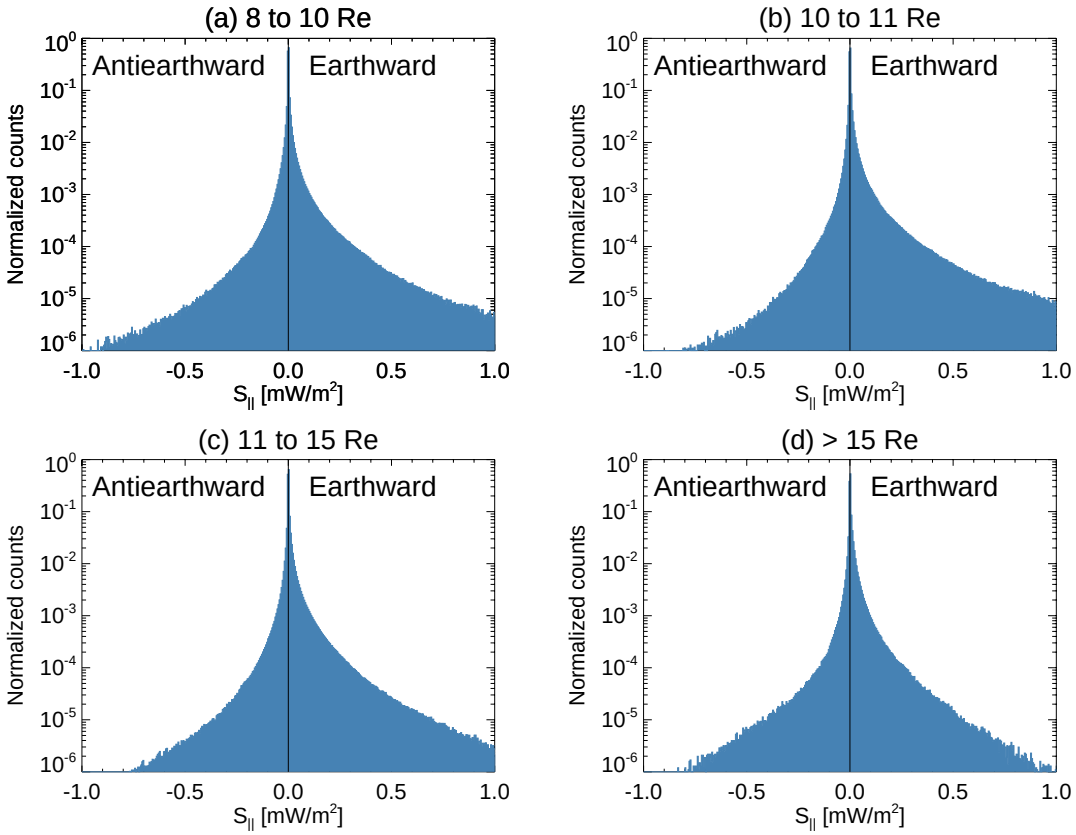

Figure 4.4: Histograms of the detrended field-aligned Poynting flux ($S_{\parallel}$) for regions of different distances to the Earth. The distance ranges are labelled in the titles of the four panels. Positive $S_{\parallel}$ is earthward, whereas negative $S_{\parallel}$ is antiearthward. The data-point counts in each histogram are normalized by the corresponding number of total data points, which is 3.4×10^7 in (a), 2.8×10^7 in (b), 5.0×10^7 in (c), and 1.2×10^7 in (d).

fits for a single 128-second-long segment of each field component, one using data in 0.01–0.3 Hz, and the other using data in 1–5 Hz. (The ion gyrofrequency is mostly between 0.2 Hz and 0.5 Hz in this study.) Before the fitting, the data are interpolated into frequency bins that are evenly spaced in logarithm scale in order to avoid the bias caused by the original linearly even-spaced frequency bins, which favors the weight of data points in higher frequency range due to its higher data-point density. Figure 4.5 shows an example of the two-range spectral slope fit.

In deriving the spectral slopes, the data are not corrected for the Doppler shift effect. Suppose ω is the frequency in the spacecraft frame and ω' is the frequency in the plasma frame. Then the Doppler shift effect gives

$$\omega = \omega' + \mathbf{k} \cdot \mathbf{v}_{plasma}, \tag{4.2}$$

where $\mathbf{v}_{plasma}$ is the velocity of the plasma medium relative to the spacecraft. Dividing Equation (4.2) by ω' gives

$$\frac{\omega}{\omega'} = 1 + \frac{\mathbf{k}}{k} \cdot \frac{\mathbf{v}_{plasma}}{v_{ph}}, \tag{4.3}$$

where $v_{ph} = \omega'/k$ is the phase velocity of the waves in the plasma frame. In the plasma sheet, v_{plasma} is typically on the order of 100 km/s, and v_{ph} is generally larger than the Alfvén speed, which is typically on the order of 1000 km/s; in other words, $v_{plasma} \ll v_{ph}$. Therefore, Doppler shifts are generally negligible in the plasma sheet.

Four subsets of 128-second-long segments are obtained based on the distance to the Earth and the strength of the fluctuations, which is characterized by the maximum δE for each segment (δE_{max}). The four subsets are numbered as follows:

- Subset 1: $r < 15\ R_E$, $\delta E_{max} > 50$ mV/m.
- Subset 2: $r < 15\ R_E$, $\delta E_{max} < 10$ mV/m.
- Subset 3: $r > 15\ R_E$, $\delta E_{max} > 50$ mV/m.

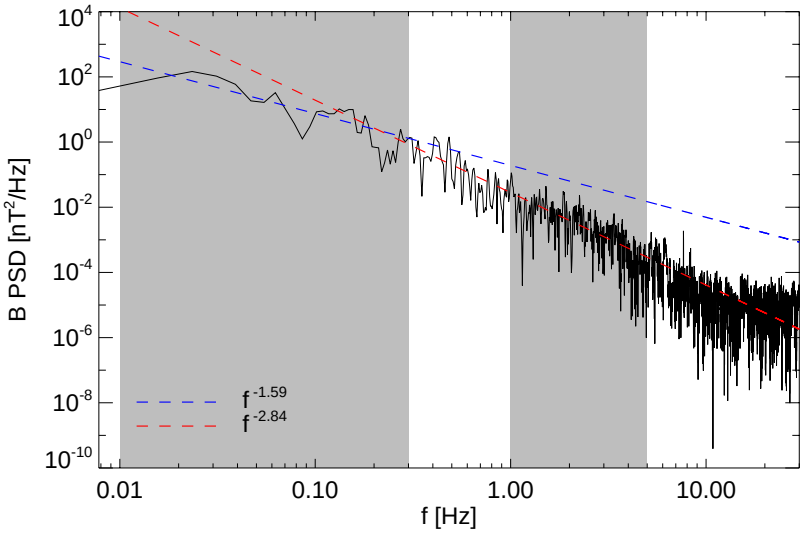

Figure 4.5: Example of the two-range spectral slope fit. The two gray areas indicate the two frequency ranges. The blue line is from the range 0.01–0.3 Hz, and the red line is from the range 1–5 Hz. In this example, the low-frequency spectral index is 1.59, and the high-frequency spectral index is 2.84.

- Subset 4: $r > 15\ R_E$, $\delta E_{max} < 10$ mV/m.

Tables 4.1 and 4.2 summarize the average spectral slopes with standard deviations of the four subsets for the frequency ranges 0.01–0.3 Hz and 1–5 Hz, respectively, where the fields are in the FAC system (see page 20 for the definition of the FAC system). The following features are shown in the two tables:

- The spectral slopes of electric fields are generally smaller than those of magnetic fields for both frequency ranges.

- The distance conditions $r < 15\ R_E$ and $r > 15\ R_E$ do not make significant differences in the spectral slopes.

- Strong fluctuations and weak fluctuations have significantly different spectral slopes for both magnetic fields and electric fields in the frequency range 0.01–0.3 Hz. For strong fluctuations (subsets 1 and 3), the perpendicular magnetic field components (δB_x and δB_y) have spectral slopes of $\sim$1.8, and the parallel magnetic field component (δB_z) has an spectral slope of $\sim$2; the perpendicular electric field components (δE_x and δE_y) have spectral slopes of $\sim$1.2, and the parallel electric field component (δE_z) has an spectral slope of $\sim$1.1. For weak fluctuations (subsets 2 and 4), the perpendicular magnetic field components (δB_x and δB_y) have spectral slopes of $\sim$2.45, and the parallel magnetic field component (δB_z) has an spectral slope of $\sim$2.6; the perpendicular electric field components (δE_x and δE_y) have spectral slopes of $\sim$1.5, and the parallel electric field component (δE_z) has an spectral slope of $\sim$1.6.

- In the frequency range 1–5 Hz, the spectral slopes of magnetic fields are generally $\sim$3, whereas those of electric fields are different between strong and weak fluctuations with slopes < 1 for strong fluctuations and slopes $\sim$1.4–1.5 for weak fluctuations.

- The standard deviations of the spectral slopes are relatively large, especially for electric fields, suggesting that the underlying dynamics of the turbulent electric and

magnetic fields in the plasma sheets has a wide range of complexity, and that the significance of the spectral slope differences described above, especially for differences less than 0.2, is still open to further investigations.

Table 4.1: Average spectral slopes with standard deviations of the four subsets of the data in the frequency range 0.01–0.3 Hz

Subset	δB_x	δB_y	δB_z	δE_x	δE_y	δE_z
1	1.81±0.56	1.81±0.57	2.02±0.65	1.21±0.53	1.18±0.50	1.10±0.51
2	2.48±0.60	2.43±0.59	2.58±0.62	1.42±0.62	1.50±0.59	1.62±0.56
3	1.83±0.59	1.84±0.56	2.14±0.57	1.31±0.53	1.27±0.50	1.06±0.43
4	2.43±0.56	2.44±0.55	2.61±0.59	1.48±0.61	1.52±0.54	1.57±0.54

Table 4.2: Average spectral slopes with standard deviations of the four subsets of the data in the frequency range 1–5 Hz

Subset	δB_x	δB_y	δB_z	δE_x	δE_y	δE_z
1	3.05±0.46	2.98±0.49	2.83±0.48	0.79±0.56	0.84±0.56	0.84±0.74
2	2.92±0.55	2.98±0.51	3.05±0.55	1.54±0.67	1.40±0.62	1.42±0.75
3	3.10±0.50	2.98±0.57	2.84±0.54	0.51±0.60	0.61±0.53	0.32±0.74
4	3.23±0.42	3.04±0.56	3.18±0.45	1.49±0.72	1.30±0.63	1.34±0.84

4.5 A Two-Species Cold Plasma System

Among other spectral features, it is rather universal that δE has flatter spectral slopes than δB, which raises the following questions: Is this feature an intrinsic property of a plasma system? What about other spectral features? To attack these questions, one needs a

fundamental model that captures intrinsic dynamics of plasma systems. The homogeneous cold plasma model [*Stix*, 1992, p.3–9] is an ideal candidate for that purpose. Although it ignores inhomogeneity and kinetic effects, the cold plasma model retains all the fundamental modes to a plasma system and its validity is not limited in scales, as opposed to the MHD model. That said, the cold plasma model provides a necessary frequency coverage that enables comparisons between theoretical results and observations with frequencies below and above the ion gyrofrequency. In addition, by ignoring kinetic effects, the cold plasma model is much easier to tackle mathematically than a kinetic model, and hence is a good place to start with. Note that, as a linear system, the cold plasma model is not able to address the absolute values of the spectral slopes of δE and δB. However, it can address the spectral slope differences between δE and δB by taking their ratios.

The plasma sheet is primarily composed of protons and electrons. Therefore, a two-species cold plasma model, which is composed of one electron species with charge $-e$ and mass m_e and one ion species with charge e and mass m_i, is considered in this chapter. This section describes general results of such a system.

Generally, for a cold-plasma system, we have [*Stix*, 1992, p.8]

$$\begin{pmatrix} S-n^2\cos^2\theta & -iD & n^2\cos\theta\sin\theta \\ iD & S-n^2 & 0 \\ n^2\cos\theta\sin\theta & 0 & P-n^2\sin^2\theta \end{pmatrix} \begin{pmatrix} \delta E_x \\ \delta E_y \\ \delta E_z \end{pmatrix} = 0, \tag{4.4}$$

where $n = kc/\omega$, $S = (R+L)/2$, and $D = (R-L)/2$. For the two-species system, we have

$$P = 1 - \frac{1}{\tilde{\omega}^2}\alpha\eta^2 - \frac{1}{\tilde{\omega}^2}\eta^2, \tag{4.5}$$

$$R = 1 - \frac{1}{\tilde{\omega}(\tilde{\omega}-\alpha)}\alpha\eta^2 - \frac{1}{\tilde{\omega}(\tilde{\omega}+1)}\eta^2 \tag{4.6}$$

$$L = 1 - \frac{1}{\tilde{\omega}(\tilde{\omega}+\alpha)}\alpha\eta^2 - \frac{1}{\tilde{\omega}(\tilde{\omega}-1)}\eta^2, \tag{4.7}$$

where $\tilde{\omega} = \omega/\Omega_i$, $\alpha = m_i/m_e$, $\eta = c/v_A$, $v_A = \sqrt{\frac{B_0^2}{\mu_0 n_0 m_i}}$ is the Alfvén speed, n_0 is the number density of ions, $\tilde{k} = kd_i$, and $d_i = c/\omega_{pi}$ is the ion inertial length.

For the cold-plasma system, the coordinate system is chosen such that the background magnetic field is in the z-axis direction and the wave vector $\mathbf{k}$ is in the x-z plane; namely, $\mathbf{B}_0 = B_0\hat{\mathbf{z}}$ and $\mathbf{k} = k_x\hat{\mathbf{x}} + k_z\hat{\mathbf{z}} = k\sin\theta\hat{\mathbf{x}} + k\cos\theta\hat{\mathbf{z}}$, where θ is the angle between $\mathbf{B}_0$ and $\mathbf{k}$. Note that the perpendicular directions in such a coordinate system do not necessarily coincide with those in the FAC system (page 20); however, such differences do not matter for comparing the ratios $\delta E_x/\delta B_y$ and $\delta B_\parallel/\delta B_\perp$.

In this chapter, the mass ratio α and the Alfvén speed v_A are chosen to be 1836 and 1000 km/s, respectively, for cold-plasma results. These choices represent typical values of α and v_A in the plasma sheet.

4.5.1 Dispersion relation

By setting the determinant of the 3-by-3 matrix on the left-hand side of Equation (4.4) equal to zero, one can obtain the dispersion equation of the two-species system as

$$a_0 + a_1\tilde{\omega}^2 + a_2\tilde{\omega}^4 + a_3\tilde{\omega}^6 + a_4\tilde{\omega}^8 + \tilde{\omega}^{10} = 0, \tag{4.8}$$

where

$$a_0 = -\alpha^2(1+\alpha)\eta^6\mathrm{Cos}[\theta]^2\tilde{k}^4, \tag{4.9}$$

$$\begin{aligned} a_1 = {} & \frac{1}{2}\eta^4\tilde{k}^2(\alpha(1+\alpha)(\alpha+(1+\alpha)\eta^2)(3+\mathrm{Cos}[2\theta]) \\ & + (2\alpha^2+(1+\alpha)(1+\alpha+\alpha^2)\eta^2+(1+\alpha^3)\eta^2\mathrm{Cos}[2\theta])\tilde{k}^2), \end{aligned} \tag{4.10}$$

$$\begin{aligned} a_2 = {} & -\frac{1}{2}\eta^2(2(1+\alpha)(\alpha+(1+\alpha)\eta^2)^2 \\ & + (4\alpha^2+(1+\alpha)(3+\alpha(5+3\alpha))\eta^2+4(1+\alpha)^2\eta^4 \\ & + (1+\alpha^3)\eta^2\mathrm{Cos}[2\theta])\tilde{k}^2+2\eta^2(1+\alpha^2+(1+\alpha)\eta^2)\tilde{k}^4), \end{aligned} \tag{4.11}$$

$$a_3 = \alpha^2+(1+\alpha)^3\eta^2+3(1+\alpha)^2\eta^4+2\eta^2(1+\alpha^2+2(1+\alpha)\eta^2)\tilde{k}^2+\eta^4\tilde{k}^4, \tag{4.12}$$

$$a_4 = -1-\alpha^2-3(1+\alpha)\eta^2-2\eta^2\tilde{k}^2 \tag{4.13}$$

In general, there are five wave branches in total from Equation (4.8), of which the whistler branch and the shear Alfvén wave branch are within the frequency range of interest.

The other three branches are of frequencies much higher than the electron gyrofrequency, which is much higher than the sample rate of the data used in this study. One special case of the solutions of Equation (4.8) is that the shear Alfvén wave branch reduces to a trivial solution ($\tilde{\omega} = 0$) when $\theta = \pi/2$. This can be seen from the expression of a_0, as in Equation (4.9): When $\theta = \pi/2$, a_0 becomes zero, and thus $\tilde{\omega} = 0$ becomes a solution to Equation (4.8).

Figure 4.6 shows the dispersion relations of the whistler branch and the shear Alfvén wave branch for various θ. As θ goes from 0° (parallel propagation) to nearly 90° (perpendicular propagation), the low-frequency part ($\omega/\Omega_i < 1$) of the whistler branch, namely, the MHD fast mode, is nearly constant, whereas the high-frequency part (ω/Ω_i) of the whistler branch shifts downward in frequency, with the stop band of the branch moving from the electron gyrofrequency Ω_e to the lower hybrid frequency (ω_{LH}). On the other hand, as θ increases, the shear Alfvén wave branch generally shifts downward but remains almost unchanged when $\theta < 45°$; the stop band of the branch remains at the ion gyrofrequency Ω_i except when θ is very close to 90° as shown in Figure 4.6(h).

4.5.2 Component ratio

Given a solution of the dispersion relation (4.8), one cannot determine the absolute value of the eigenvector $\delta\mathbf{E}$ from Equation (4.4) since the equation is homogeneous. However, one can express the eigenvector in terms of one component. For example, one can express $\delta\mathbf{E}$ in terms of δE_x, i.e., $\delta\mathbf{E} = (\delta E_x, c_1\delta E_x, c_2\delta E_x)$, where c_1 and c_2 are determined from Equation (4.4). Then, one can obtain $\delta\mathbf{B}$ from Faraday's law:

$$\mathbf{k} \times \delta\mathbf{E} = \omega\delta\mathbf{B}. \tag{4.14}$$

Since the ratios between any two components from $\delta\mathbf{E}$ and $\delta\mathbf{B}$ can be determined, spectral behavior comparisons of $\delta\mathbf{E}$ and $\delta\mathbf{B}$ between observations and cold-plasma results can be achieved by taking component ratios. The underlying assumption of such comparisons

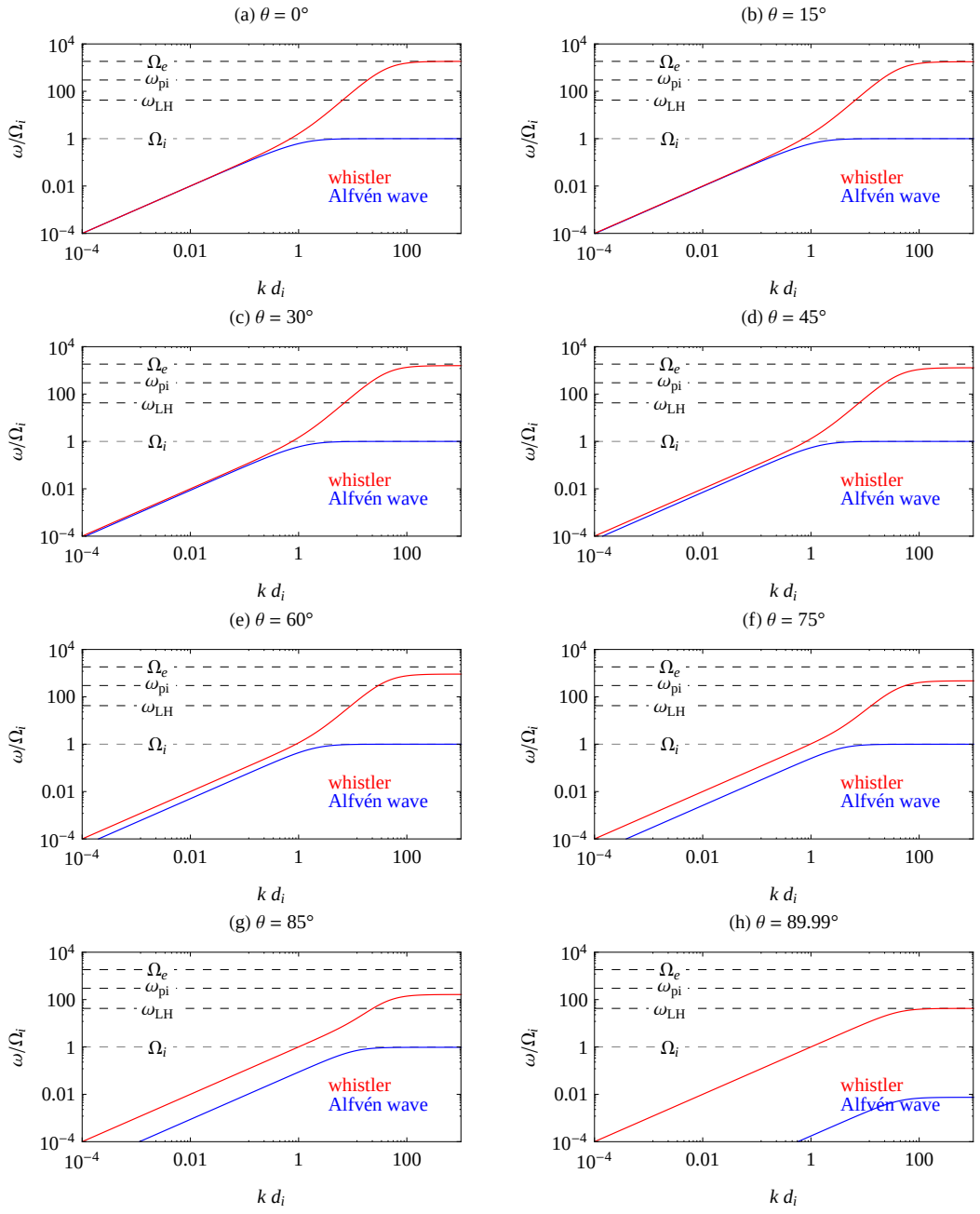

Figure 4.6: Dispersion relations of the whistler branch (red) and the shear Alfvén wave branch (blue) for various θ in the two-species system. The electron gyrofrequency (Ω_e), ion plasma frequency (ω_{pi}), lower hybrid frequency ω_{LH}, and ion gyrofrequency (Ω_i) are indicated by the horizontal dashed lines.

is that the component ratios of normal plasma modes are sustained even when the waves are in a nonlinear stage, despite the fact that the ratios are calculated from a linear theory. Chapter 3 provides supporting cases to this assumption. As shown in Figures 3.11(b) and 3.12(b), the dispersion relations derived from the nonlinear stages of the simulations match the linear-analysis results quite well.

Figure 4.7 shows the behavior of $|\delta E_x/\delta B_y|$ as a function of frequency for various θ for the two-species system. According to Faraday's law, one has

$$\left|\frac{\delta E_x}{\delta B_y}\right| = \left|\frac{\omega}{k\cos\theta} + \tan\theta\frac{\delta E_z}{\delta B_y}\right|. \tag{4.15}$$

As shown later, δE_z (or $\delta E_\parallel$) is generally negligible except when the frequency is close to the ion or the electron gyrofrequency. Therefore, the second term on the right-hand side of Equation (4.15) is generally negligible except when θ is close to $\pi/2$ (i.e., quasi-perpendicular) or when the frequency is close to the ion or the electron gyrofrequency (i.e., cyclotron resonance). Therefore, $|\delta E_x/\delta B_y|$ is generally a good estimate of the phase velocity ω/k except for quasi-perpendicular propagation or cyclotron resonance. The spectral behavior of $|\delta E_y/\delta B_x|$ is nearly identical to that of $|\delta E_x/\delta B_y|$ in the frequency range shown in Figure 4.7.

Figure 4.8 shows the behavior of $|\delta B_\parallel/\delta B_\perp|$ as a function of frequency for various θ in the two-species system. For quasi-parallel propagation, i.e., $\theta \approx 0$, one has $\delta B_\parallel \approx 0$ for both the whistler branch and the shear Alfvén wave branch, as shown in Figure 4.8(a). As θ increases, the importance of $\delta B_\parallel$ relative to $\delta B_\perp$ generally increases; the whistler branch shows a transition of $|\delta B_\parallel/\delta B_\perp|$ around the ion gyrofrequency.

Figure 4.9 shows the behavior of $|\delta E_\parallel/\delta E_\perp|$ as a function of frequency for various θ in the two-species system. In general, $\delta E_\parallel$ is much less than $\delta E_\perp$ except when frequency is very close to the ion gyrofrequency for the shear Alfvén wave branch or to the electron gyrofrequency for the whistler branch. The whistler branch behaves similarly to the shear Alfvén wave branch when the frequency approaches to the electron gyrofrequency, namely, $|\delta E_\parallel/\delta E_\perp|$ increases rapidly with the increase of the frequency.

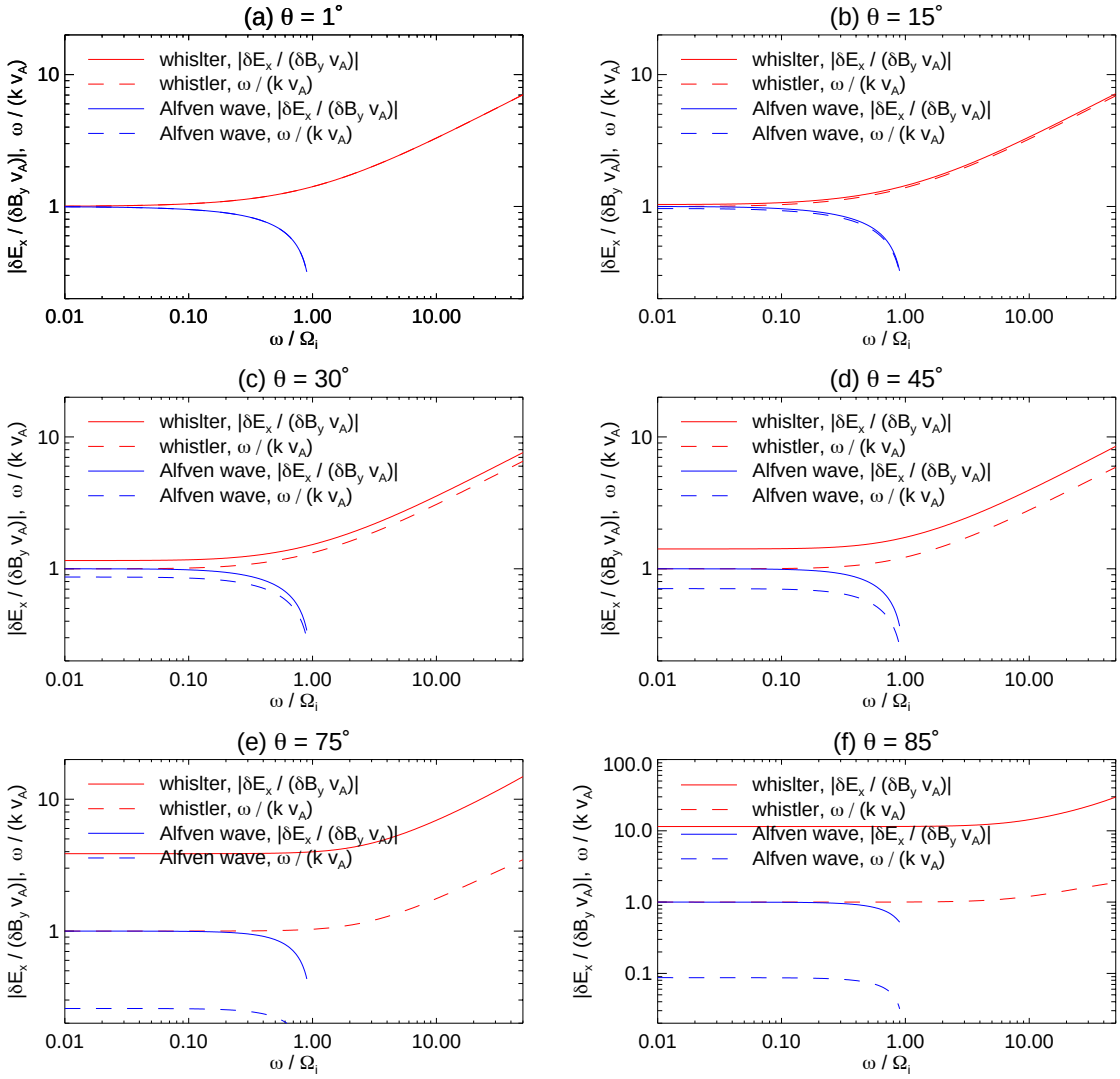

Figure 4.7: Behavior of $|\delta E_x/\delta B_y|$ as a function of frequency for various θ in the two-species system, compared to the phase velocity (ω/k). The red solid ($|\delta E_x/\delta B_y|$) and dashed (ω/k) lines correspond to the whistler branch, whereas the blue lines correspond to the shear Alfvén wave branch. Both $|\delta E_x/\delta B_y|$ and ω/k are normalized with the Alfvén speed v_A.

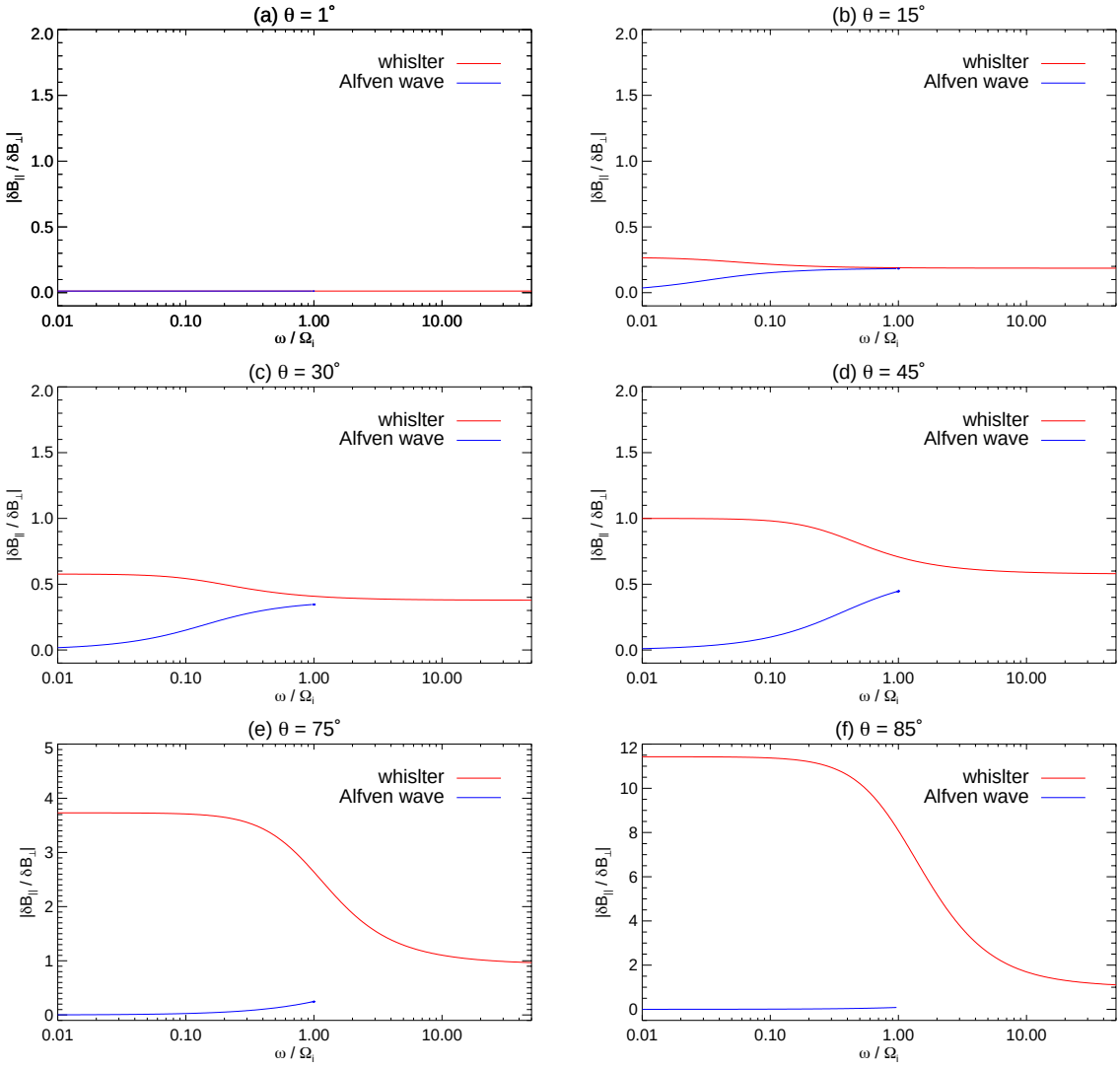

Figure 4.8: Behavior of $|\delta B_{\parallel}/\delta B_{\perp}|$ as a function of frequency for various θ in the two-species system. The red line corresponds to the whistler branch, whereas the blue line corresponds to the shear Alfvén wave branch.

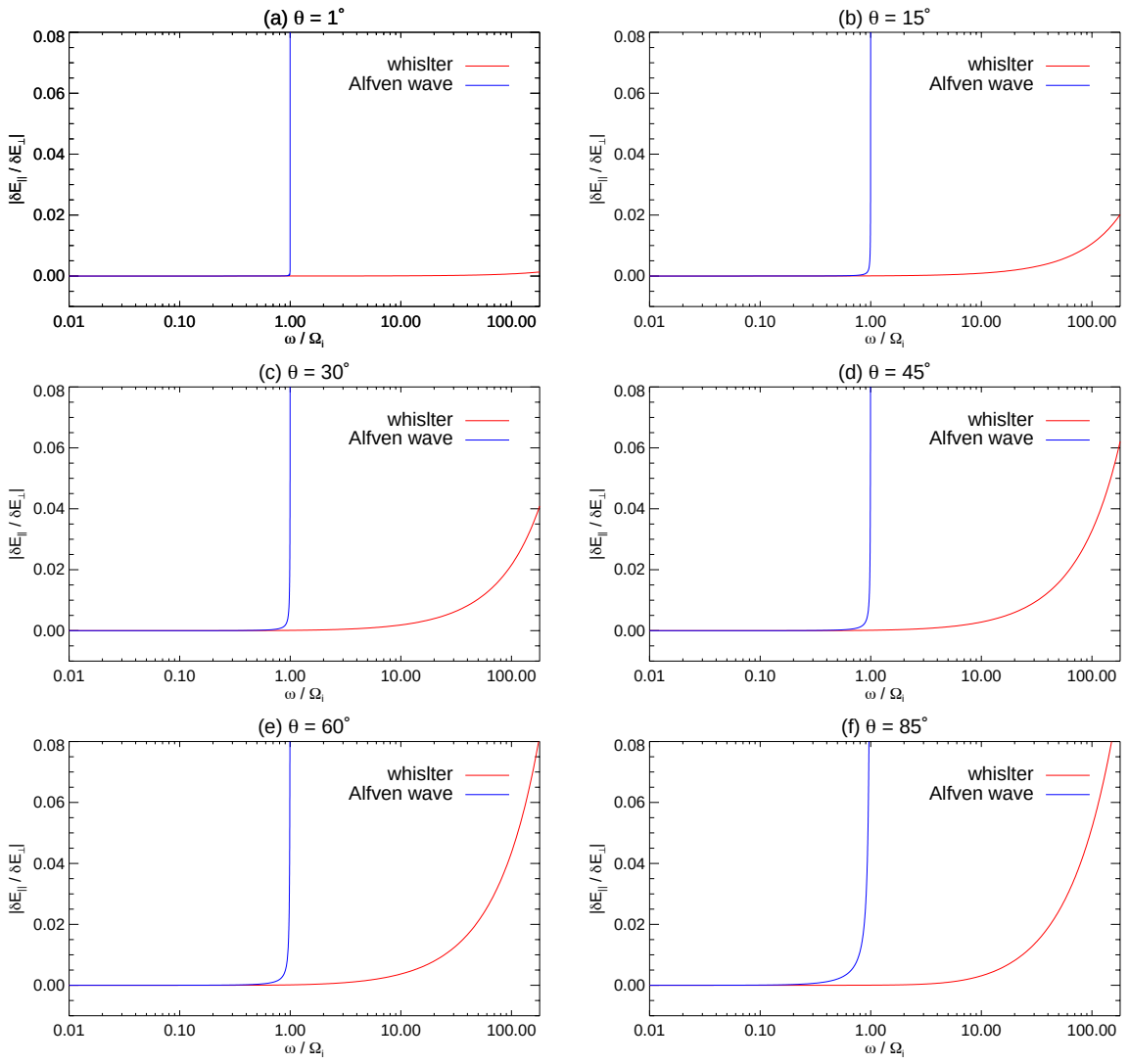

Figure 4.9: Behavior of $|\delta E_{\parallel}/\delta E_{\perp}|$ as a function of frequency for various θ in the two-species system. The red line corresponds to the whistler branch, whereas the blue line corresponds to the shear Alfvén wave branch.

4.6 Comparisons Between Observations and Cold-Plasma Results

4.6.1 $\delta E_x/\delta B_y$

Figure 4.10 shows the spectral behavior of observed $\delta E_x/\delta B_y$ compared to cold-plasma results. *Chaston et al.* [2008] presented a similar comparison between the observed $\delta E_x/\delta B_y$ and the local inertial Alfvén wave dispersion in a study of the turbulent Alfvénic aurora. The average of the observations is done in logarithm scale, namely, $\text{Avg}[\delta E_x/\delta B_y] = \exp[\frac{1}{N}\sum^N \ln(\delta E_x/\delta B_y)]$, where Avg[ ] stands for the average operation. This average operation has the advantage of reducing the significance of extreme values. From the two-species system with $\theta = 45°$, the two dashed lines in Figure 4.10 serve as intermediate representatives of cold plasma results. (The choice of $\theta = 45°$ is not an optimized one but rather an intermediate one between parallel and perpendicular propagations.) In general, the ratio $\delta E_x/\delta B_y$ increases as frequency increases, especially for $f/f_{ci} \gtrsim 0.1$. The spectral behavior of the observed $\delta E_y/\delta B_x$ is nearly identical to that of the observed $\delta E_x/\delta B_y$.

In the low-frequency regime ($f/f_{ci} \lesssim 0.1$), $\delta E_x/\delta B_y$ is close to the Alfvén speed for the strong-fluctuation subsets as shown by the black and red solid lines in Figure 4.10. As shown in Figure 4.7, the shear Alfvén wave branch has $\delta E_x/\delta B_y$ close to v_A in this frequency regime for all propagation angles except for quasi-perpendicular propagation; the whistler branch manifests similar behavior for small θ. Therefore, based on cold plasma results, the strong-fluctuation observations suggest that the electromagnetic energy in the plasma sheet likely lies primarily on the shear Alfvén wave branch or the low-θ whistler branch. In the same frequency regime, $\delta E_x/\delta B_y$ is close to the half Alfvén speed for the weak-fluctuation subsets as shown by the blue and cyan solid lines in Figure 4.10. Such a low value of $\delta E_x/\delta B_y$ is not expected based on the cold plasma results. Although kinetic effects are not accounted for in the cold plasma results, they are not expected to play an important role in such a low frequency regime. Measurement errors are relatively significant in this low-frequency regime for weak fluctuations; thus, they may be responsible for such a low value of $\delta E_x/\delta B_y$.

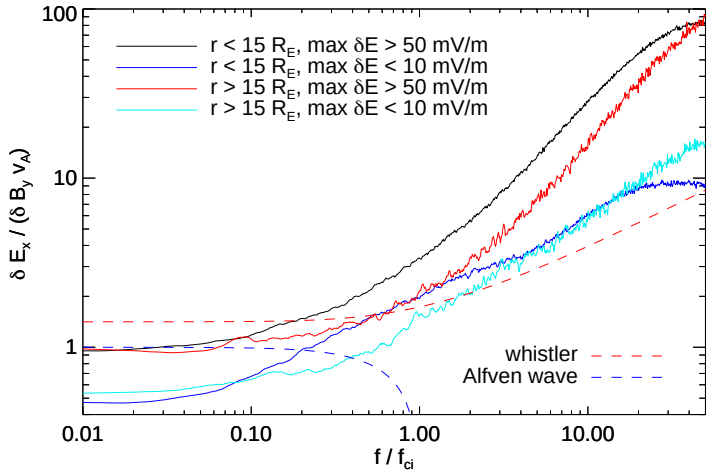

Figure 4.10: Spectral behavior of observed $\delta E_x/\delta B_y$ averaged over the four subsets (solid lines), respectively, and results from the two-species cold plasma system with $\theta = 45°$ (dashed lines). The meanings of the colors are indicated by the legends in the figure. The frequency is normalized by the ion gyrofrequency (f_{ci}), and the ratio $\delta E_x/\delta B_y$ is normalized by the Alfvén speed (v_A).

Nevertheless, the nature of this result is not certain and under further investigation.

In the higher-frequency regime ($f/f_{ci} \gtrsim 0.1$), the weak-fluctuation averages (the blue and cyan solid lines in Figure 4.10) roughly follow the whistler branch, suggesting that the turbulent electromagnetic fields of weak fluctuations in the plasma sheet with distance 8–30 R_E to the Earth can be roughly treated as a superposition of linear normal-mode cold plasma waves. However, for strong fluctuations, the observed $\delta E_x/\delta B_y$ grows much faster than that of the $\theta = 45°$ whistler branch. For cold plasma results to be able to account for the observed values of $\delta E_x/\delta B_y$ in this frequency regime, θ must approach 90° rapidly as frequency increases, which is unlikely for the observations. Instead, it is likely that kinetic effects become more and more important for strong fluctuations as frequency increases in the regime $f/f_{ci} \gtrsim 0.1$ and the kinetic effects primarily produce electrostatic waves so that the average of the observed $\delta E_x/\delta B_y$ increases much faster than the cold plasma result.

4.6.2 $\delta B_\parallel/\delta B_\perp$

While $\delta\mathbf{E}$ can be due to electrostatic waves or electromagnetic waves or both, $\delta\mathbf{B}$ is only due to electromagnetic waves. The ratio $\delta B_\parallel/\delta B_\perp$ provides a means to examine the electromagnetic waves in the observations. Figure 4.11 shows the spectral behavior of the observed $\delta B_\parallel/\delta B_\perp$ averaged over the four subsets, respectively. The observed curves of $\delta B_\parallel/\delta B_\perp$ of the four subsets generally lie between the corresponding theoretical curves from the two-species cold plasma system with $\theta = 15°$ and $\theta = 75°$, respectively. Therefore, there always exist positive coefficients c_1 and c_2 satisfying $c_1 + c_2 = 1$, such that a superposition given by

$$\left.\frac{\delta B_\parallel}{\delta B_\perp}\right|_{observed} = c_1 \left.\frac{\delta B_\parallel}{\delta B_\perp}\right|_{\theta=15°} + c_2 \left.\frac{\delta B_\parallel}{\delta B_\perp}\right|_{\theta=75°} \tag{4.16}$$

can be achieved for a given frequency. The right column of Figure 4.11 shows the spectral behavior of the superposition coefficients c_1 (the black line) and c_2 (the red line), which are moving-averaged over 200 frequency bins.

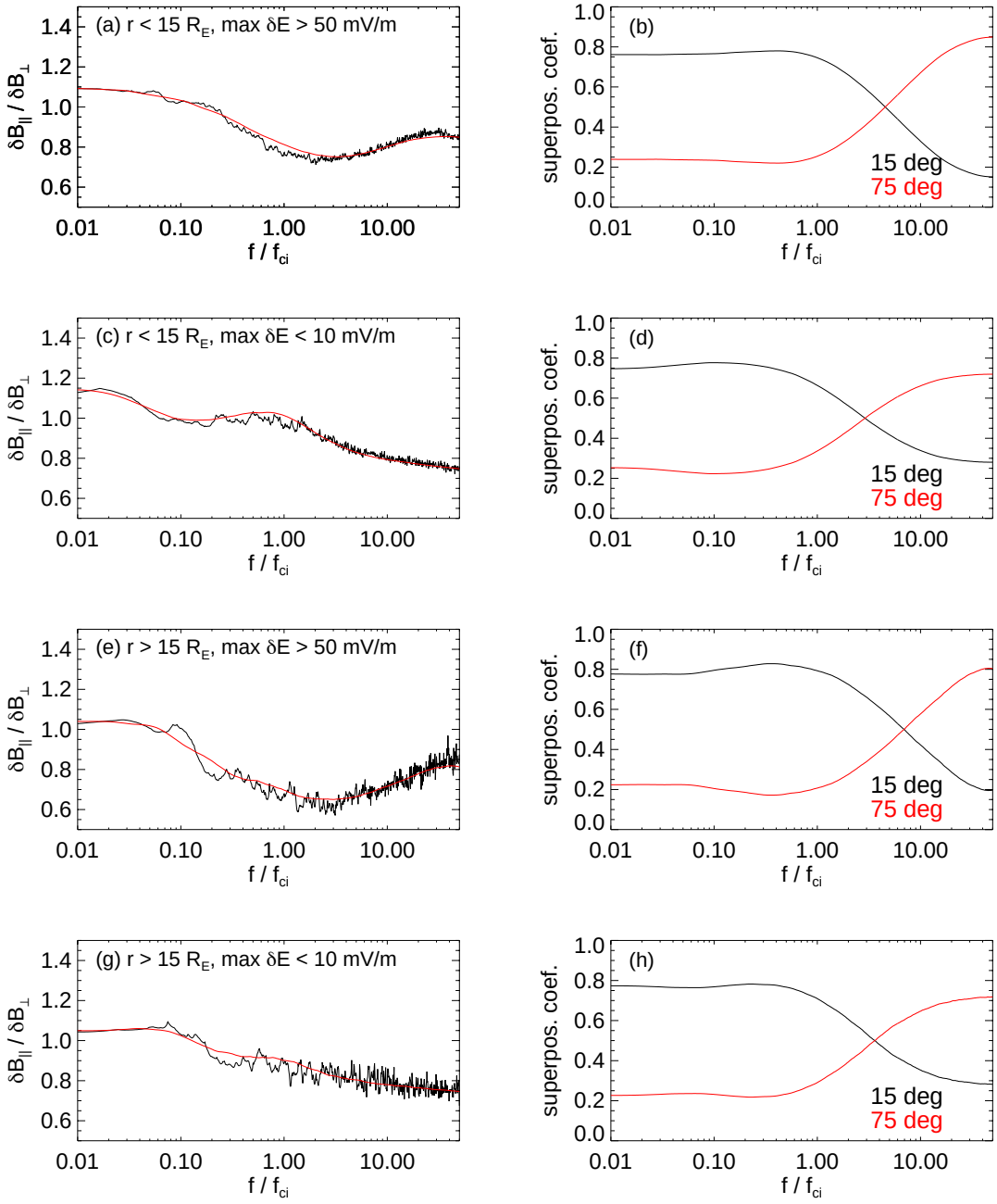

Figure 4.11: Left column: Spectral behavior of the observed $\delta B_{\parallel}/\delta B_{\perp}$ (black) with a fit from the two-species cold plasma system (red). Right column: The superposition coefficients that generate the fit on the left column according to Equation (4.16). The four rows correspond to the four subsets. The frequency is normalized by the ion gyrofrequency.

The left column of Figure 4.11 shows that the spectral behavior of $\delta B_{\parallel}/\delta B_{\perp}$ is similar between $r < 15\ R_E$ and $r > 15\ R_E$ for strong and weak fluctuations, respectively, but it is significantly different between weak and strong fluctuations. The spectral behavior of the coefficients c_1 and c_2 as shown on the right column of Figure 4.11, on the other hand, are generally similar for the four subsets, except that c_2 approaches a larger value for strong fluctuations than for weak fluctuations as frequency increases. c_1 and c_2 measure the importance of near-parallel waves and near-perpendicular waves, respectively. The general behavior of c_1 and c_2 as shown in Figure 4.11 suggests that the propagation of the electromagnetic waves are primarily near parallel for $f/f_{ci} < 1$ and becomes near perpendicular for $f/f_{ci} \gtrsim 10$. However, cold-plasma theory is not able to explain or verify this result; instead, kinetic theory is needed. One possibility is that, given the conditions in the plasma sheet, near-parallel waves are less damped for $f/f_{ci} < 1$, whereas near-perpendicular waves are less damped for $f/f_{ci} \gtrsim 10$.

4.7 Discussion

Two major pieces of physics are missing in the cold plasma model: nonlinearity and kinetic effects. Thus, the findings from comparing cold-plasma results and turbulence observations are only suggestive but not conclusive. Nevertheless, one aspect of the importance of this study is that the spectral results from the cold-plasma theory can serve as a baseline to be compared with turbulence spectra from observations and simulations. Such comparisons can help identify the importance of nonlinear and/or kinetic effects.

The deviation between the cold plasma result and the observations occurs roughly at the ion gyrofrequency as shown in Figure 4.10. Based on the dispersions shown in Figure 4.6, $f \sim f_{ci}$ corresponds to $k \sim d_i$ for the whistler branch. In the plasma sheet, d_i and ρ_i (ion gyroradius) are both on the order of 100 km. Since d_i is included in the cold plasma model, it is likely that ρ_i, rather than d_i, is the critical scale, below and around which kinetic effects become generally important.

The distance conditions $r < 15\ R_E$ and $r > 15\ R_E$ do not have significant effects for the spectral behaviors of $\delta E_x/\delta B_y$ and $\delta B_\parallel/\delta B_\perp$ as shown in Figures 4.10 and 4.11, respectively. In the plasma sheet, as the distance to the Earth goes from $\sim$10 R_E to $\sim$30 R_E, the plasma beta (β) goes from a intermediate level ($\beta \sim 1$) to a high-beta level ($\beta \sim 10$). Due to the connection between the distance and the plasma beta, the insignificance of distance to the spectral behaviors of $\delta E_x/\delta B_y$ and $\delta B_\parallel/\delta B_\perp$ suggests that the plasma beta does not have a significant impact on the spectral behaviors of turbulent electric and magnetic fields in the plasma sheet. The insignificance of plasma beta may also suggest that the observed spectral results bear some universal spectral features of turbulent electric and magnetic fields in plasmas. *Borovsky and Funsten* [2003] proposed that "turbulence in a box" would be a better description of the plasma sheet turbulence compared to the effectively boundary-free solar wind turbulence. Therefore, one further step to verify the potential universality of these findings, such as the propagation angle changes from low frequencies to high frequencies as shown in Figure 4.11, would be applying the same analysis to electric and magnetic field measurements in the solar wind.

4.8 Summary

A statistical study of turbulent electric and magnetic fields in the Earth's plasma sheet is presented in this chapter. Compared to previous works, it includes statistical features of turbulent electric fields, which are not previously addressed, and an extensive frequency coverage from $f < f_{ci}$ (MHD scales) to $f > f_{ci}$ (kinetic scales). The cold plasma model is used to help understand the observed spectral features of δE and δB, which is an original approach for studying turbulence in plasmas.

To sum up, the statistical features of turbulent electric and magnetic fields in the Earth's plasma sheet include:

- The amplitudes of electric field perturbations generally decrease as the distance to

the Earth increases;

- strong field-aligned Poynting flux is predominantly earthward in the near-Earth plasma sheet;
- the slopes of electric field spectra are generally smaller (or flatter) than those of magnetic field spectra;
- the magnetic field spectra turn steeper near the ion gyrofrequency as frequency increases;
- kinetic effects become generally important for strong fluctuations when $f \gtrsim f_{ci}$ based on the observations of $\delta E_x/\delta B_y$; and
- near-parallel propagation and near-perpendicular propagation dominate for $f \lesssim f_{ci}$ and $f \gtrsim 10 f_{ci}$, respectively.

Chapter 5

Future Work

5.1 Electron Phase-Space Holes

As demonstrated in Chapter 2, electromagnetic EHs likely have large spatial sizes (tens of the local Debye length) and carry strong potentials (comparable to the local electron temperature), as opposed to sizes of a few Debye length and potentials much less than the local electron temperature from previous observations [*Franz et al.*, 2005]. These features indicate that electromagnetic EHs may play an important role in the plasma sheet. To further our understanding of electromagnetic EHs, a statistical study of electromagnetic EHs is needed. THEMIS has accumulated a large data set from four tail seasons, each roughly four months long. Such a large data set offers an excellent opportunity for that study. The following questions can be addressed by the proposed statistical study.

(1) What are the statistical features of the electromagnetic EH properties, including their velocities, sizes, potentials, propagation directions (earthward or anti-earthward), and observed locations in the plasma sheet? This work will be valuable for determining the generation mechanism of electromagnetic EHs and assessing their effects in the plasma sheet.

(2) What large-scale phenomena are associated with the electromagnetic EHs in the plasma sheet and how are they related? For instance, our preliminary results show that the electromagnetic EHs are often associated with Bursty Bulk Flows (BBFs)

and enhanced magnetic perturbations with time scales much longer than those of the electromagnetic EHs. How often and in what circumstances are the electromagnetic EHs associated with BBFs and enhanced magnetic perturbations?

(3) Observations have shown that electromagnetic EHs and DLs are sometimes adjacent to each other. This provokes the question: How are electromagnetic EHs and DLs related?

5.2 The Lunar Wake

In summer 2011, both spacecraft of the ARTEMIS mission were inserted into a lunar orbit. With the comprehensive package of field and plasma instruments aboard, this mission opens a great opportunity to study solar wind interactions with the lunar wake. The following questions can be addressed by a systematic survey of lunar-wake observations.

(1) What kinetic processes are happening during the refilling of solar wind plasmas into the lunar wake? How important are they?

(2) How does the lunar wake interact with solar wind activities? Take solar-wind reconnection for example. It is well known that reconnection outflows propagate at Alfvén speed. Due to the large density gradient, the Alfvén speed changes dramatically in the lunar wake. What can we learn about solar-wind reconnection from that interaction?

The solar wind interaction with the lunar wake is a natural example of plasma expansion into a vacuum or a more tenuous plasma. Therefore, the proposed research not only can further our understanding of this interaction, but also can shed light on other plasma-obstacle interactions, such as those with space vehicle wakes, the Venusian wake, and the wake of Titan.

5.3 Turbulence

In Chapter 4, a framework is sketched to use linear theory to study turbulence in plasmas, namely, to compare spectral behaviors of field component ratios between linear theory and observations. The cold plasma model is explored in Chapter 4 under this framework. In the future, it will be interesting to see the results from a kinetic model (e.g., *Stix* [1992], p.262).

In low frequency range, Chapter 4 shows a consistency between observations and linear theory with field component ratios. However, the frequency range of this work does not cover an extensive range in the MHD regime. Therefore, it will be worthwhile to extend the study further into the MHD regime and see whether such a consistency exists in that regime.

Bibliography

Andersson, L., et al. (2009), New Features of Electron Phase Space Holes Observed by the THEMIS Mission, *Phys. Rev. Lett.*, *102*(22), 225,004, doi: 10.1103/PhysRevLett.102.225004.

Angelopoulos, V. (2008), The THEMIS Mission, *Space Sci. Rev.*, *141*, 5–34, doi: 10.1007/s11214-008-9336-1.

Angelopoulos, V. (2010), The ARTEMIS Mission, *Space Sci. Rev.*, p. 114, doi: 10.1007/s11214-010-9687-2.

Angelopoulos, V., F. S. Mozer, J. Bonnell, M. Temerin, M. Somoza, W. K. Peterson, H. L. Collin, and B. Giles (2001), Wave power studies of cusp crossings with the Polar satellite, *J. Geophys. Res.*, *106*, 5987–6006, doi:10.1029/2000JA900127.

Angelopoulos, V., J. A. Chapman, F. S. Mozer, J. D. Scudder, C. T. Russell, K. Tsuruda, T. Mukai, T. J. Hughes, and K. Yumoto (2002), Plasma sheet electromagnetic power generation and its dissipation along auroral field lines, *J. Geophys. Res.*, *107*, 1181, doi: 10.1029/2001JA900136.

Auster, H. U., et al. (2008), The THEMIS Fluxgate Magnetometer, *Space Sci. Rev.*, *141*, 235–264, doi:10.1007/s11214-008-9365-9.

Bale, S. D. (1997), Shadowed particle distributions near the Moon, *J. Geophys. Res.*, *1021*, 19,773–19,778, doi:10.1029/97JA01676.

Bale, S. D., C. J. Owen, J.-L. Bougeret, K. Goetz, P. J. Kellogg, R. P. Lepping, R. Manning, and S. J. Monson (1997), Evidence of currents and unstable particle distributions in an extended region around the lunar plasma wake, *Geophys. Res. Lett.*, *24*, 1427–1430, doi: 10.1029/97GL01193.

Bale, S. D., P. J. Kellogg, D. E. Larson, R. P. Lin, K. Goetz, and R. P. Lepping (1998), Bipolar electrostatic structures in the shock transition region: Evidence of electron phase space holes, *Geophys. Res. Lett.*, *25*, 2929–2932, doi:10.1029/98GL02111.

Bernstein, I. B., J. M. Greene, and M. D. Kruskal (1957), Exact Nonlinear Plasma Oscillations, *Phys. Rev.*, *108*, 546–550, doi:10.1103/PhysRev.108.546.

Birch, P. C., and S. C. Chapman (2001), Particle-in-cell simulations of the lunar wake with high phase space resolution, *Geophys. Res. Lett.*, *28*, 219–222, doi:10.1029/2000GL011958, (Correction, *Geophys. Res. Lett.*, 28(13), 2669, 2001).

Birch, P. C., and S. C. Chapman (2002), Two dimensional particle-in-cell simulations of the lunar wake, *Phys. Plasmas*, *9*, 1785–1789, doi:10.1063/1.1467655.

Birdsall, C. K., and A. B. Langdon (1985), *Plasma physics via computer simulation*, McGraw-Hill, New York, charles K. Birdsall, A. Bruce Langdon. ill. ; 24 cm. Includes indexes.

Biskamp, D., E. Schwarz, and J. F. Drake (1996), Two-Dimensional Electron Magnetohydrodynamic Turbulence, *Phys. Rev. Lett.*, *76*, 1264–1267, doi:10.1103/PhysRevLett.76.1264.

Bonnell, J. W., F. S. Mozer, G. T. Delory, A. J. Hull, R. E. Ergun, C. M. Cully, V. Angelopoulos, and P. R. Harvey (2008), The Electric Field Instrument (EFI) for THEMIS, *Space Sci. Rev.*, *141*, 303–341, doi:10.1007/s11214-008-9469-2.

Borovsky, J. E., and H. O. Funsten (2003), MHD turbulence in the Earth's plasma sheet: Dynamics, dissipation, and driving, *J. Geophys. Res.*, *108*, 1284, doi:10.1029/2002JA009625.

Borovsky, J. E., R. C. Elphic, H. O. Funsten, and M. F. Thomsen (1997), The Earth's plasma sheet as a laboratory for flow turbulence in high-[beta] MHD, *J. Plasma Phys.*, *57*, 1–34, doi:10.1017/S0022377896005259.

Bosqued, J. M., et al. (1996), Moon-solar wind interaction: First results from the WIND/3DP experiment, *Geophys. Res. Lett.*, *23*, 1259–1262, doi:10.1029/96GL00303.

Cattell, C., J. Wygant, J. Dombeck, F. S. Mozer, M. Temerin, and C. T. Russell (1998), Observations of large amplitude parallel electric field wave packets at the plasma sheet boundary, *Geophys. Res. Lett.*, *25*, 857–860, doi:10.1029/98GL00497.

Cattell, C., J. Crumley, J. Dombeck, J. R. Wygant, and F. S. Mozer (2002), Polar observations of solitary waves at the Earth's magnetopause, *Geophys. Res. Lett.*, *29*(5), 1065, doi:10.1029/2001GL014046.

Cattell, C., C. Neiman, J. Dombeck, J. Crumley, J. Wygant, C. A. Kletzing, W. K. Peterson, F. S. Mozer, and M. André (2003), Large amplitude solitary waves in and near the Earth's magnetosphere, magnetopause and bow shock: Polar and Cluster observations, *Nonlin. Processes Geophys.*, *10*, 13–26.

Cattell, C., et al. (2005), Cluster observations of electron holes in association with magnetotail reconnection and comparison to simulations, *J. Geophys. Res.*, *110*, A01,211, doi:10.1029/2004JA010519.

Cattell, C. A., et al. (1999), Comparisons of Polar satellite observations of solitary wave velocities in the plasma sheet boundary and the high altitude cusp to those in the auroral zone, *Geophys. Res. Lett.*, *26*, 425–428, doi:10.1029/1998GL900304.

Chaston, C. C., C. Salem, J. W. Bonnell, C. W. Carlson, R. E. Ergun, R. J. Strangeway, and J. P. McFadden (2008), The Turbulent Alfvénic Aurora, *Phys. Rev. Lett.*, *100*(17), 175003, doi:10.1103/PhysRevLett.100.175003.

Che, H., J. F. Drake, M. Swisdak, and P. H. Yoon (2010), Electron holes and heating in the reconnection dissipation region, *Geophys. Res. Lett.*, *37*, 11,105, doi:10.1029/2010GL043608.

Chen, L., and G. K. Parks (2002), BGK electron solitary waves in 3D magnetized plasma, *Geophys. Res. Lett.*, *29*(9), 090,000–1, doi:10.1029/2001GL013385.

Cheng, C. Z., and G. Knorr (1976), The integration of the Vlasov equation in configuration space, *J. Comput. Phys.*, *22*, 330–351, doi:10.1016/0021-9991(76)90053-X.

Cully, C. M., R. E. Ergun, K. Stevens, A. Nammari, and J. Westfall (2008), The THEMIS Digital Fields Board, *Space Sci. Rev.*, *141*, 343–355, doi:10.1007/s11214-008-9417-1.

Dai, L., J. R. Wygant, C. Cattell, J. Dombeck, S. Thaller, C. Mouikis, A. Balogh, and H. Rème (2011), Cluster observations of surface waves in the ion jets from magnetotail reconnection, *J. Geophys. Res.*, *116*, A12227, doi:10.1029/2011JA017004.

Deng, X. H., et al. (2006), Observations of electrostatic solitary waves associated with reconnection by Geotail and Cluster, *Adv. Space Res.*, *37*, 1373–1381, doi: 10.1016/j.asr.2005.05.129.

Drake, J. F., M. Swisdak, C. Cattell, M. A. Shay, B. N. Rogers, and A. Zeiler (2003), Formation of Electron Holes and Particle Energization During Magnetic Reconnection, *Science*, *299*, 873–877, doi:10.1126/science.1080333.

Dupree, T. H. (1982), Theory of phase-space density holes, *Phys. Fluids*, *25*, 277–289, doi: 10.1063/1.863734.

Ergun, R. E., E. Klementis, C. W. Carlson, J. P. McFadden, and J. H. Clemmons (1991), Wavelength measurement of auroral hiss, *J. Geophys. Res.*, *96*, 21,299–+, doi: 10.1029/91JA01863.

Ergun, R. E., et al. (1998a), FAST satellite observations of large-amplitude solitary structures, *Geophys. Res. Lett.*, *25*, 2041–2044, doi:10.1029/98GL00636.

Ergun, R. E., C. W. Carlson, J. P. McFadden, F. S. Mozer, L. Muschietti, I. Roth, and R. J. Strangeway (1998b), Debye-Scale Plasma Structures Associated with Magnetic-Field-Aligned Electric Fields, *Phys. Rev. Lett.*, *81*, 826–829, doi:10.1103/PhysRevLett.81.826.

Ergun, R. E., Y.-J. Su, L. Andersson, C. W. Carlson, J. P. McFadden, F. S. Mozer, D. L. Newman, M. V. Goldman, and R. J. Strangeway (2001), Direct Observation of Localized Parallel Electric Fields in a Space Plasma, *Phys. Rev. Lett.*, *87*(4), 045,003–+, doi: 10.1103/PhysRevLett.87.045003.

Ergun, R. E., et al. (2009), Observations of Double Layers in Earth's Plasma Sheet, *Phys. Rev. Lett.*, *102*(15), 155,002, doi:10.1103/PhysRevLett.102.155002.

Farrell, W. M., R. J. Fitzenreiter, C. J. Owen, J. B. Byrnes, R. P. Lepping, K. W. Ogilvie, and F. Neubauer (1996), Upstream ULF waves and energetic electrons associated with the lunar wake: Detection of precursor activity, *Geophys. Res. Lett.*, *23*, 1271–1274, doi: 10.1029/96GL01355.

Farrell, W. M., M. L. Kaiser, J. T. Steinberg, and S. D. Bale (1998), A simple simulation of a plasma void: Applications to Wind observations of the lunar wake, *J. Geophys. Res.*, *103*, 23,653–23,660, doi:10.1029/97JA03717.

Feldman, W. C., J. R. Asbridge, S. J. Bame, M. D. Montgomery, and S. P. Gary (1975), Solar wind electrons, *J. Geophys. Res.*, *80*, 4181–4196, doi:10.1029/JA080i031p04181.

Fitzenreiter, R. J., K. W. Ogilvie, D. J. Chornay, and J. Keller (1998), Observations of electron velocity distribution functions in the solar wind by the WIND spacecraft: High angular resolution strahl measurements, *Geophys. Res. Lett.*, *25*, 249–252, doi: 10.1029/97GL03703.

Fox, W., M. Porkolab, J. Egedal, N. Katz, and A. Le (2008), Laboratory Observation of Electron Phase-Space Holes during Magnetic Reconnection, *Phys. Rev. Lett.*, *101*(25), 255,003, doi:10.1103/PhysRevLett.101.255003.

Franz, J. R., P. M. Kintner, and J. S. Pickett (1998), POLAR observations of coherent electric field structures, *Geophys. Res. Lett.*, *25*, 1277–1280, doi:10.1029/98GL50870.

Franz, J. R., P. M. Kintner, J. S. Pickett, and L.-J. Chen (2005), Properties of small-amplitude electron phase-space holes observed by Polar, *J. Geophys. Res.*, *110*, A09,212, doi:10.1029/2005JA011095.

Frisch, U. (1995), *Turbulence: The legacy of A. N. Kolmogorov.*

Galtier, S., and E. Buchlin (2007), Multiscale Hall-Magnetohydrodynamic Turbulence in the Solar Wind, *Astrophys. J.*, *656*, 560–566, doi:10.1086/510423.

Gary, S. P. (1985), Electrostatic instabilities in plasmas with two electron components, *J. Geophys. Res.*, *90*, 8213–8221.

Gary, S. P., and R. L. Tokar (1985), The electron-acoustic mode, *Phys. Fluids*, *28*, 2439–2441, doi:10.1063/1.865250.

Goldman, M. V., D. L. Newman, and P. Pritchett (2008), Vlasov simulations of electron holes driven by particle distributions from PIC reconnection simulations with a guide field, *Geophys. Res. Lett.*, *35*, 22,109, doi:10.1029/2008GL035608.

Gurnett, D. A., and L. A. Frank (1977), A region of intense plasma wave turbulence on auroral field lines, *J. Geophys. Res.*, *82*, 1031–1050, doi:10.1029/JA082i007p01031.

Gurnett, D. A., and L. A. Frank (1978), Plasma waves in the polar cusp - Observations from Hawkeye 1, *J. Geophys. Res.*, *83*, 1447–1462, doi:10.1029/JA083iA04p01447.

Gurnett, D. A., L. A. Frank, and R. P. Lepping (1976), Plasma waves in the distant magnetotail, *J. Geophys. Res.*, *81*, 6059–6071, doi:10.1029/JA081i034p06059.

Halekas, J. S., et al. (2011), First Results from ARTEMIS, a New Two-Spacecraft Lunar Mission: Counter-Streaming Plasma Populations in the Lunar Wake, *Space Sci. Rev.*, pp. 8–+, doi:10.1007/s11214-010-9738-8.

Hashimoto, K., et al. (2010), Electrostatic solitary waves associated with magnetic anomalies and wake boundary of the Moon observed by KAGUYA, *Geophys. Res. Lett.*, *37*, 19,204, doi:10.1029/2010GL044529.

Hau, L., and W. Fu (2007), Mathematical and physical aspects of Kappa velocity distribution, *Phys. Plasmas*, *14*(11), 110,702, doi:10.1063/1.2779283.

Hoshino, M., A. Nishida, T. Yamamoto, and S. Kokubun (1994), Turbulent magnetic field in the distant magnetotail: Bottom-up process of plasmoid formation?, *Geophys. Res. Lett.*, *21*, 2935–2938, doi:10.1029/94GL02094.

Huttunen, K. E. J., S. D. Bale, T. D. Phan, M. Davis, and J. T. Gosling (2007), Wind/WAVES observations of high-frequency plasma waves in solar wind reconnection exhausts, *J. Geophys. Res.*, *112*, 1102, doi:10.1029/2006JA011836.

Iroshnikov, P. S. (1964), Turbulence of a Conducting Fluid in a Strong Magnetic Field, *Sov. Astron.*, *7*, 566.

Jackson, J. D. (1998), *Classical Electrodynamics*, 3rd ed., Wiley, New York, NY.

Johnson, F. S., and J. E. Midgley (1968), Notes on the Lunar Magnetosphere, *J. Geophys. Res.*, *73*, 1523–+, doi:10.1029/JA073i005p01523.

Kallio, E. (2005), Formation of the lunar wake in quasi-neutral hybrid model, *Geophys. Res. Lett.*, *32*, 6107–+, doi:10.1029/2004GL021989.

Kelley, M. C., D. J. Knudsen, and J. F. Vickrey (1991), Poynting flux measurements on a satellite - A diagnostic tool for space research, *J. Geophys. Res.*, *96*, 201–207, doi:10.1029/90JA01837.

Kellogg, P. J., K. Goetz, S. J. Monson, J. Bougeret, R. Manning, and M. L. Kaiser (1996), Observations of plasma waves during a traversal of the moon's wake, *Geophys. Res. Lett.*, *23*, 1267–1270, doi:10.1029/96GL00376.

Khotyaintsev, Y. V., A. Vaivads, M. André, M. Fujimoto, A. Retinò, and C. J. Owen (2010), Observations of Slow Electron Holes at a Magnetic Reconnection Site, *Phys. Rev. Lett.*, *105*(16), 165,002, doi:10.1103/PhysRevLett.105.165002.

Kojima, H., H. Matsumoto, S. Chikuba, S. Horiyama, M. Ashour-Abdalla, and R. R. Anderson (1997), Geotail waveform observations of broadband/narrowband electrostatic noise in the distant tail, *J. Geophys. Res.*, *102*, 14,439–14,456, doi:10.1029/97JA00684.

Kolmogorov, A. (1941), The Local Structure of Turbulence in Incompressible Viscous Fluid for Very Large Reynolds' Numbers, *Dokl. Akad. Nauk SSSR*, *30*, 301–305.

Kraichnan, R. H. (1965), Inertial-Range Spectrum of Hydromagnetic Turbulence, *Phys. Fluids*, *8*, 1385–1387, doi:10.1063/1.1761412.

Krishan, V., and S. M. Mahajan (2004), Magnetic fluctuations and Hall magneto-hydrodynamic turbulence in the solar wind, *J. Geophys. Res.*, *109*, A11105, doi: 10.1029/2004JA010496.

Labelle, J., and P. M. Kintner (1989), The measurement of wavelength in space plasmas, *Rev. Geophys.*, *27*, 495–518, doi:10.1029/RG027i004p00495.

Lefebvre, B., L. Chen, W. Gekelman, P. Kintner, J. Pickett, P. Pribyl, S. Vincena, F. Chiang, and J. Judy (2010), Laboratory Measurements of Electrostatic Solitary Structures Generated by Beam Injection, *Phys. Rev. Lett.*, *105*(11), 115,001–+, doi: 10.1103/PhysRevLett.105.115001.

Louarn, P., et al. (2009), On the Temporal Variability of the "Strahl" and Its Relationship with Solar Wind Characteristics: STEREO SWEA Observations, *Solar Phys.*, *259*, 311–321, doi:10.1007/s11207-009-9402-1.

Lu, Q. M., B. Lembege, J. B. Tao, and S. Wang (2008), Perpendicular electric field in two-dimensional electron phase-holes: A parameter study, *J. Geophys. Res.*, *113*, A11,219, doi:10.1029/2008JA013693.

Lynov, J. P., P. Michelsen, H. L. Pecseli, J. Juul Rasmussen, K. Saeki, and V. A. Turikov (1979), Observations of solitary structures in a magnetized, plasma loaded waveguide, *Phys. Scr.*, *20*, 328–335, doi:10.1088/0031-8949/20/3-4/005.

Mangeney, A., et al. (1999), WIND observations of coherent electrostatic waves in the solar wind., *Ann. Geophys.*, *17*, 307–320.

Matsumoto, H., H. Kojima, T. Miyatake, Y. Omura, M. Okada, I. Nagano, and M. Tsutsui (1994), Electrotastic Solitary Waves (ESW) in the magnetotail: BEN wave forms observed by GEOTAIL, *Geophys. Res. Lett.*, *21*, 2915–2918, doi:10.1029/94GL01284.

McFadden, J. P., C. W. Carlson, D. Larson, M. Ludlam, R. Abiad, B. Elliott, P. Turin, M. Marckwordt, and V. Angelopoulos (2008), The THEMIS ESA Plasma Instrument and In-flight Calibration, *Space Sci. Rev.*, *141*, 277–302, doi:10.1007/s11214-008-9440-2.

Morse, R. L., and C. W. Nielson (1969), One-, Two-, and Three-Dimensional Numerical Simulation of Two-Beam Plasmas, *Phys. Rev. Lett.*, *23*, 1087–1090, doi: 10.1103/PhysRevLett.23.1087.

Mozer, F. S., R. Ergun, M. Temerin, C. Cattell, J. Dombeck, and J. Wygant (1997), New features of time domain electric-field structures in the auroral acceleration region., *Phys. Rev. Lett.*, *79*, 1281–1284, doi:10.1103/PhysRevLett.79.1281.

Muschietti, L., I. Roth, C. W. Carlson, and R. E. Ergun (2000), Transverse Instability of Magnetized Electron Holes, *Phys. Rev. Lett.*, *85*, 94–97, doi:10.1103/PhysRevLett.85.94.

Nakagawa, T., Y. Takahashi, and M. Iizima (2003), GEOTAIL observation of upstream ULF waves associated with lunar wake, *Earth Planets Space*, *55*, 569–580.

Ness, N. F. (1972), Interaction of the solar wind with the moon., in *The Interplanetary Medium: Part II of Solar-Terrestrial Physics/1970*, pp. 159–205.

Ness, N. F., K. W. Behannon, C. S. Scearce, and S. C. Cantarano (1967), Early Results from the Magnetic Field Experiment on Lunar Explorer 35, *J. Geophys. Res.*, *72*, 5769, doi:10.1029/JZ072i023p05769.

Newman, D. L., L. Andersson, M. V. Goldman, R. E. Ergun, and N. Sen (2008), Influence of suprathermal background electrons on strong auroral double layers: Vlasov-simulation parameter study, *Phys. Plasmas*, *15*(7), 072,902, doi:10.1063/1.2938753.

Ogilvie, K. W., J. T. Steinberg, R. J. Fitzenreiter, C. J. Owen, A. J. Lazarus, W. M. Farrell, and R. B. Torbert (1996), Observations of the lunar plasma wake from the WIND spacecraft on December 27, 1994, *Geophys. Res. Lett.*, *23*, 1255–1258, doi:10.1029/96GL01069.

Omura, Y., H. Matsumoto, T. Miyake, and H. Kojima (1996), Electron beam instabilities as generation mechanism of electrostatic solitary waves in the magnetotail, *J. Geophys. Res.*, *101*(A2), 2685–2697, doi:10.1029/95JA03145.

Onsager, T. G., and R. H. Holzworth (1990), Measurement of the electron beam mode in earth's foreshock, *J. Geophys. Res.*, *95*, 4175–4186, doi:10.1029/JA095iA04p04175.

Onsager, T. G., R. H. Holzworth, H. C. Koons, O. H. Bauer, and D. A. Gurnett (1989), High-frequency electrostatic waves near earth's bow shock, *J. Geophys. Res.*, *94*, 13,397–13,408, doi:10.1029/JA094iA10p13397.

Owen, C. J., R. P. Lepping, K. W. Ogilvie, J. A. Slavin, W. M. Farrell, and J. B. Byrnes (1996), The lunar wake at 6.8 R_L: WIND magnetic field observations, *Geophys. Res. Lett.*, *23*, 1263–1266, doi:10.1029/96GL01354.

Pedersen, A., F. Mozer, and G. Gustafsson (1998), Electric Field Measurements in a Tenuous Plasma with Spherical Double Probes, in *Measurement Techniques in Space Plasmas – Fields*, edited by R. F. Pfaff, J. E. Borovsky, & D. T. Young, p. 1.

Penrose, O. (1960), Electrostatic Instabilities of a Uniform Non-Maxwellian Plasma, *Phys. Fluids*, *3*, 258–265, doi:10.1063/1.1706024.

Peredo, M., J. A. Slavin, E. Mazur, and S. A. Curtis (1995), Three-dimensional position and shape of the bow shock and their variation with Alfvenic, sonic and magnetosonic Mach numbers and interplanetary magnetic field orientation, *J. Geophys. Res.*, *100*, 7907–7916, doi:10.1029/94JA02545.

Pickett, J., L. Chen, S. Kahler, O. Santolík, D. Gurnett, B. Tsurutani, and A. Balogh (2004), Isolated electrostatic structures observed throughout the Cluster orbit: relationship to magnetic field strength, *Ann. Geophys.*, *22*, 2515–2523, doi:10.5194/angeo-22-2515-2004.

Pickett, J. S., et al. (2009), Electrostatic solitary waves in current layers: from Cluster observations during a super-substorm to beam experiments at the LAPD, *Nonlin. Processes Geophys.*, *16*, 431–442.

Pierrard, V., and M. Lazar (2010), Kappa distributions: theory and applications in space plasmas, *ArXiv e-prints*.

Retinò, A., et al. (2006), Structure of the separatrix region close to a magnetic reconnection X-line: Cluster observations, *Geophys. Res. Lett.*, *33*, 6101, doi:10.1029/2005GL024650.

Reynolds, O. (1883), An experimental investigation of the circumstances which determine whether the motion of water in parallel channels shall be direct or sinuous and of the law of resistance in parallel channels., *Philos. Trans. R. Soc.*, *174*, 935–982.

Richardson, L. F. (2007), *Weather Prediction by Numerical Process*, 2nd ed., Cambridge University Press, New York, 1st edition published in 1922.

Roberts, K. V., and H. L. Berk (1967), Nonlinear Evolution of a Two-Stream Instability, *Phys. Rev. Lett.*, *19*, 297–300, doi:10.1103/PhysRevLett.19.297.

Rott, N. (1990), Note on the history of the reynolds number, *Ann. Rev. Fluid Mech.*, *22*, 1–11, doi:10.1146/annurev.fl.22.010190.000245.

Roux, A., O. Le Contel, C. Coillot, A. Bouabdellah, B. de La Porte, D. Alison, S. Ruocco, and M. C. Vassal (2008), The Search Coil Magnetometer for THEMIS, *Space Sci. Rev.*, *141*, 265–275, doi:10.1007/s11214-008-9455-8.

Saeki, K., P. Michelsen, H. L. Pécseli, and J. J. Rasmussen (1979), Formation and Coalescence of Electron Solitary Holes, *Phys. Rev. Lett.*, *42*, 501–504, doi:10.1103/PhysRevLett.42.501.

Samir, U., K. H. Wright, Jr., and N. H. Stone (1983), The expansion of a plasma into a vacuum: basic phenomena and processes and applications to space plasma physics., *Rev. Geophys. Space Phys.*, *21*, 1631–1646.

Santolík, O., D. A. Gurnett, J. S. Pickett, M. Parrot, and N. Cornilleau-Wehrlin (2003), Spatio-temporal structure of storm-time chorus, *J. Geophys. Res.*, *108*, 1278, doi:10.1029/2002JA009791.

Schamel, H. (1979), Theory of electron holes, *Phys. Scr.*, *20*, 336–342, doi:10.1088/0031-8949/20/3-4/006.

Schamel, H. (1986), Electron holes, ion holes and double layers Electrostatic phase space structures in theory and experiment, *Phys. Rep.*, *140*, 161–191, doi:10.1016/0370-1573(86)90043-8.

Schubert, G., and B. R. Lichtenstein (1974), Observations of moon-plasma interactions by orbital and surface experiments, *Rev. Geophys. Space Phys.*, *12*, 592–626.

Shiokawa, K., W. Baumjohann, and G. Haerendel (1997), Braking of high-speed flows in the near-Earth tail, *Geophys. Res. Lett.*, *24*, 1179–1182, doi:10.1029/97GL01062.

Shue, J., J. K. Chao, H. C. Fu, C. T. Russell, P. Song, K. K. Khurana, and H. J. Singer (1997), A new functional form to study the solar wind control of the magnetopause size and shape, *J. Geophys. Res.*, *102*, 9497–9512, doi:10.1029/97JA00196.

Singh, N. (2000), Electron holes as a common feature of double-layer-driven plasma waves, *Geophys. Res. Lett.*, *27*, 927–930, doi:10.1029/1999GL003709.

Singh, N., S. M. Loo, B. E. Wells, and C. Deverapalli (2000), Three-dimensional structure of electron holes driven by an electron beam, *Geophys. Res. Lett.*, *27*, 2469–2472, doi:10.1029/2000GL003766.

Singh, N., S. Araveti, and E. B. Wells (2011), Mesoscale PIC simulation of double layers and electron holes affecting parallel and transverse accelerations of electrons and ions, *J. Geophys. Res.*, *116*, A00K09, doi:10.1029/2010JA016323.

Stix, T. H. (1992), *Waves in Plasmas*, American Institute of Physics, New York.

Summers, D., and R. M. Thorne (1991), The modified plasma dispersion function, *Phys. Fluids B*, *3*, 1835–1847, doi:10.1063/1.859653.

Taylor, H. E. (1968), Aspect determination in lunar shadow on Explorer 35, *NASA-TN, D-4544*.

Turikov, V. A. (1984), Electron phase space holes as localized BGK solutions, *Phys. Scr.*, *30*, 73, doi:10.1088/0031-8949/30/1/015.

Umeda, T., Y. Omura, and H. Matsumoto (2004), Two-dimensional particle simulation of electromagnetic field signature associated with electrostatic solitary waves, *J. Geophys. Res.*, *109*, A02,207, doi:10.1029/2003JA010000.

Umeda, T., Y. Omura, T. Miyake, H. Matsumoto, and M. Ashour-Abdalla (2006), Nonlinear evolution of the electron two-stream instability: Two-dimensional particle simulations, *J. Geophys. Res.*, *111*, A10,206, doi:10.1029/2006JA011762.

Weygand, J. M., et al. (2005), Plasma sheet turbulence observed by Cluster II, *J. Geophys. Res.*, *110*, A01,205, doi:10.1029/2004JA010581.

Wiehle, S., et al. (2011), First lunar wake passage of ARTEMIS: Discrimination of wake effects and solar wind fluctuations by 3D hybrid simulations, *Planet. Space Sci.*, *59*, 661–671, doi:10.1016/j.pss.2011.01.012.

Appendix A

The THEMIS mission and the ARTEMIS mission

The THEMIS mission [*Angelopoulos*, 2008] initially consisted of five identical, spinning spacecraft in terrestial orbits with various apogees. In late 2009, the two outmost spacecraft were directed to lunar orbits and formed the ARTEMIS mission [*Angelopoulos*, 2010]. In terms of instrumentation, the two missions are identical.

Each of the THEMIS/ARTEMIS spacecraft carries a comprehensive package of field and plasma instruments, including an electric field instrument (EFI) [*Bonnell et al.*, 2008], fluxgate magnetometer (FGM) [*Auster et al.*, 2008], search coil magnetometer (SCM) [*Roux et al.*, 2008], electrostatic analyzer (ESA) [*McFadden et al.*, 2008], and solid state telescope (SST). Figure A.1 shows a schematic diagram of the spacecraft with all the instruments labelled.

A.1 The Orbits of THEMIS Spacecraft

The orbits of the five THEMIS spacecraft are highly elliptical and roughly in the ecliptic plane around the Earth. Table A.1 lists main orbit parameters of the five spacecraft, where the apogees and perigees are in units of Earth radii (R_E). As shown in Table A.1, THEMIS spacecraft can be referred to by a letter or by a number. For instance, THEMIS A can also be referred as THEMIS probe 5 (P5). Due to the apogee difference, THEMIS A, D, and E are known as inner probes, whereas THEMIS C and B are known as outer probes. The five spacecraft line up at apogee approximately every four days. The apogees slowly rotate

around the Earth so that the orbits can cover nightside, duskside, dayside, and dawnside of the Earth's magnetosphere. Figure A.2 illustrates the THEMIS constellation configuration in the nightside. Figure A.3 shows example orbits of THEMIS spacecraft in different regions of the magnetosphere.

Table A.1: Orbit parameters of THEMIS spacecraft

Spacecraft	Apogee [R_E]	Perigee [R_E]
THEMIS A (P5)	10	1.5
THEMIS E (P4)	12	1.5
THEMIS D (P3)	12	1.5
THEMIS C (P2)	20	1.2
THEMIS B (P1)	30	1.3

A.2 The Orbits of ARTEMIS Spacecraft

The THEMIS B and C spacecraft were directed to the Moon after the prime phase of THEMIS was successfully completed in September 2009. The maneuver primarily took place in the equatorial plane. There are four main phases of ARTEMIS orbits:

- Translunar injections (TLI): Roughly from October 2009 to October 2010. The first lunar wake flyby of ARTEMIS P1 occurred during this phase.
- P1(P2) at LL2(LL1): Roughly from October 2010 to January 2011. After TLI, the ARTEMIS spacecraft entered Lissajous orbits around the Lagrange points of the Earth-Moon system, where the Earth side point is labelled Lunar Lagrange point 1 (LL1) and the opposite one labelled LL2. Example orbits of this phase are shown in Figure A.4(a).
- P1 and P2 both at LL1: Roughly from January 2011 to April 2011. Example orbits of this phase are shown in Figure A.4(b).

- In lunar orbit: Roughly from April 2011 to September 2012. Both ARTEMIS spacecraft are placed in stable equatorial, high-eccentricity orbits, of $\sim$100 km $\times$ $\sim$11 R_L altitude. Example orbits of this phase are shown in Figure A.5.

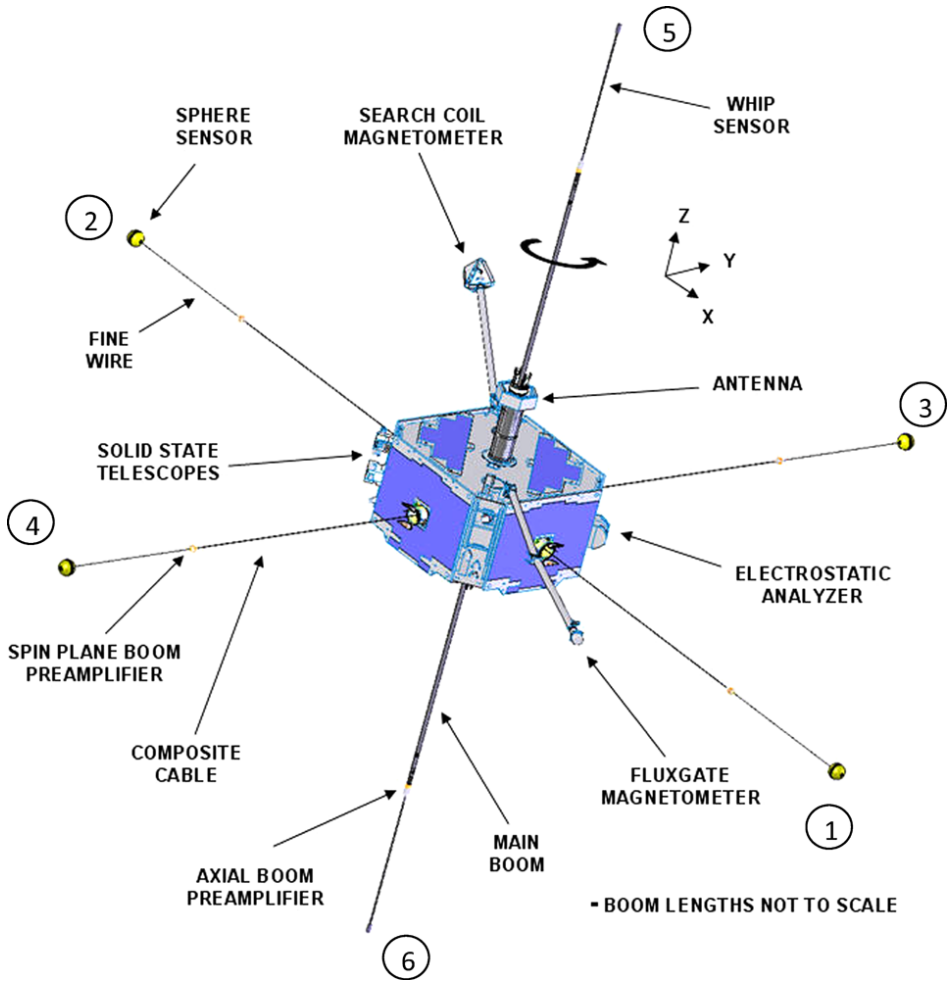

Figure A.1: Schematic diagram of THEMIS spacecraft. The six circled numbers label the six EFI sensors. The x-y plane represents the spin plane of the spacecraft. (After *Bonnell et al.* [2008].)

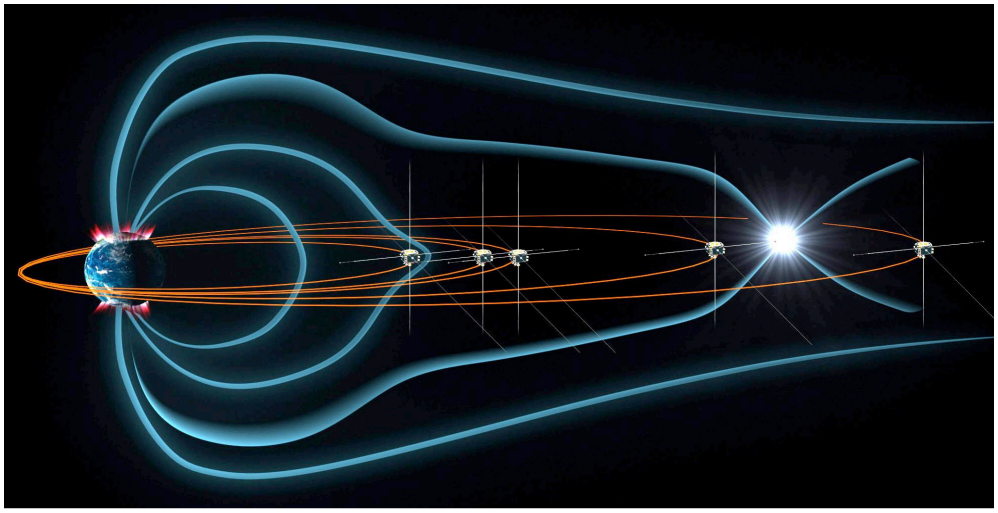

Figure A.2: An artistic illustration of the THEMIS constellation configuration in the nightside.

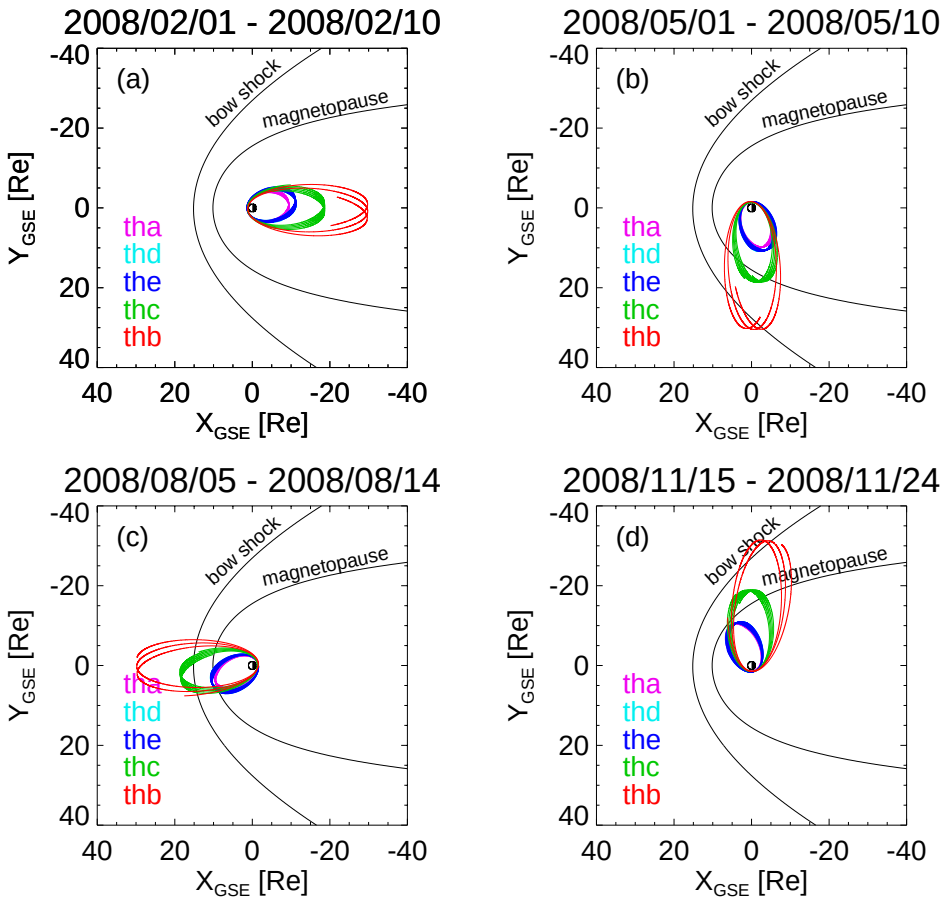

Figure A.3: Example orbits in GSE x-y plane of THEMIS spacecraft in the (a) night side, (b) dusk side, (c) day side, and (d) dawn side. The dates of the orbits are labelled in the title of each panel. The locations of the bow shock and the magnetopause are based on *Peredo et al.* [1995] and *Shue et al.* [1997], respectively.

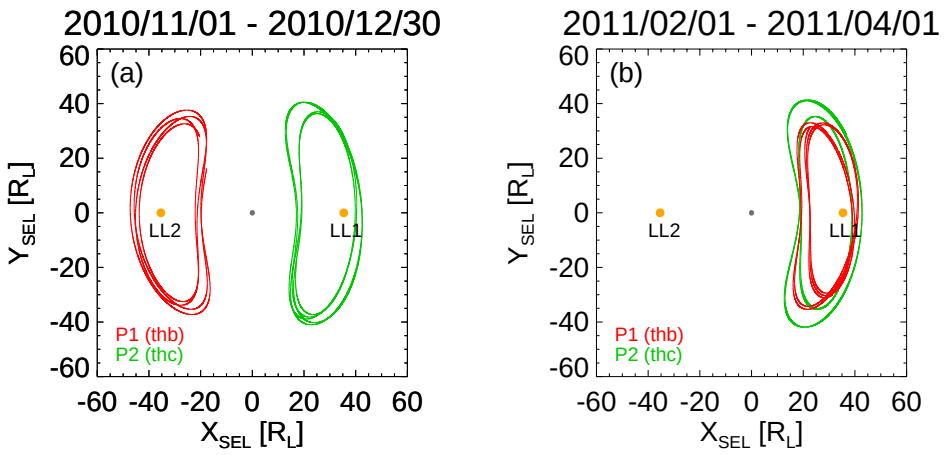

Figure A.4: Example Lissajous orbits in SEL x-y plane of ARTEMIS spacecraft. The SEL coordinate system is defined such that the origin is at the center of the Moon, x axis pointing to the Earth, z axis pointing northward normal to the orbit plane of the Moon, and y axis completing the right-handed system. The dates of the orbits are labelled in the title of each panel. The approximate locations of LL1 and LL2 are indicated by orange filled circles.

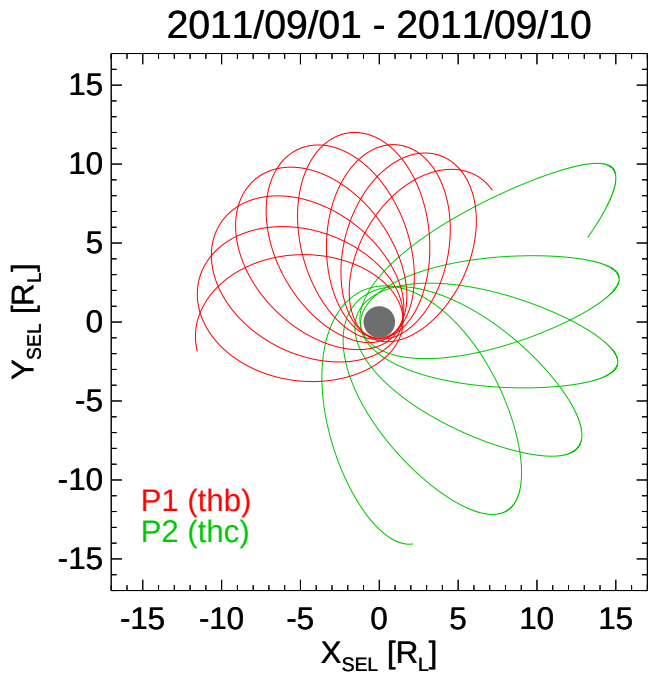

Figure A.5: Example lunar orbits in SEL x-y plane of ARTEMIS spacecraft. The format is similar to that in Figure A.4.

Appendix B

On Correcting THEMIS/ARTEMIS Vector Field Data for Eclipse Crossings

B.1 Introduction

Accurate spin rate and spin phase are required to de-spin vector field data, such as magnetic field and flow velocity, of a spinning spacecraft. A common technique for determining the spin rate and the spin phase is to use the Sun as a reference, which is the case for THEMIS/ARTEMIS. However, when the spacecraft is in an eclipse, the spacecraft loses that spin reference. Even worse, the spacecraft is cooling due to thermal radiation in the eclipse and its moment of inertia decreases due to thermal contraction. The spin rate of the spacecraft thus increases because of the conservation of the angular momentum of the spacecraft. Because no spin reference is available, an empirical spin rate is assumed during an eclipse crossing, which is not generally accurate. Therefore, the de-spun vector field data from the empirical spin rate are not accurate and must be corrected. This appendix provides a method for that correction.

The method consists of three main steps. First, determine the time of an eclipse crossing of the spacecraft. Second, correct the spin rate and spin phase of the spacecraft. Third, correct vector field data using the corrected spin phase.

B.2 Determining Eclipse Time

To determine the time of an eclipse accurately, one needs the position of the spacecraft, the position of the celestial body that causes the eclipse, and the position of the Sun. For

THEMIS/ARTEMIS, one can use the routine `thm_load_slp` from the themis data analysis software (TDAS) to get the position information of the Moon and the Sun. Once all the position information is ready, determining the eclipse time is a simple geometry problem and the details are omitted in this appendix.

B.3 Correcting Spin Rate and Spin Phase

The time-dependent behavior of the spin rate and the spin period of a spacecraft in an eclipse is illustrated in Figure B.1.

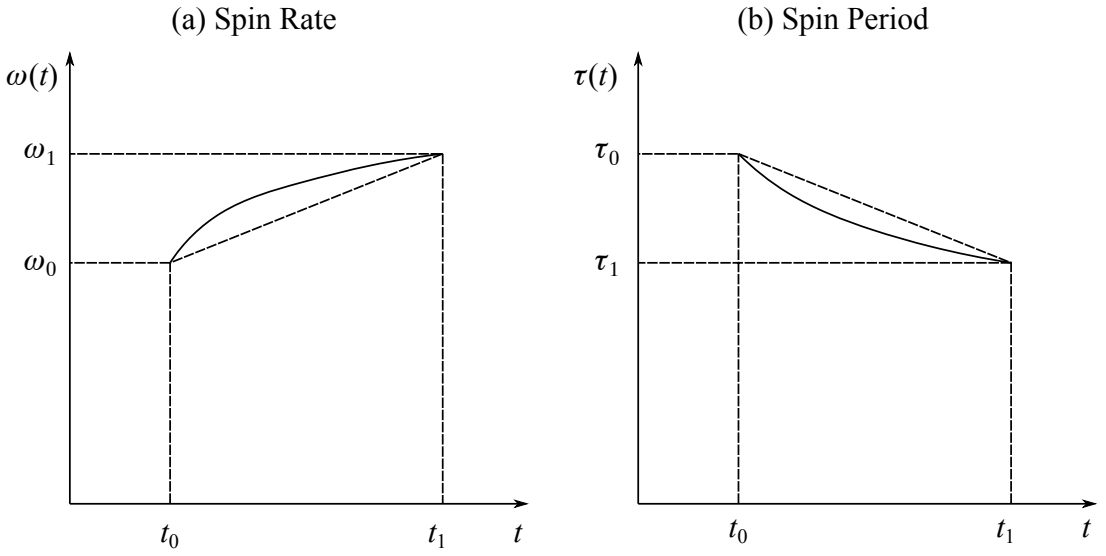

Figure B.1: An illustration of the time-dependent behavior of the (a) spin rate ($\omega(t)$) and (b) spin period ($\tau(t)$) of a spacecraft in an eclipse, where t_0 and t_1 are the starting and ending times of the eclipse respectively.

Although the cumulative error of spin phase is generally significant in shadow crossing, the net change of the spin rate is generally small (less than 1% based on available lunar shadow crossing as of April 11, 2012). In this method, the time-dependent relation of the spin rate in an eclipse is approximated with a Taylor expansion as

$$\omega(t) = \omega_0 + b(t - t_0) + a(t - t_0)^2, \tag{B.1}$$

where the Taylor expansion is truncated at the second order, $\omega(t)$ is the time-dependent spin period in the eclipse, t_0 is the starting time of the eclipse, ω_0 is the spin rate at t_0, and a and b are two parameters to be determined. Using the spin rate at the end of the shadow, one has

$$b = \frac{\omega_1 - \omega_0 - aT^2}{T}, \tag{B.2}$$

where $T = t_1 - t_0$ is the length of the eclipse, t_1 is the ending time of the eclipse, and ω_1 is the spin rate at t_1.

Because the spin rate should be increasing in an eclipse, one constraint on $\omega(t)$ is that

$$\frac{d\omega}{dt} > 0. \tag{B.3}$$

Moreover, the rate of the spin-rate increase should be decreasing in an eclipse because the spacecraft temperature drops faster in the early stage of the eclipse than in the late stage. Therefore, another constraint on $\omega(t)$ is that

$$\frac{d^2\omega}{dt^2} < 0. \tag{B.4}$$

These two constraints lead to

$$-\frac{\omega_1 - \omega_0}{T^2} < a < 0. \tag{B.5}$$

Therefore, to fully determine the time-dependent relation of $\omega(t)$, one needs to find an optimal a in the range of $[(\omega_0 - \omega_1)/T^2, 0]$.

The spin phase is an integration of the spin rate based on the following relation

$$\phi(t) = \phi(t'_0) + \int_{t'_0}^{t} \omega(t')dt'. \tag{B.6}$$

One measure of the optimization of a is to measure the spin phase difference between the modelled spin phase based on Equations (B.1) and (B.6) and the measured spin phase in a certain interval after the eclipse, for instance, one hour after the eclipse. The goal is to find a value of a that minimizes that phase difference. An example algorithm for finding an optimal a is illustrated in Figure B.2.

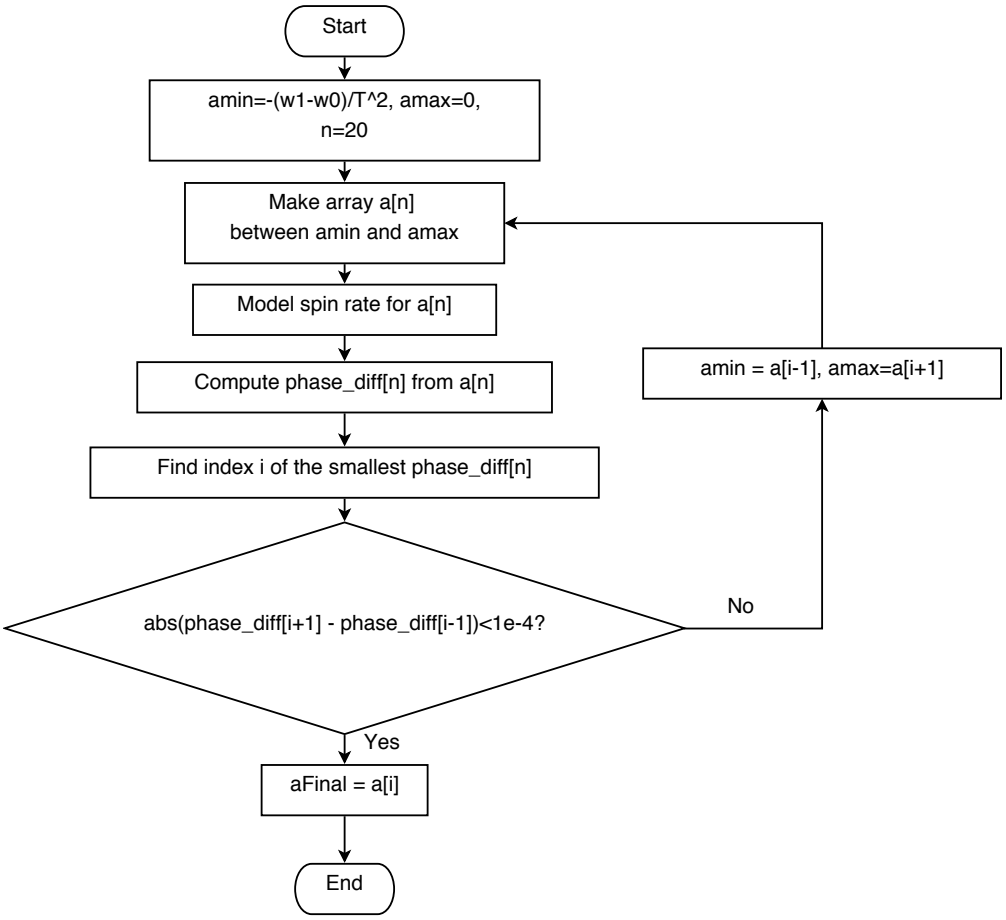

Figure B.2: An algorithm for finding an optimal value of a for spin rate correction.

B.3.1 2π ambiguity issue of spin phase

Suppose the true spin phase is ϕ_1 at t_1, a_0 is the optimal a for the true time-dependent relation of the spin rate in an eclipse, and $a_0 + \Delta a$ is a value of a that results in a spin phase $\phi_1 + 2n\pi$ at t_1 where n is an integer. Then it is impossible to tell which one models the true time-dependent relation of the spin rate between a_0 and $a_0 + \Delta a$ based on the difference between the modelled and measured spin phases after the shadow because the spin phase is measured between 0 and 360 in degrees. One has to use extra information to determine that.

However, this issue only occurs when the eclipse is too long. Suppose the effective average spin rate is ω', which satisfies $\omega' T = \phi_1 - \phi_0$, where ϕ_0 is the spin phase at t_0. As

shown Figure B.1(a), $\omega' > (\omega_0 + \omega_1)/2$. Suppose $N_1 = \frac{T\omega_1}{2\pi}$, and $N_2 = \frac{T(\omega_0+\omega_1)}{4\pi}$, and N is the number of spins of the spacecraft in the shadow, then

$$N_2 < N < N_1. \tag{B.7}$$

For any model of $\omega(t)$, if $N_1 - N_2 < 1$, the 2π ambiguity issue is resolved. Substituting the expressions of N_1 and N_2 into $N_1 - N_2 < 1$, and using the relation $\omega = 2\pi/\tau$, one obtains

$$T < \frac{2\tau_0\tau_1}{\tau_0 - \tau_1}, \tag{B.8}$$

where τ_0 and τ_1 are the spin period at t_0 and t_1 respectively. For THEMIS/ARTEMIS, $\tau_0 - \tau_1 \lesssim 0.01$ s, and τ_0, $\tau_1 \approx 3.52$ s. Therefore, $\frac{2\tau_0\tau_1}{\tau_0-\tau_1} \approx 41$ min. In other words, if the shadow duration is less than 41 minutes, no 2π ambiguity of spin phase exists for any model of $\omega(t)$.

The model of $\omega(t)$ as shown in Equation (B.1) has a better performance in terms of resolving the 2π ambiguity issue than the general results shown above. By solving the equation

$$\int_{t_0}^{t_1} \omega(t; a_0 + \Delta a)dt - \int_{t_0}^{t_1} \omega(t; a_0)dt = 2n\pi, \tag{B.9}$$

one has

$$\Delta a = \frac{6n\pi}{T^3}. \tag{B.10}$$

Because the value of a is bounded as shown in Equation (B.5), no 2π ambiguity of spin phase translates to $\Delta a(n = 1) > \frac{\omega_1-\omega_0}{T^2}$, or

$$T < \frac{3\tau_0\tau_1}{\tau_0 - \tau_1}, \tag{B.11}$$

which indicates that no 2π ambiguity issue exists for a shadow crossing less than 62 minutes. This condition is better than the general one shown in Equation (B.8) because it allows longer shadow crossings to avoid the 2π amiguity of spin phase.

B.4 Correcting Vector Fields

Vector fields must be in a de-spun coordinate system to be useful for scientific purposes. Once the spin period and spin phases are corrected in the shadow, correcting de-spun vector fields is simply a problem of vector rotation. For THEMIS/ARTEMIS, one spinning coordinate system is the spinning sun-sensor L-vector (SSL) coordinate system, and one de-spun coordinate system is the de-spun, sun-pointing, L-vector (DSL) coordinate system. The L-vector stands for the angular momentum vector of the spin. The Z axis of DSL is identical to that of SSL and is along L-vector. The rotation from SSL to DSL is

$$X_{DSL} = X_{SSL}\cos\phi - Y_{SSL}\sin\phi \tag{B.12}$$

$$Y_{DSL} = X_{SSL}\sin\phi + Y_{SSL}\cos\phi \tag{B.13}$$

where ϕ is the spin phase. And the inverse rotation is

$$X_{SSL} = X_{DSL}\cos\phi + Y_{DSL}\sin\phi \tag{B.14}$$

$$Y_{SSL} = -X_{DSL}\sin\phi + Y_{DSL}\cos\phi. \tag{B.15}$$

If the SSL data are available, one can use the corrected spin phase and the SSL data to get the corrected DSL data with Equations (B.12) and (B.13). Another approach is to correct the DSL data directly. Suppose X'_{DSL}, Y'_{DSL}, and ϕ' are non-corrected data, and X_{DSL}, Y_{DSL}, and ϕ are corrected data. Then, one has

$$X_{DSL}\cos\phi + Y_{DSL}\sin\phi = X'_{DSL}\cos\phi' + Y'_{DSL}\sin\phi' \tag{B.16}$$

$$-X_{DSL}\sin\phi + Y_{DSL}\cos\phi = -X'_{DSL}\sin\phi' + Y'_{DSL}\cos\phi', \tag{B.17}$$

or

$$X_{DSL} = X'_{DSL}\cos(\phi' - \phi) + Y'_{DSL}\sin(\phi' - \phi) \tag{B.18}$$

$$Y_{DSL} = -X'_{DSL}\sin(\phi' - \phi) + Y'_{DSL}\cos(\phi' - \phi), \tag{B.19}$$

Fig. B.3 shows an example of the application of this method. The corrected magnetic field was derived by rotating the corresponding SSL data, whereas the correction of flow velocity used the second approach (Equations (B.18) and (B.19)). Comparing data after the shadow, one can see that the corrected spin phase, magnetic field, and flow velocity match the originally measured data quite well.

B.5 Discussion

Ideally, spacecraft temperature should be used to model $\omega(t)$. However, this piece of information is not generally available for THEMIS/ARTEMIS. In addition, one may argue that an exponential model may be more appropriate, such as the one used in *Taylor* [1968]. However, a simple exponential model, as in *Taylor* [1968], does not give a two-side bounded parameter range, which makes it difficult to search for an optimized parameter. Moreover, it does not have the advantage of allowing longer shadow crossings than the general situation to avoid the 2π ambiguity issue of spin phase. Compared to the exponential model in *Taylor* [1968], the method proposed in this appendix has the advantage of easy implementation and allowance of longer shadow crossings to avoid the 2π ambiguity of spin phase.

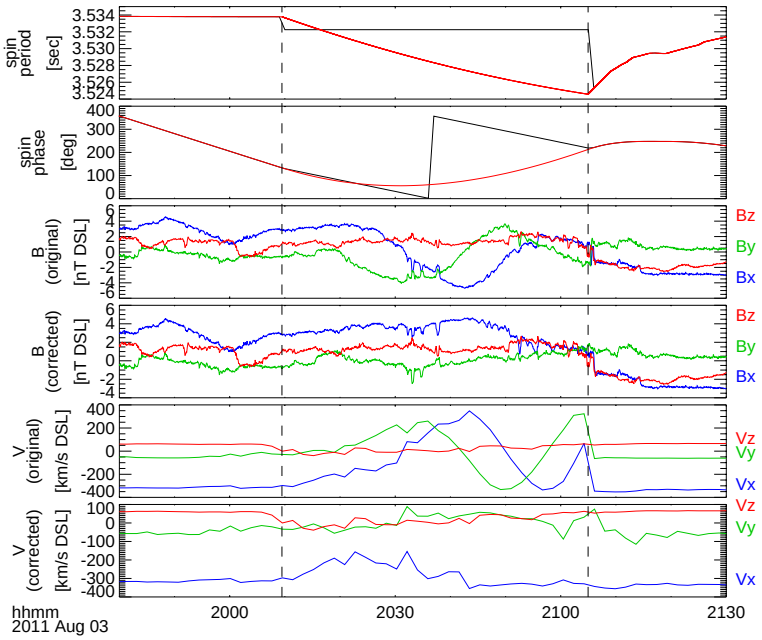

Figure B.3: An example of the correction of spin period, spin phase, magnetic field, and flow velocity from ARTEMIS data. In the top two panels, the red lines are corrected data, whereas the black lines are original data. The two vertical dashed lines indicate the starting and the ending times of a lunar shadow crossing.

Appendix C

Solving 1D Kinetic Dispersion Equation with Mathematica®

This appendix describes a way to solve the 1D kinetic dispersion equation of an electrostatic, unmagnetized plasma system.

Credit: This method was originally developed by Dr. David L. Newman at CU/CIPS.

C.1 Theory

The dispersion equation of a 1D, electrostatic, unmagnetized plasma system with N species is

$$\epsilon = 1 + \sum_{s=1}^{N} \chi_s = 0, \tag{C.1}$$

where χ_s is the susceptibility of the system, and

$$\chi_s = \frac{\omega_{ps}^2}{k^2} \int_L \frac{\partial_v f_{s0}}{\omega/k - v} dv, \tag{C.2}$$

where $\omega_{ps} = \left(\frac{n_{s0} q_s^2}{\epsilon_0 m_s}\right)^{1/2}$ is the plasma frequency of species s, n_{s0} the unperturbed density of species s, f_{s0} the unperturbed distribution function of species s, $\partial_v = \partial/\partial v$, and L designates the standard Landau contour.

C.1.0.1 Landau Contour

In the integral

$$\int_L \frac{\partial_v f_{s0}}{\omega/k - v} dv, \tag{C.3}$$

there are two sources of singularity of the integrand, one being ω/k, the other being $\partial_v f_{s0}$. The Landau contour is a contour that goes from $-\infty$ to ∞ along the real axis in the complex v-plane but always goes underneath and around the singularity ω/k if ω/k has a non-positive imaginary part in the complex v-plane. Figure C.1 illustrates the Landau contour in three different situations.

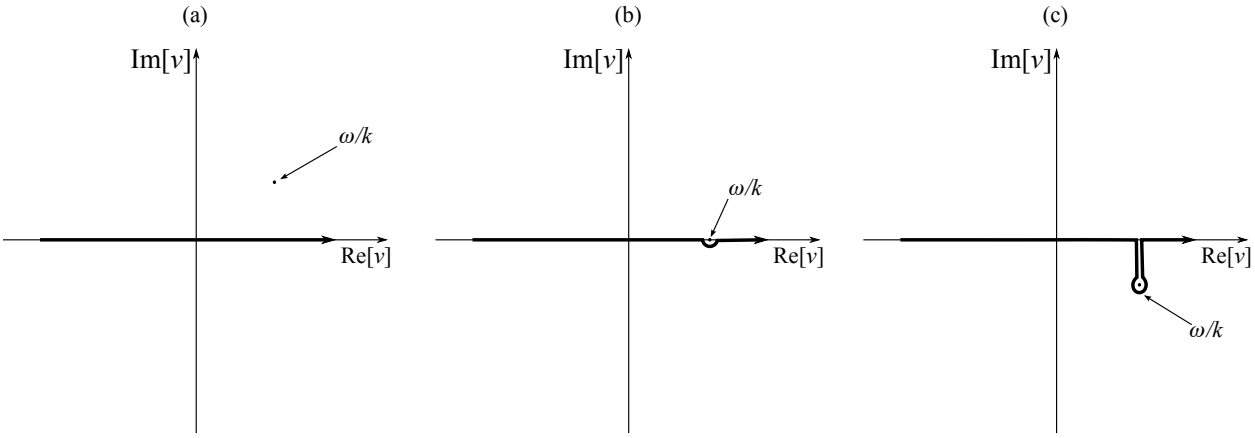

Figure C.1: An illustration of the Landau contour in three different situations.

The evaluation of the Landau contour integral, i.e., Equation (C.3), often invokes the residue theorem, i.e.,:

$$\oint_C f(z)dz = 2\pi i \sum_k \mathrm{Res}(f; z_k), \tag{C.4}$$

where C is a closed contour in counterclockwise direction enclosing a simply connected domain, and z_k are singularities in the domain enclosed by C. One way to evaluate the Landau contour integral is to calculate the sum of residues of singularities of the integrand in the lower half of the complex v plane (LHP) that excludes the resonant pole ω/k, i.e.,

$$\int_L \frac{\partial_v f_{s0}}{\omega/k - v} dv = -2\pi i \sum_k^{\mathrm{LHP}} \mathrm{Res}(\frac{\partial_v f_{s0}}{\omega/k - v}; v_k), \tag{C.5}$$

where the minus sign is due to the clockwise contour enclosing the LHP.

C.1.0.2 Kappa distribution vs. Maxwellian distribution

Good discussions on kappa distributions can be found in *Summers and Thorne* [1991]; *Hau and Fu* [2007]; *Pierrard and Lazar* [2010].

The one-dimensional kappa distribution function is written as

$$f_\kappa(v) = \frac{1}{\sqrt{\pi(2\kappa-3)}v_t}\frac{\Gamma(\kappa)}{\Gamma(\kappa-1/2)}\left(1+\frac{(v-u)^2}{(2\kappa-3)v_t^2}\right)^{-\kappa}, \tag{C.6}$$

where v_t is the thermal velocity of the distribution, u the drifting velocity of the distribution, and $\Gamma(x)$ the Gamma function. In order to have a finite second moment, $\kappa > 3/2$ is required for f_κ in Equation (C.6). Thermal velocity v_t is defined as the second moment of a distribution and temperature is defined as $T = mv_t^2$ in this appendix.

The one-dimensional Maxwellian distribution function reads

$$f_M(v) = \frac{1}{(2\pi v_t^2)^{1/2}}\exp\left[-\frac{(v-u)^2}{2v_t^2}\right]. \tag{C.7}$$

One difference between kappa distributions and Maxwellian distributions is that kappa distributions have heavy tails. Figure C.2 shows a 1D kappa distribution and a 1D Maxwellian distribution with identical thermal velocity where f_κ is clearly larger than f_M when $|v| \gtrsim 2.5v_t$. However, the tail of a distribution is only important for high-order moments. For a 1D plasma system, most often only low-order moments are important, such as density, velocity, and temperature. Therefore, most often one can use a kappa distribution as a good approximation to a Maxwellian distribution.

C.1.0.3 Calculation of the Landau contour integral for a specific distribution

It is relatively easy to calculate the Landau contour integral for a kappa distribution. Suppose the undisturbed distribution of species s is

$$f_{s0}(v) = \frac{1}{\sqrt{\pi(2\kappa_s-3)}v_{ts}}\frac{\Gamma(\kappa_s)}{\Gamma(\kappa_s-1/2)}\left(1+\frac{(v-u_s)^2}{(2\kappa_s-3)v_{ts}^2}\right)^{-\kappa_s}. \tag{C.8}$$

The singularity due to $\partial_v f_{s0}$ in the LHP is $v = u_s - i\sqrt{2\kappa_s-3}v_{ts}$. Using Mathematica, it is easy to evaluate the residue of $\frac{\partial_v f_{s0}}{\omega/k-v}$ at this singularity.

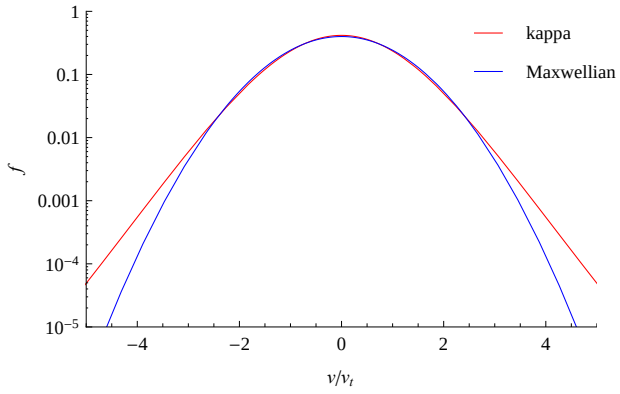

Figure C.2: An illustration of heavy tails of a kappa distribution ($\kappa = 10$) compared to a Maxwellian distribution.

On the other hand, the Maxwellian distribution is a limit of the kappa distribution as $\kappa \to \infty$, namely,

$$\lim_{\kappa\to\infty} f_\kappa(v) = \frac{1}{(2\pi v_t^2)^{1/2}} \exp\left[-\frac{(v-u)^2}{2v_t^2}\right] = f_M. \tag{C.9}$$

Therefore, the LHP singularity goes to infinity for f_M, which makes it rather difficult to evaluate the residue at that singularity. **Therefore, it is easier to use kappa distributions for the calculation of the Landau contour integral.**

C.1.0.4 The Nyquist criterion for instability

Denote

$$R_s = \omega_{ps}^2 \int_L \frac{\partial_v f_{s0}}{\omega/k - v} dv, \tag{C.10}$$

$$R = \sum_{s=1}^{N} R_s, \tag{C.11}$$

$$\zeta = \omega/k. \tag{C.12}$$

Then, R is a function of ζ alone, i.e., $R = R(\zeta)$. $R(\zeta)$ is a characteristic function of a plasma system, and is connected to the susceptibility of the system (χ) by the relation

$$R = k^2\chi. \tag{C.13}$$

The Nyquist criterion states that as ζ goes in the counterclockwise direction along a closed contour, which goes from $-\infty$ to $+\infty$ along a straight line infinitely close to but above the real axis and completes the contour by circling around the upper half plane of the ζ-plane as shown in Figure C.3(a), the number of unstable modes of the system is equal to how many times that the corresponding $-R(\zeta)$ contour crosses the positive real axis in the R-plane. Figure C.3(b) shows an example of such a contour in the R-plane, which indicates that there is one unstable mode of the corresponding plasma system. Note that an infinite ζ always maps to the origin in the R-plane.

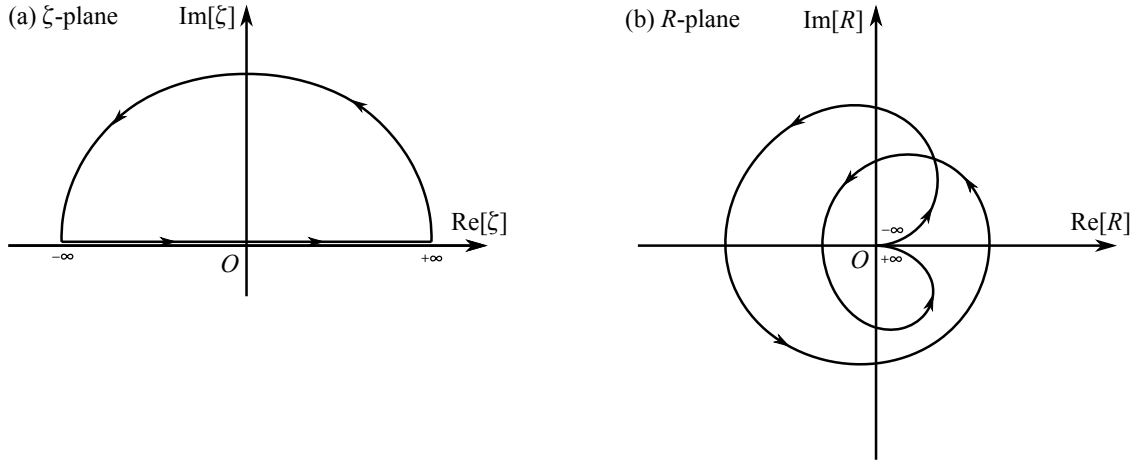

Figure C.3: An example mapping from ζ-plane to R-plane for the Nyquist criterion for instability.

A rigorous derivation of the Nyquist criterion for instability can be found in *Penrose* [1960]. With the Nyquist criterion, one can easily find the number of unstable modes in the system by plotting a Nyquist diagram like the one in Figure C.3(b).

C.2 Method

The ultimate goal of solving a dispersion equation is to obtain $\omega_r(k)$ and $\gamma(k)$ where ω_r and γ are the real part and imaginary part of ω respectively. The Mathematica function `FindRoot` is used for this goal. One prerequisite of `FindRoot` is to specify a good initial guess, which is achieved graphically in this method.

Utilizing $R(\zeta)$, the dispersion relation can be written as:

$$R(\zeta) = -k^2. \tag{C.14}$$

Therefore, the solution to the dispersion relation corresponds to intersections of

$$\mathrm{Im}[R(\zeta)] = 0 \tag{C.15}$$

and

$$\mathrm{Re}[R(\zeta)] = -k^2 \tag{C.16}$$

in the ζ-plane. To find such intersections in the ζ-plane, draw a contour of $\mathrm{Im}[R(\zeta)]$ for value 0, and a contour of $\mathrm{Re}[R(\zeta)]$ for a specific k. Then, use the intersections as initial guesses to solve Equations (C.15) and (C.16) with `FindRoot`.

A general work flow can be the following:

(1) Make generic definitions of f_{s0} and R_s.

(2) Define R for a specific system.

(3) Plot a Nyquist diagram to identify the number of unstable modes in the system.

(4) Plot contours of $\mathrm{Im}[R]$ and $\mathrm{Re}[R]$ to find initial guesses for deriving $\omega_r(k)$ and $\gamma(k)$.

(5) Solve Equations (C.15) and (C.16) for $\omega_r(k)$ and $\gamma(k)$ with `FindRoot` respectively.

C.3 Implementation

C.3.1 Normalization

It is often desired to normalize the equation when solving a dispersion equation. Normalization not only converts the equation into a simpler form to solve, but also makes it more straightforward to interpret the solution. In this case, the following normalization scheme is

chosen:

$$k = \tilde{k}\frac{1}{\lambda_{D1}}, \tag{C.17}$$

$$\omega = \tilde{\omega}\omega_{p1}, \tag{C.18}$$

$$v = \tilde{v}v_{t1}, \tag{C.19}$$

$$f = \tilde{f}\frac{1}{v_{t1}}, \tag{C.20}$$

where the first species ($s = 1$) is a reference species, and $\lambda_{D1} = \sqrt{\frac{\epsilon_0 m_1 v_{t1}^2}{n_{1,0} q_1^2}}$ the Debye length of the first species. With this normalization scheme, Equation (C.1) becomes

$$1 + \frac{1}{\tilde{k}^2}\sum_{s=1}^{N}\alpha_s \int_L \frac{\partial_{\tilde{v}}\tilde{f}_{s0}}{\tilde{\omega}/\tilde{k} - \tilde{v}} d\tilde{v} = 0, \tag{C.21}$$

where $\alpha_s = \frac{m_1}{m_s}\frac{n_{s0}}{n_{1,0}}\frac{q_s^2}{q_1^2}$.

In this method, kappa distributions are used. The normalized kappa distribution function of species s is

$$\tilde{f}_{s0}(v) = \frac{1}{\sqrt{\pi(2\kappa_s - 3)}\tilde{v}_{ts}}\frac{\Gamma(\kappa_s)}{\Gamma(\kappa_s - 1/2)}\left(1 + \frac{(\tilde{v} - \tilde{u}_s)^2}{(2\kappa_s - 3)\tilde{v}_{ts}^2}\right)^{-\kappa_s}, \tag{C.22}$$

where $\tilde{v}_{ts} = v_{ts}/v_{t1}$ and $\tilde{u}_s = u_s/v_{t1}$.

C.3.2 Implementation in Mathematica

Mathematica source codes are attached in the following.

General Definitions

■ Define kappa distribution function

In[1]:=
```
fkappa[v_, κ_, vt_, u_] :=
  (1 / Sqrt[π (2 κ - 3) vt^2]) * (Gamma[κ] / Gamma[κ - 1 / 2]) / (1 + (v - u)^2 / ((2 κ - 3) vt^2))^κ;
```

■ Define Landau contour integral

In[2]:=
```
landauInt[ζr_, ζi_, κ_, vt_, u_] := -2 π i *
   Residue[D[fkappa[v, κ, vt, u], v] / (ζr + i * ζi - v), {v, u - i * Sqrt[2 κ - 3] * vt}];
```

■ Define Rs

In[3]:=
```
Rs[ζr_, ζi_, κ_, vt_, u_, α_] := α * landauInt[ζr, ζi, κ, vt, u];
```

Langmuir Waves

This part demonstrates the dispersion relation of Langmuir waves. The plasma system consists of only one species, an electron species. Ion dynamics is ignored.

■ Define R of the system

In[4]:=
```
κ = 4; u = 0; vt = 1; α = 1;
ftot[v_] := fkappa[v, κ, vt, u];
Rtot[ζr_, ζi_] := Rs[ζr, ζi, κ, vt, u, α];
```

In[11]:=
```
Plot[ftot[v], {v, -5, 5}, Frame → True,
 FrameLabel → {v, f, "System distribution function"}]
```

Out[11]=

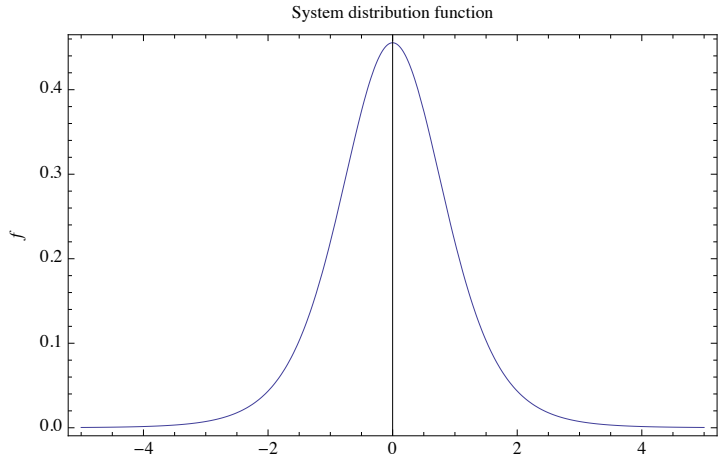

■ Plot the Nyquist diagram

In[13]:=
```
ζmin = -10; ζmax = 10; npts = 5000; dζ = (ζmax - ζmin) / (npts - 1.);
Ntable = Table[{0, 0}, {npts}];
For[i = 1, i ≤ npts, i++,
 ζtmp = ζmin + (i - 1) * dζ;
 Ntable[[i, 1]] = -Re[Rtot[ζtmp, 0]];
 Ntable[[i, 2]] = -Im[Rtot[ζtmp, 0]];
]
```

In[18]:=
```
ListLinePlot[Ntable, PlotRange → All, Frame → True,
 FrameLabel → {"-Re[k^2 χ]", "-Im[k^2 χ]", "Nyquist diagram of the system"}]
```

Out[18]=

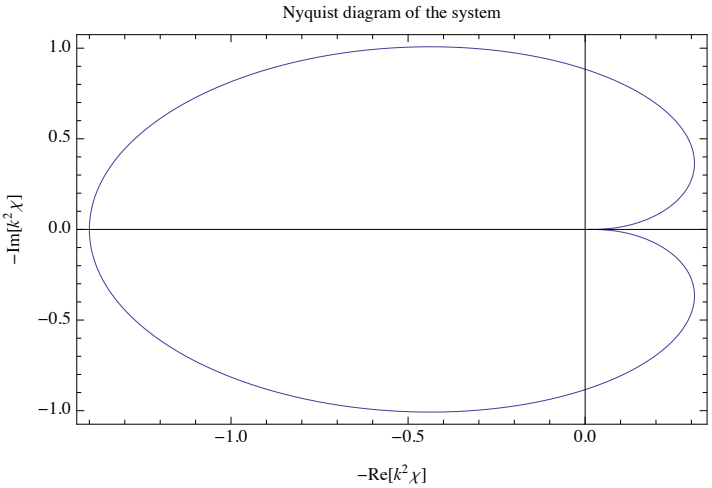

■ Find initial guess

In[19]:=
```
nx = 100; ny = 100; ζrmin = -12; ζrmax = 12; ζimin = -10; ζimax = 10;
imPlot = ContourPlot[Im[Rtot[ζr, ζi]], {ζr, ζrmin, ζrmax}, {ζi, ζimin, ζimax},
   PlotPoints → {nx, ny}, ContourLabels → None, Contours → {0},
   ContourShading → False, MaxRecursion → 2, ContourStyle → {Black}];
rePlot = ContourPlot[Re[Rtot[ζr, ζi]], {ζr, ζrmin, ζrmax}, {ζi, ζimin, ζimax},
   PlotPoints → {nx, ny}, ContourLabels → None, Contours → {-0.01},
   ContourShading → False, MaxRecursion → 2, ContourStyle → {Red}];
```

In[26]:=
```
(* Overview *)
Show[{imPlot, rePlot}, PlotRange → All,
 GridLines → Automatic, FrameLabel -> {"Re[ζ]", "Im[ζ]",
   "Contours of Im[R] and Re[R] (Black: Im[R]=0; Red: Re[R]=-0.01"}]
```

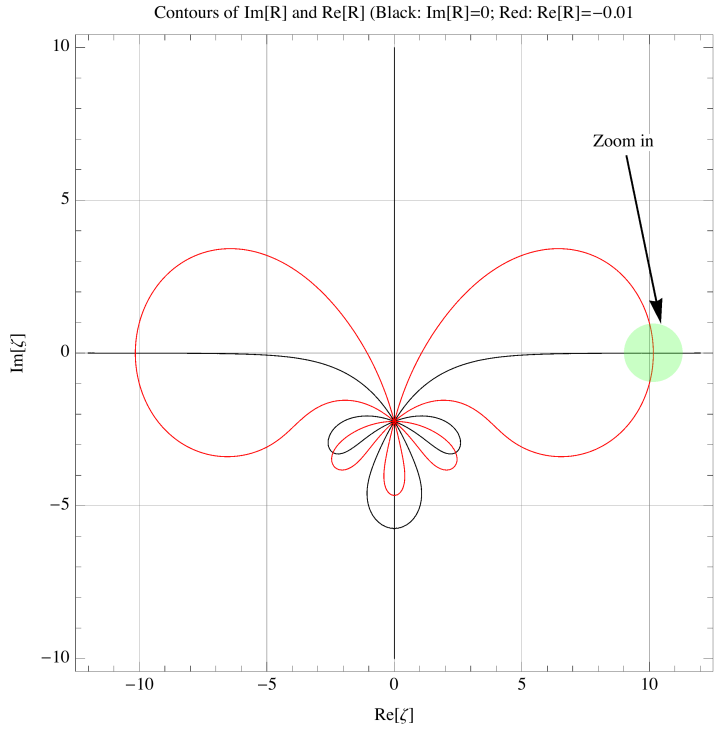
Contours of Im[R] and Re[R] (Black: Im[R]=0; Red: Re[R]=−0.01
Zoom in
10
5
0
−5
−10
Im[ζ]
−10
−5
0
5
10
Re[ζ]

In[27]:=
```
(* Zoom in *)
Show[{imPlot, rePlot}, PlotRange → {{10, 10.2}, {-0.05, 0}},
 GridLines → Automatic, FrameLabel -> {"Re[ζ]", "Im[ζ]",
   "Contours of Im[R] and Re[R] (Black: Im[R]=0; Red: Re[R]=-0.01"}]
```

Out[27]=

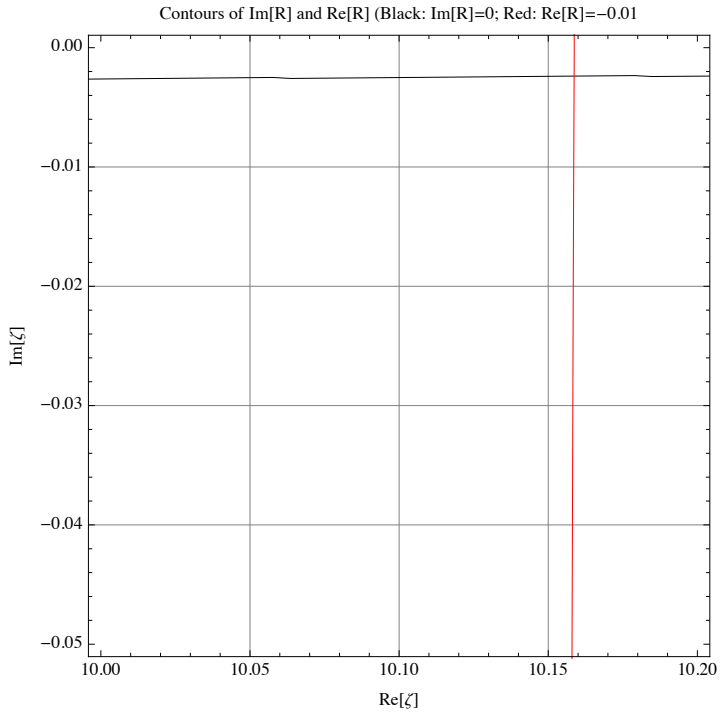

Initial guess for Langmuir waves: ζr=10.16, ζi=-0.0026.

- **Obtain ω_r(k) and γ(k)**

In[28]:=
```
(*Parameters*)
kmin = 0.001; kmax = 1.0 + kmin; nk = 100; ξrGuess = 10.16; ξiGuess = -0.0026;
(*Main body of finding ω(k) and γ(k)*)
(**inherit parameters**)
k1 = kmin; k2 = kmax; npts = nk;
(** initialize tables for storing ω(k) and γ(k) **)
ωkTable = Table[{k1 + (k2 - k1) * (i - 1.) / (npts - 1.), 0}, {i, 1, npts}];
γkTable = Table[{k1 + (k2 - k1) * (i - 1.) / (npts - 1.), 0}, {i, 1, npts}];
(** start main loop **)
Do[ (*start*)
  kCurrent = ωkTable[[i, 1]]; (* update k *)
  (*Find ω and γ for a given k*)
  newRoot = FindRoot[{Re[Rtot[ξr, ξi]] == -kCurrent^2, Im[Rtot[ξr, ξi]] == 0},
    {ξr, ξrGuess}, {ξi, ξiGuess}];
  (*Store ω and γ *)
  ωkTable[[i, 2]] = kCurrent * ξr /. newRoot;
  γkTable[[i, 2]] = kCurrent * ξi /. newRoot;
  (*update guess by taking last root*)
  ξrGuess = ξr /. newRoot; ξiGuess = ξi /. newRoot, {i, 1, npts}(*loop index*)];
(*end of main loop*)
```

In[36]:=
```
ListLinePlot[{ωkTable, γkTable}, PlotStyle → {Blue, Red}, Frame → True,
 FrameLabel → {"kλD1", "", "Blue: ω-k relation; Red: γ-k relation"}]
```

Out[36]=

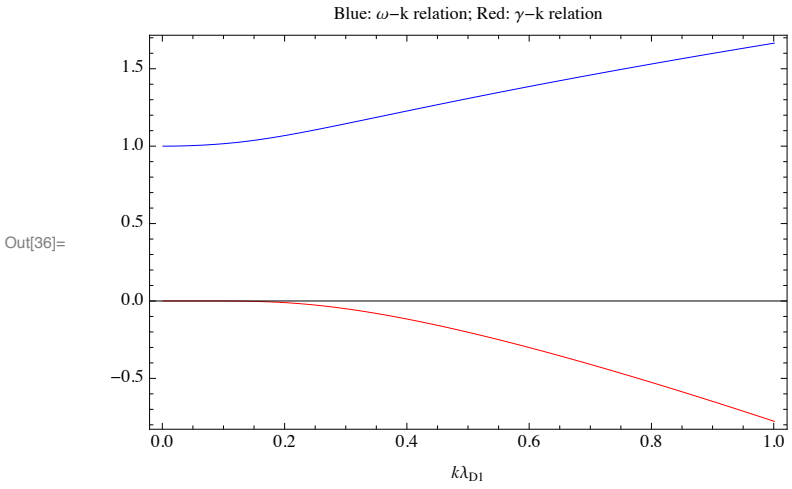

Two-Stream Instability

- **Define R of the system**

In[37]:=
```
κ = 4; u1 = 0; vt1 = 1; u2 = 5; vt2 = 1; α1 = 1; α2 = 1;
ftot[v_] := fkappa[v, κ, vt1, u1] + fkappa[v, κ, vt2, u2];
Rtot[ξr_, ξi_] := Rs[ξr, ξi, κ, vt1, u1, α1] + Rs[ξr, ξi, κ, vt2, u2, α2];
```

In[40]:=
```
Plot[ftot[v], {v, -5, 10}, Frame → True,
 FrameLabel → {v, f, "System distribution function"}]
```

Out[40]=

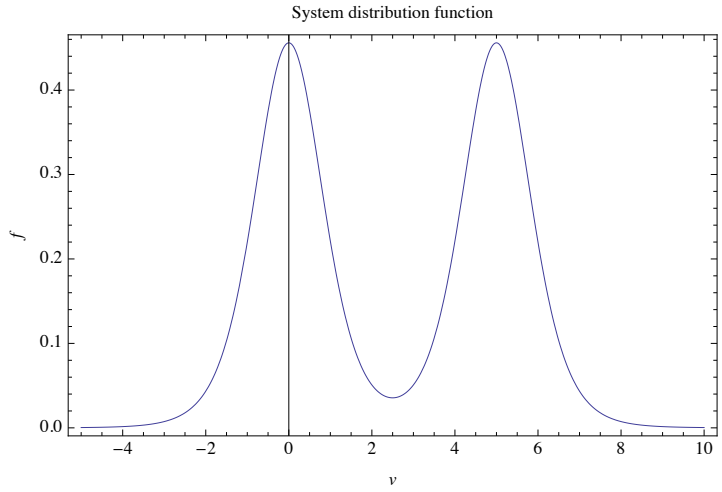

■ Plot the Nyquist diagram

In[41]:=
```
ζmin = -10; ζmax = 10; npts = 5000; dζ = (ζmax - ζmin) / (npts - 1.);
Ntable = Table[{0, 0}, {npts}];
For[i = 1, i ≤ npts, i++,
 ζtmp = ζmin + (i - 1) * dζ;
 Ntable[[i, 1]] = -Re[Rtot[ζtmp, 0]];
 Ntable[[i, 2]] = -Im[Rtot[ζtmp, 0]];
]
```

In[44]:=
```
ListLinePlot[Ntable, PlotRange → All, Frame → True,
 FrameLabel → {"-Re[k^2 χ]", "-Im[k^2 χ]", "Nyquist diagram of the system"}]
```

Out[44]=

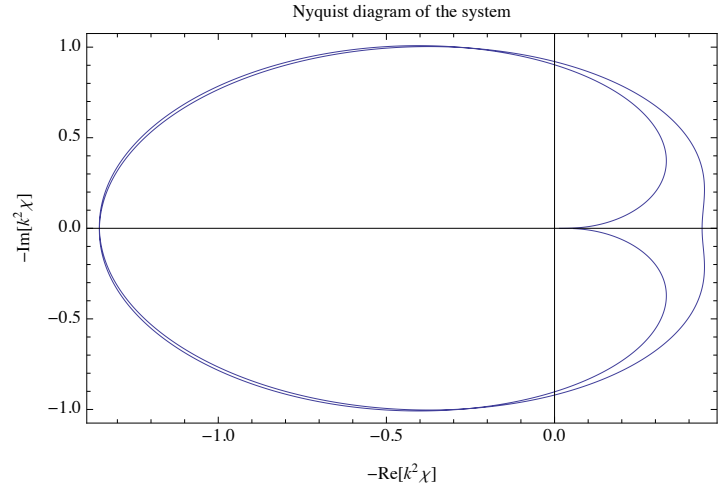

■ Find initial guess

In[45]:=
```
nx = 100; ny = 100; ζrmin = -15; ζrmax = 20; ζimin = -5; ζimax = 5;
imPlot = ContourPlot[Im[Rtot[ζr, ζi]], {ζr, ζrmin, ζrmax}, {ζi, ζimin, ζimax},
   PlotPoints → {nx, ny}, ContourLabels → None, Contours → {0},
   ContourShading → False, MaxRecursion → 2, ContourStyle → {Black}];
rePlot = ContourPlot[Re[Rtot[ζr, ζi]], {ζr, ζrmin, ζrmax}, {ζi, ζimin, ζimax},
   PlotPoints → {nx, ny}, ContourLabels → None, Contours → {-0.01},
   ContourShading → False, MaxRecursion → 2, ContourStyle → {Red}];
```

In[48]:=
```
(* Save result *)
twostreamImPlot = imPlot;
twostreamRePlot = rePlot;
```

In[50]:=
```
(* Overview *)
Show[{twostreamImPlot, twostreamRePlot}, PlotRange → All,
 GridLines → Automatic, FrameLabel -> {"Re[ζ]", "Im[ζ]",
   "Contours of Im[R] and Re[R] (Black: Im[R]=0; Red: Re[R]=-0.01"}]
```

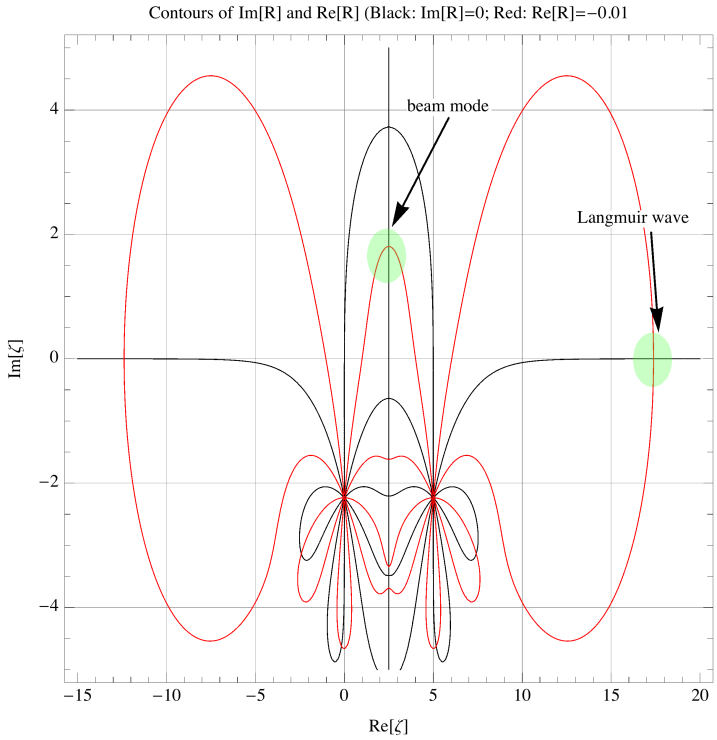

In[51]:=
```
(* Zoom in for the Langmuir wave branch *)
Show[{twostreamImPlot, twostreamRePlot}, PlotRange → {{17, 18}, {-0.002, -0.0005}},
 GridLines → Automatic, FrameLabel -> {"Re[ζ]", "Im[ζ]",
   "Contours of Im[R] and Re[R] (Black: Im[R]=0; Red: Re[R]=-0.01"}]
```

Out[51]=

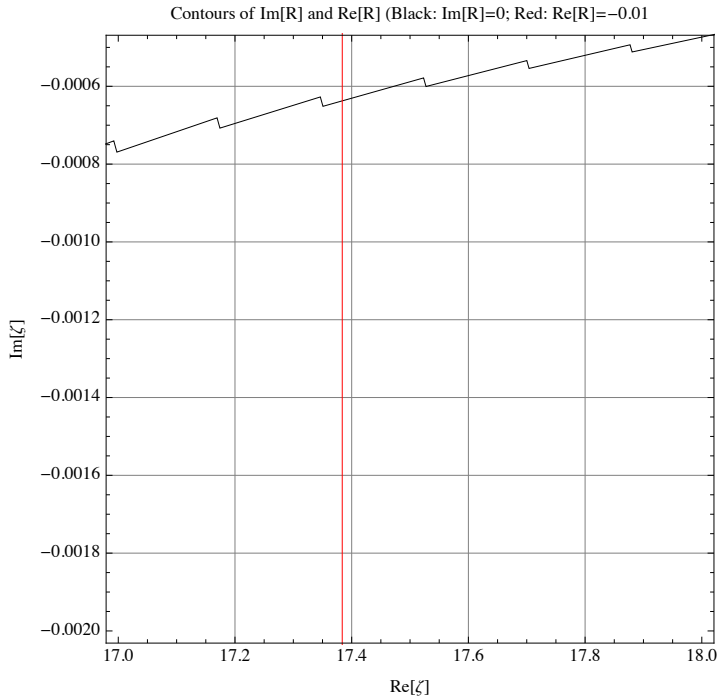

Initial guess for the Langmuir wave branch: ζr=17.38, ζi=-0.00065.

In[52]:=
```
(* Zoom in for the beam mode branch *)
Show[{twostreamImPlot, twostreamRePlot}, PlotRange → {{2, 3}, {1.8, 1.82}},
 GridLines → Automatic, FrameLabel -> {"Re[ζ]", "Im[ζ]",
   "Contours of Im[R] and Re[R] (Black: Im[R]=0; Red: Re[R]=-0.01"}]
```

Out[52]=

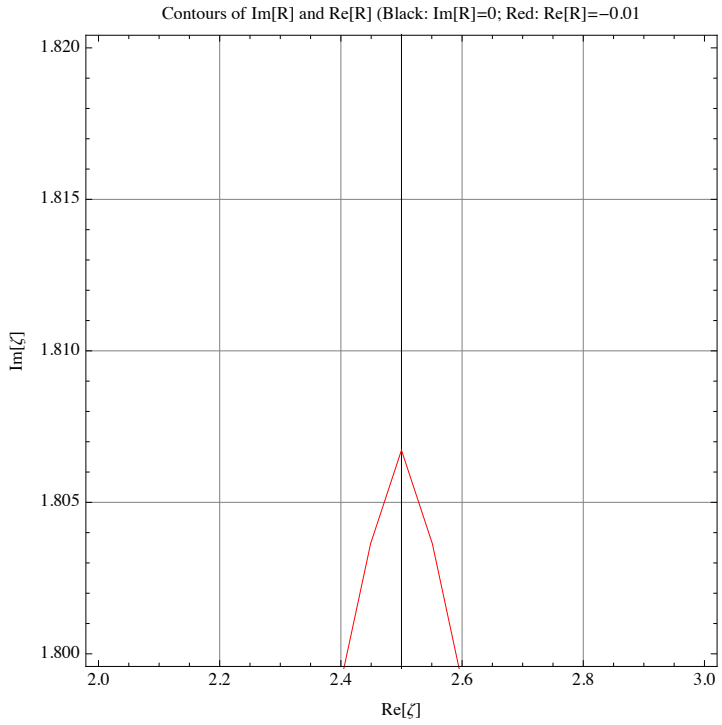

Initial guess for the Langmuir wave branch: ζr=2.5, ζi=1.8065.

■ Obtain ω_r(k) and γ(k)

In[53]:=
```
(* Langmuir wave *)
(*Parameters*)
kmin = 0.001; kmax = 0.7 + kmin; nk = 200; ζrGuess = 17.38; ζiGuess = -0.00065;
(*Main body of finding ω(k) and γ(k)*)
(**inherit parameters**)
k1 = kmin; k2 = kmax; npts = nk;
(** initialize tables for storing ω(k) and γ(k) **)
ωkTable = Table[{k1 + (k2 - k1) * (i - 1.) / (npts - 1.), 0}, {i, 1, npts}];
γkTable = Table[{k1 + (k2 - k1) * (i - 1.) / (npts - 1.), 0}, {i, 1, npts}];
(** start main loop **)
Do[ (*start*)
  kCurrent = ωkTable[[i, 1]]; (* update k *)
  (*Find ω and γ for a given k*)
  newRoot = FindRoot[{Re[Rtot[ζr, ζi]] == -kCurrent^2, Im[Rtot[ζr, ζi]] == 0},
    {ζr, ζrGuess}, {ζi, ζiGuess}];
  (*Store ω and γ *)
  ωkTable[[i, 2]] = kCurrent * ζr /. newRoot;
  γkTable[[i, 2]] = kCurrent * ζi /. newRoot;
  (*update guess by taking last root*)
  ζrGuess = ζr /. newRoot; ζiGuess = ζi /. newRoot, {i, 1, npts}(*loop index*)];
(*end of main loop*)
```

In[58]:=
```
(* Save results *)
twostreamLangωkTable = ωkTable;
twostreamLangγkTable = γkTable;
```

In[60]:=
```
(* Beam mode *)
(*Parameters*)
kmin = 0.001; kmax = 0.7 + kmin; nk = 200; ζrGuess = 2.5; ζiGuess = 1.8065;
(*Main body of finding ω(k) and γ(k)*)
(**inherit parameters**)
k1 = kmin; k2 = kmax; npts = nk;
(** initialize tables for storing ω(k) and γ(k) **)
ωkTable = Table[{k1 + (k2 - k1) * (i - 1.) / (npts - 1.), 0}, {i, 1, npts}];
γkTable = Table[{k1 + (k2 - k1) * (i - 1.) / (npts - 1.), 0}, {i, 1, npts}];
(** start main loop **)
Do[ (*start*)
  kCurrent = ωkTable[[i, 1]]; (* update k *)
  (*Find ω and γ for a given k*)
  newRoot = FindRoot[{Re[Rtot[ζr, ζi]] == -kCurrent^2, Im[Rtot[ζr, ζi]] == 0},
    {ζr, ζrGuess}, {ζi, ζiGuess}];
  (*Store ω and γ *)
  ωkTable[[i, 2]] = kCurrent * ζr /. newRoot;
  γkTable[[i, 2]] = kCurrent * ζi /. newRoot;
  (*update guess by taking last root*)
  ζrGuess = ζr /. newRoot; ζiGuess = ζi /. newRoot, {i, 1, npts}(*loop index*)];
(*end of main loop*)
```

In[65]:=
```
(* Save results *)
twostreamBeamωkTable = ωkTable;
twostreamBeamγkTable = γkTable;
```

In[74]:=
```
ListLinePlot[{twostreamLangωkTable, twostreamLangγkTable, twostreamBeamωkTable,
  twostreamBeamγkTable}, PlotStyle → {Black, Blue, Purple, Green}, Frame → True,
 FrameLabel → {"kλD1", "", "Black: ω-k, Langmuir wave; Blue: γ-k, Langmuir wave;
Purple: ω-k, beam mode; Green: γ-k, beam mode"}]
```

Out[74]=

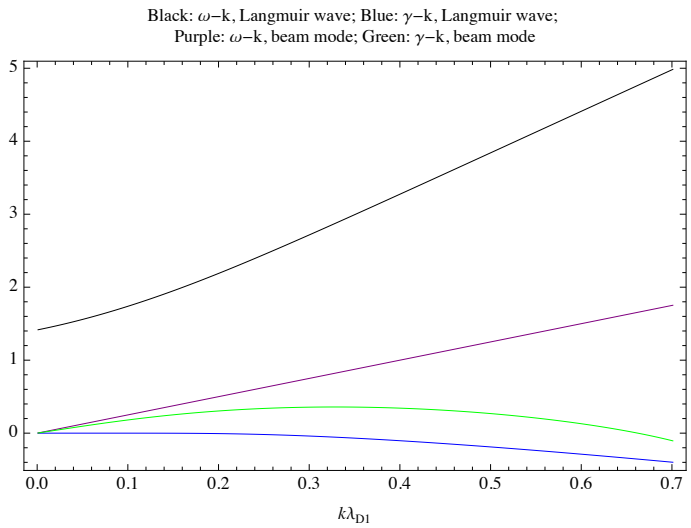

Comments: The ω-k relation of the beam mode shows that the phase velocity of the beam mode is exactly one half of the relative drifting velocity between the two electron beams in the system, which is expected.